MINISTÉRIO DA CIÊNCIA, TECNOLOGIA E INOVAÇÃO
INSTITUTO NACIONAL DE PESQUISAS ESPACIAIS

sid.inpe.br/mtc-m21d/2024/02.20.18.27-TDI

MAPPING BURNED AREAS IN THE CERRADO USING TIME SERIES FROM THE CBERS AND AMAZONIA SATELLITES

Alisson Cleiton de Oliveira

Master's Dissertation of the Graduate Course in Remote Sensing, guided by Dr. Thales Sehn Körting, approved in February 09, 2024.

URL of the original document:
<http://urlib.net/8JMKD3MGP3W34T/4APPK92>

INPE
São José dos Campos
2024

PUBLISHED BY:

Instituto Nacional de Pesquisas Espaciais - INPE
Coordenação de Ensino, Pesquisa e Extensão (COEPE)
Divisão de Biblioteca (DIBIB)
CEP 12.227-010
São José dos Campos - SP - Brasil
Tel.:(012) 3208-6923/7348
E-mail: pubtc@inpe.br

MINISTÉRIO DA CIÊNCIA, TECNOLOGIA E INOVAÇÃO
INSTITUTO NACIONAL DE PESQUISAS ESPACIAIS

sid.inpe.br/mtc-m21d/2024/02.20.18.27-TDI

MAPPING BURNED AREAS IN THE CERRADO USING TIME SERIES FROM THE CBERS AND AMAZONIA SATELLITES

Alisson Cleiton de Oliveira

Master's Dissertation of the Graduate Course in Remote Sensing, guided by Dr. Thales Sehn Körting, approved in February 09, 2024.

URL of the original document:
<http://urlib.net/8JMKD3MGP3W34T/4APPK92>

INPE
São José dos Campos
2024

Cataloging in Publication Data

Oliveira, Alisson Cleiton de.

Ol14m Mapping burned areas in the Cerrado using time series from the CBERS and Amazonia satellites / Alisson Cleiton de Oliveira. – São José dos Campos : INPE, 2024.

xvi + 82 p. ; (sid.inpe.br/mtc-m21d/2024/02.20.18.27-TDI)

Dissertation (Master in Remote Sensing) – Instituto Nacional de Pesquisas Espaciais, São José dos Campos, 2024.

Guiding : Dr. Thales Sehn Körting.

1. Fire. 2. WFI. 3. Chapada dos Veadeiros National Park. 4. Supervised classification. 5. Random forest. I.Title.

CDU 614.84:528.8(213.54)

MINISTÉRIO DA CIÊNCIA, TECNOLOGIA E INOVAÇÃO

INSTITUTO NACIONAL DE PESQUISAS ESPACIAIS
Serviço de Pós-Graduação - SEPGR

DEFESA FINAL DE DISSERTAÇÃO DE ALISSON CLEITON DE OLIVEIRA
REG. 485855/2022, BANCA Nº 001/2024

No dia 09 de fevereiro de 2024, de forma online e presencial no auditório da OBT, o(a) aluno(a) mencionado(a) acima defendeu seu trabalho final (apresentação oral seguida de arguição) perante uma Banca Examinadora, cujos membros estão listados abaixo. O(A) aluno(a) foi APROVADO(A) pela Banca Examinadora, por unanimidade, em cumprimento ao requisito exigido para obtenção do Título de Mestre em Sensoriamento Remoto, com a exigência de que o trabalho final a ser publicado deverá incorporar as correções sugeridas pela Banca Examinadora, com revisão pelo(s) orientador(es).

Novo Título: MAPPING BURNED AREAS IN THE CERRADO USING TIME SERIES FROM THE CBERS AND AMAZÔNIA SATELLITES

Membros da banca:

Dr. Lenio Soares Galvao – Presidente – INPE
Dr. Thales Sehn Körting – Orientador – INPE
Dr. Guilherme Augusto Verola Mataveli – Membro Interno – INPE
Dra. Tahisa Neitzel Kuck – Membro Externo – IEAv

Documento assinado eletronicamente por **Guilherme Augusto Verola Mataveli (E)**, **Usuário Externo**, em 16/02/2024, às 16:19 (horário oficial de Brasília), com fundamento no § 3º do art. 4º do Decreto nº 10.543, de 13 de novembro de 2020.

Documento assinado eletronicamente por **Thales Sehn Korting**, **Pesquisador**, em 16/02/2024, às 18:01 (horário oficial de Brasília), com fundamento no § 3º do art. 4º do Decreto nº 10.543, de 13 de novembro de 2020.

Documento assinado eletronicamente por **Tahisa neitzel kuck (E)**, **Usuário Externo**, em 16/02/2024, às 18:24 (horário oficial de Brasília), com fundamento no § 3º do art. 4º do Decreto nº 10.543, de 13 de novembro de 2020.

Documento assinado eletronicamente por **Lênio Soares Galvão**, **Pesquisador**, em 22/02/2024, às 07:46 (horário oficial de Brasília), com fundamento no § 3º do art. 4º do Decreto nº 10.543, de 13 de novembro de 2020.

A autenticidade deste documento pode ser conferida no site https://sei.mcti.gov.br/verifica.html, informando o código verificador **11699217** e o código CRC **C56259BB**.

Referência: Processo nº 01340.000874/2024-54 SEI nº 11699217

ACKNOWLEDGEMENTS

Agradeço à minha família pela presença na distância e compreensão, e aos meus amigos por tornarem, desde os tempos da graduação, a vida mais leve. Agradeço à UFSCar e ao corpo docente do curso de bacharelado em Gestão e Análise Ambiental de 2016-2021, e ao INPE, pelas coisas que aprendi e pela possibilidade de realizar essa pesquisa. Agradeço, principalmente, à CAPES, pois essa dissertação só se tornou realidade graças ao auxílio financeiro que recebi por ser um bolsista de pós-graduação no Brasil. Especial agradecimento ao Prof. Dr. Thales Sehn Körting, meu orientador, que desde o início desse caminho confiou em mim e no nosso trabalho juntos.

ABSTRACT

The Brazilian Cerrado, a hotspot for global biodiversity conservation, evolved under the presence of natural wildfires. Fire has become frequent and widespread, and the Cerrado, where natural fires have occurred for at least four million years, is threatened by human-induced wildfires. The Chapada dos Veadeiros National Park (CVNP), located in the state of Goiás, Brazil, was established in 1961 and currently covers 240,611 ha. In 2017, approximately 66,000 ha were burned in the CVNP, and the Integrated Fire Management (IFM) was implemented still in that year to reduce the negative impacts of future criminal/accidental events. Remote Sensing (RS) data show that there were fire-foci in the CVNP during the dry months of 2020, 2021, and 2022. There are two RS-based products for wildfires detection: products of released heat and products of biophysical changes in vegetation. As an example of provider, there is the Queimadas Program of Brazil's National Institute for Space Research (INPE), which provides products on daily fire hotspots and a monthly product of burned areas for the Cerrado. As of the current date, there are no products that employ Brazilian satellite images for the systematic mapping of burned areas. The objective of this research is to explore methods for supervised classification of time series images captured by the Wide Field Imager (WFI) sensor on board the CBERS-4, CBERS-4A, and AMAZONIA-1 satellites, using the Random Forest (RF) algorithm. The study area is the CVNP and its buffer zone of 10 km, and the time window covers the years 2020, 2021 and 2022. A total of 382 images were acquired from INPE archive and after filtering for cloud cover it was decided to keep 235 images: 50 from 2020, 72 from 2021 and 113 from 2022. The WFI sensor has four spectral bands (BGR NIR), which is a limiting factor. Consequently, we estimated and integrated the BAI (Burned Area Index), EVI (Enhanced Vegetation Index), GEMI (Global Environmental Monitoring Index), NDVI (Normalized Difference Vegetation Index), and NDWI (Normalized Difference Water Index) spectral indices into a regular grid with 500 m x 500 m cells, totalling 38,957 cells. For each one of the previous spectral indices more the NIR band, datasets containing annual and semi-annual observations were structured and the models were trained using samples of "burned areas" and "unburned areas" previously collected through visual image analysis. The annual models achieved at least 90% accuracy and the best generalization results were observed using multi-temporal datasets. The results of this research indicate that, given a representative sample set, it is possible to detect burned areas in the CVNP using WFI imagery.

Keywords: Fire. WFI. Chapada dos Veadeiros National Park. Supervised classification. Random forest.

MAPEAMENTO DE ÁREAS QUEIMADAS NO CERRADO UTILIZANDO SÉRIES TEMPORAIS DOS SATÉLITES CBERS E AMAZONIA

RESUMO

O Cerrado, *hotspot* de conservação da biodiversidade, evoluiu sob a presença de incêndios naturais. O fogo se tornou frequente e difuso na atualidade, e o Cerrado, onde o fogo natural ocorre há pelo menos quatro milhões de anos, é ameaçado por incêndios de origens antrópicas. O Parque Nacional da Chapada dos Veadeiros (PNCV), localizado no estado de Goiás, foi instituído em 1961 e a sua área atual é de 240.611 ha. Em 2017 o PNCV teve cerca de 66 mil ha atingidos por fogo e, ainda nesse ano, foi instituído o Manejo Integrado do Fogo (MIF) a fim de se reduzir os impactos negativos desses eventos criminosos/acidentais. Dados de Sensoriamento Remoto (SR) evidenciam que houve focos de calor nos meses secos de 2020, 2021 e 2022 no PNCV. Existem, principalmente, dois subprodutos de fogo em aplicações de SR: subprodutos de liberação de calor e subprodutos de modificações biofísicas da vegetação. Como exemplo de provedores, tem-se o Programa Queimadas do Instituto Nacional de Pesquisas Espaciais (INPE), que disponibiliza produtos sobre focos de calor diários e um produto mensal de áreas queimadas para o Cerrado. Entretanto não há, até o momento, produtos que utilizem imagens de satélites brasileiros no mapeamento sistemático de áreas queimadas. Assim, essa pesquisa tem como objetivo explorar abordagens de classificação supervisionada de séries temporais de imagens do sensor Wide Field Imager (WFI), a bordo dos satélites brasileiros CBERS-4, CBERS-4A e AMAZONIA-1, com o algoritmo Random Forest (RF). A área de estudo é o PNCV e seu buffer envolvente de 10 km, e a janela temporal engloba os anos de 2020, 2021 e 2022. Ao todo, 382 imagens foram adquiridas do arquivo do INPE e, após a triagem por cobertura de nuvens, optou-se por manter 235 imagens, sendo 50 de 2020, 72 de 2021 e 113 de 2022. O sensor WFI possui quatro bandas (BGR NIR), o que é um limitante. Procedeu-se, portanto, a estimação e a integração dos índices BAI (Índice de Área Queimada), EVI (Índice de Vegetação Melhorado), GEMI (Índice Global de Monitoramento Ambiental), NDVI (Índice de Vegetação por Diferença Normalizada) e NDWI (Índice de Água por Diferença Normalizada) em uma grade regular com células de 500 m x 500 m, o que totaliza 38.957 células. Para cada índice espectral e para a banda do NIR foram estruturados *datasets* contendo observações anuais e semestrais e os treinamentos dos modelos foram conduzidos com amostras de "áreas queimadas" e "áreas não queimadas", coletadas previamente por análise visual de imagens. Como resultado, os modelos anuais atingiram, no mínimo, 90% de acurácia e os melhores resultados de generalização foram observados utilizando *datasets* multitemporais. Os resultados desta pesquisa indicam que é possível, dado um conjunto de amostras representativo, classificar áreas queimadas do Cerrado do PNCV utilizando imagens do sensor WFI.

Palavras-chave: Fogo. WFI. Parque Nacional da Chapada dos Veadeiros. Classificação supervisionada. Random Forest.

LIST OF FIGURES

Page

LIST OF TABLES

Page

CONTENTS

Page

1 INTRODUCTION

The Cerrado, or Brazilian savannas, is hotspot for global biodiversity conservation (MYERS et al., 2000). Its ecosystems are characterized by high species diversity and endemism, while also providing environmental services such as water cycle regulation and carbon storage (BUSTAMANTE; OLIVEIRA, 2008; COLLI et al., 2020). The Brazilian Cerrado is one of the most biodiverse savannas in the world, but historically, conservation efforts and policies in Brazil have not given the same attention to savannas as to forest biomes, including the Amazon (OVERBECK et al., 2015).

According to the Brazilian Institute of Geography and Statistics (IBGE), the Cerrado is classified as a non-forest biome. The proportion of formally protected non-forest environments in Brazil is lower than forest vegetation, and land cover conversion in these environments is driven by the global demand for commodities (OVERBECK et al., 2015). Over time, however, both forest and non-forest environments have experienced deforestation and degradation mainly due to agricultural activities (BUSTAMANTE et al., 2019).

Brazil currently plays a significant role as a major exporter of agricultural products. It is in the Cerrado region where various commodities, mainly soybeans, are produced (SOTERRONI et al., 2019). The 1970s marked the beginning of extensive human occupation in the Cerrado, as governmental development programs promoted land cover conversion to support economic activities, directly resulting in successive deforestation events and the advance of agricultural frontiers (FARIA; SANTOS, 2016; HOFMANN et al., 2021; DUTRA; SOUZA, 2022).

Pivello et al. (2021) report that the states of Mato Grosso and Goiás have experienced significant losses of Cerrado vegetation over the last two decades, and that the agricultural frontier has recently reached the region known as MATOPIBA, which refers to the region comprising the border of the states of Maranhão, Tocantins, Piauí and Bahia. The authors highlight deforestation, the use of pesticides, the spread of monocultures and human-induced fires as factors linked to the dynamics of land use changes in the region. Sawyer et al. (2016) also highlight some of these factors as current direct and indirect causes of threats for the Cerrado conservation.

Changes in land cover are temporally continuous, and fire events in the Cerrado could be considered ambiguous. While most of the Cerrado has an evolutionary dependency on fire, the current incidence of human-induced wildfires has negative impacts on its ecosystems (DURIGAN et al., 2020; FIDELIS et al., 2018). Anthropogenic-

caused wildfires occur in unfavorable seasons, persist for longer periods, are more intense and threaten the biodiversity, which may not resist facing the high recurrence and intensity of these events and the high temperatures of the flames (FIDELIS et al., 2018; KEELEY, 2009).

While land use practices have intensified fire events, Remote Sensing (RS) applications allow the understanding of the Cerrado historical dynamics and the effects of fire at different scales. Currently, national initiatives, such as MapBiomas (MAPBIOMAS, 2023) and TerraClass (INPE, 2023a) develop operational land use and land cover (LULC) products, while MapBiomas Fogo (ALENCAR et al., 2022), Programa Queimadas (INPE, 2023b) and ALARMES (Alarm System of Satellite-Derived Burned Area Estimations) (UFRJ, 2023) provide active fires detection and/or burned area products for the Brazilian Cerrado.

In a RS perspective, changes driven by wildfires can be understood as alterations in vegetal cover or as spectral and spatial movement of the vegetation characteristics over time. RS enables the detection of the electromagnetic radiation emitted or reflected by targets on the Earth's surface and converts them into images, based on the spectral behavior and properties of the targets. It enables various analyses related to the Earth's resources and climate, such as monitoring atmospheric and oceanic conditions, crop planning and deforestation detection (JENSEN, 2009).

RS analysis are performed across a wide range of the electromagnetic spectrum, including optical, infrared, and long wavelengths regions (JENSEN, 2009). In this context, images derived from orbital sensors should be used according to their specifications to ensure accurate analysis of the monitored terrestrial phenomena. By applying RS techniques in the analysis of satellite images for monitoring wildfires and assessing their impacts on ecosystems, studies employ methods that vary based on the resolutions of the sensors and on the available technology at the moment.

Bands positioned in the infrared spectral region are effective in distinguishing active fires and burned areas in landscapes (PEREIRA et al., 2016). Additionally, the temporal coverage of orbital platforms is a factor that influences the analysis, and sensors with high temporal resolution allow for short-term analysis and rapid provision of RS products. Various RS-based products are currently available for wildfire analysis, including active fire and burned area data (PENHA, 2018). These RS products may differ depending on the methodology used and the reference sensor.

As an example of a RS application related to fire, burned area products allow for the

comprehension of the characteristics and behavior of wildfires, contributing to the estimation of their impacts (GAVEAU et al., 2021). Despite considering the sensor's spectral and temporal resolutions, the applied methodology behind these products is fundamental to ensure a reliable accuracy (SHIMABUKURO et al., 2020). Artificial Intelligence (AI) is currently a reality and is being used to improve RS approaches, including the assessment of burned areas mapping (ALENCAR et al., 2022; ROY et al., 2019; RAMO et al., 2018; SHIMABUKURO et al., 2009).

Analysis of the spectral characteristics of targets in different regions of the electromagnetic spectrum is limited when a given sensor, such as the WFI (Wide Field Imager) on board the CBERS-4 (China-Brazil Earth Resources Satellite), CBERS-4A and AMAZONIA-1 satellites, operates in the BGR NIR (blue, green, red and near-infrared) multispectral bands. Nevertheless, RS and AI techniques, such as detecting land use and land cover changes and analyzing time series data, could be alternatives to the use of multispectral bands for mapping burned areas, through the synergy of RS-based data and pattern recognition algorithms, for example.

By combining the temporal coverage of the CBERS-4, CBERS-4A and AMAZONIA-1 satellites, it is possible to acquire WFI images with a spatial resolution of 55 m or 64 m every 1-3 days. Approaches based on WFI images from these satellites need to harmonize, to some extent, the data. Despite being the same sensor, there are differences in spatial resolution and in the grid of the satellites (OLDONI, 2022). Considering these aspects, we propose an approach for composing inter-satellites time series with the WFI sensor for mapping burned areas in a region of the Cerrado.

Currently, fires have become more frequent, intense, and widespread, and the Brazilian Cerrado, where natural wildfires have occurred for at least four million years, now faces threats related to land use and land cover conflicts, agricultural activities and recreational practices (SIMON et al., 2009; PIVELLO et al., 2021). A RS method for mapping burned areas based on Brazilian satellites with high temporal coverage has the potential to be useful for conservation units and priority areas, and it is in line with national plans for monitoring the Cerrado (MMA, 2018).

1.1 Hypothesis

It is possible to map burned areas in the Cerrado through automated processes using artificial intelligence applied to harmonized time series derived from bands and spectral indices acquired by the WFI sensor on board the CBERS-4, CBERS-4A, and AMAZONIA-1 satellites.

1.2 Objective

Explore different temporal approaches for classifying burned areas in the Brazilian Cerrado, using the NIR band, spectral indices, and time series supervised classification based on regular 500 m cells as geographic objects.

1.2.1 Specific objectives

a) Build Analysis Ready Data (ARD) datasets with remote sensing data from 2020 to 2022 for the Cerrado present in the Chapada dos Veadeiros National Park using WFI imagery acquired by brazilian satellites.

b) Assess the performance of time series supervised classification with Random Forest on annual, semi-annual and multi-temporal datasets.

c) Understand the performance of classifications using the NIR band and the BAI, EVI, GEMI, NDVI and NDWI spectral indices.

d) Compare the generalization results of the generated multitemporal models with the MCD64A1 and AQM1km burned area products.

2 THEORETICAL BACKGROUND

2.1 An overview of the Brazilian Cerrado conceptions

The Cerrado is the second largest Brazilian biome, or phytogeographic domain, and its climate is characterized by dry winters and rainy summers under the Aw (tropical wet and dry or savanna climate) Köppen-Geiger classification (MMA, 2017). An important ecosystem service provided by the Cerrado is the carbon storage. According to Sawyer et al. (2016), 70% of the Cerrado biomass is underground. Cattle, annual crops such as soybeans, corn and cotton, biofuels (sugar cane), charcoal, fire and monocultures are threats to the ecosystems serviced offered by this biome.

Several definitions regarding the Brazilian natural regions classification have been proposed during the last two-hundred years (RIBEIRO; WALTER, 1998), and there is no consensus on whether the Brazilian Cerrado should be considered a biome or a phytogeographic domain. One general definition describes the Cerrado as a mosaic of distinct environments in which phytophysiognomies from three biomes coexist in a vegetation density gradient (COUTINHO, 1978; COUTINHO, 2006). A similar classification was elaborated by Eiten (1983).

The Cerrado, while a phytogeographic domain, represents an extensive natural area where the tropical grassland, savanna, and seasonal forest biomes are present (BATALHA, 2011). According to this interpretation, a biome would be understood on a global scale and a phytogeographic domain on a subcontinental scale. Campo Limpo is the phytophisiognomy comprising grassland formations, Campo Sujo, Campo Cerrado and Cerrado Sensu-Stricto are savannic environments and the Cerradão represents the forest formations. Figure 2.1, adapted from Coutinho (1978), exemplifies this biomass density gradient.

Figure 2.1 - The Cerrado phytophysiognomies according to Coutinho (1978).

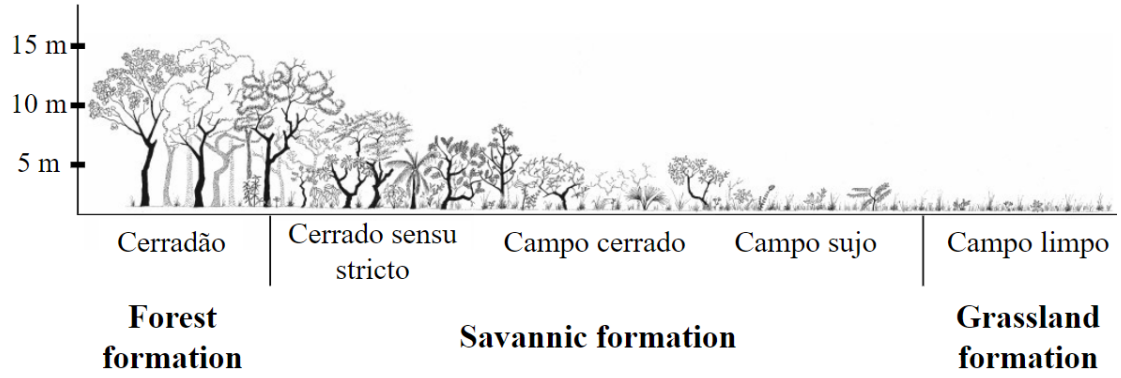

Source: Adapted from Gottsberger and Silberbauer-Gottsberger (2018).

According to the IBGE, the Cerrado is a xeromorphic vegetation biome characterized by a seasonal climate with the driest months occurring from May to September (PIVELLO, 2011). The IBGE defines a biome on a regional scale, based on shared geo-climatic conditions and a common natural history, resulting in environments with unique biodiversity, but not homogeneous (IBGE, 2012). Under this conception, grassland, savanna, and forest formations are not considered separate biomes but rather the primary vegetation formations found within the Brazilian Cerrado.

Another established concept that aggregates local details was proposed by Walter (1986) and Ribeiro and Walter (1998). According to their definitions, the Cerrado has eleven general phytophysiognomies containing twenty-three different vegetation types. Due to the pragmatism of this classification system, despite the no consideration of quantitative data, several researchers have adopted and used this useful concept as reference to comprehend and describe the Cerrado (PINHEIRO; DURIGAN, 2012).

The official definition was given in the Technical Manual on Geosciences, Number 1 (Brazilian Vegetation). In 2017, the "Forest Reference Emission Level" (FREL-Cerrado) was published (MMA, 2017), adopting the IBGE classification as the reference for the biome carbon estimation. In an effort to establish compatibility between the classification systems proposed by Walter (1986), Ribeiro and Walter (2008) and IBGE (2012), Valeriano (2017), in the context of REDD+ (Reducing Emissions from Deforestation and Forest Degradation), proposed the framework summarized in Table 2.1.

Table 2.1 - Compatibility of phytophysiognomies suggested by Valeriano (2017).

Formation	**Group (RIBEIRO; WALTER, 2008)**	**Vegetation class (IBGE, 2012)**
Grassland	Open grassland	Woody-grass savanna
	Shrub grassland	Savanna park
	Rupestrian grassland	
Savanna	Tipical cerrado	Wooded savanna
	Rupestrian cerrado	Savanna park
	Cerrado park	
	Palmland	Fluvial and/or lacustre influenced vegetation
	Vereda	
Forest	Tall woodland	Forest savanna
	Gallery forest	Seasonal forest
	Eyelash forest	
	Dry forest	

Source: Valeriano (2017).

2.1.1 Fires in the Cerrado

The majority of the Brazilian Cerrado biodiversity depends on fire (Figure 2.2). Natural wildfires have been occurring, at least, during the last four million years in the Cerrado, and fire has been a natural selection factor that has led to most of the flora being fire-resistant due to morphological and physiological adaptations (NASCIMENTO, 2001). It is also important to emphasize that natural fires occur between three and six years, and that human-induced wildfires have different characteristics and have negative impacts on the Cerrado (RAMOS-NETO; PIVELLO, 2000; JÚNIOR et al., 2014).

Figure 2.2 - Ecological relationship between Brazilian biomes and fire and detected fire-foci for 2022 per state present in the Cerrado.

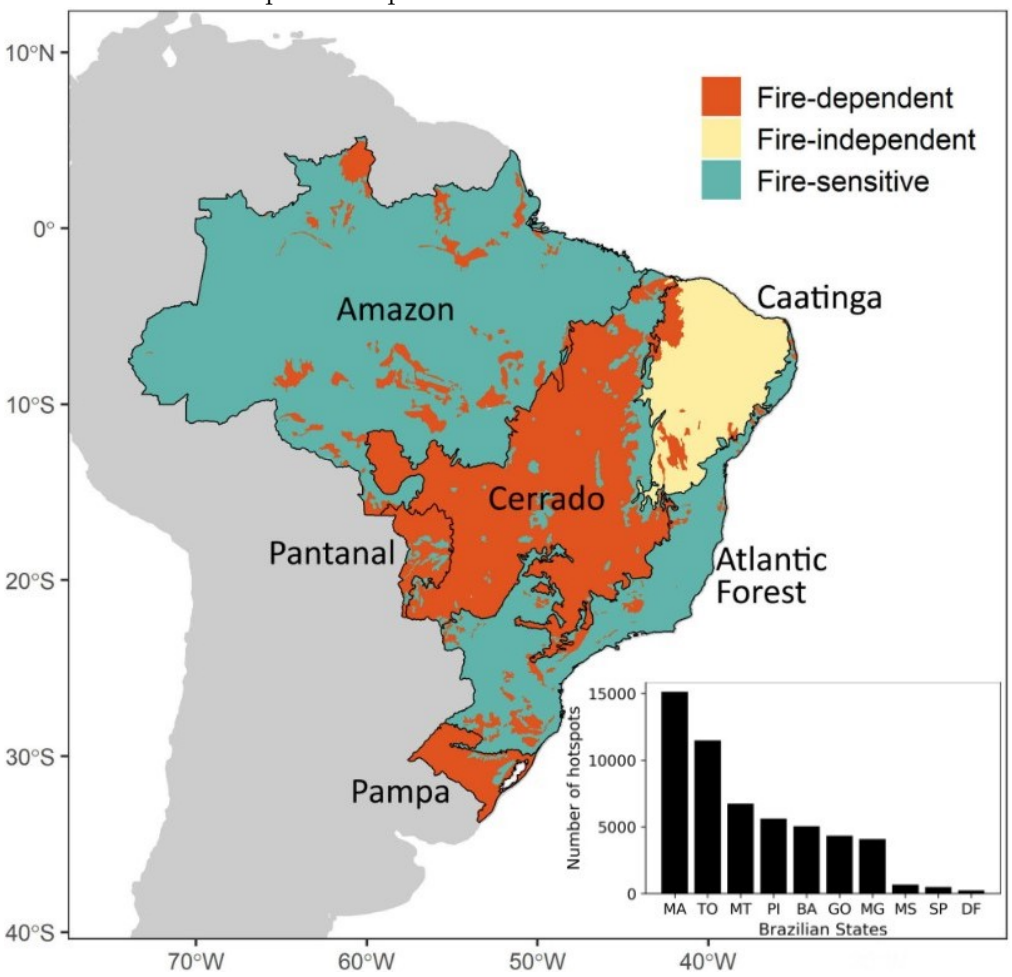

Source: Adapted from Pivello et al. (2021).

When analyzing the fire-foci of 2022 by states containing Cerrado vegetation, we observe that, except for Mato Grosso (MT), the four states with the highest number of hotspots identified by the INPE reference satellite (INPE, 2023b) are located in

the MATOPIBA region. While most of its phytophysiognomies have fire-resistant adaptations, natural fires are exceptions, and wildfires caused by human factors negatively affect its natural dynamics, leading to problems related to biodiversity loss and fragmentation (FIDELIS et al., 2018).

During a wildfire, the combustion process primarily involves the consumption of organic vegetation, which influences the fire intensity. It has a relationship with the fuel's calorific value, and different types of vegetable fuel can lead to variations in flame temperature, spread rate, and persistence (KEELEY, 2009). Although the primary environments of the Cerrado are categorized as fire-dependent, they still face risks. Additionally, the Cerrado's zero-fire policy has shown ineffectiveness and may potentially amplify the negative effects of wildfires (BARRADAS et al., 2020; DURIGAN et al., 2020), requiring new approaches for reducing environmental losses.

A historical debate involving fires in the Cerrado concerns the assumption that the use of managed fire to control densification and maintain the natural dynamics of grassland and savanna phytophisiognomies. Prescribed fire has been shown to be effective in preventing catastrophic fire events, such as those that occurred in the Cerrado in 2017, by controlling biomass growth (FIDELIS et al., 2018). Moreover, this practice has the advantage of combating the spread of exotic species, while providing fire-resistant vegetation with environmental conditions that ensure their natural dynamics (DURIGAN; RATTER, 2016).

According to Schmidt et al. (2016), the Integrated Fire Management (IFM) was first implemented in Brazil in 2014. One of its principles is conducting prescribed early burnings at the beginning of the dry season. The authors mention that IFM helps reduce the amount of fuel, resulting in a mosaic with varying levels of post-fire regeneration. Forestry brigade teams conduct the entire process, and these fires tend to be of low intensity and spread, as they do not completely consume the available fuel and are generally extinguished at night due to favorable conditions.

Essentially, as explained by Barradas et al. (2020), the debate between the zero-fire policy and the managed use of fire in savannas is global. In the context of the Cerrado, the benefits of IFM in preventing intense events potentially caused by humans are recognized and formally adopted in conservation units managed by the Chico Mendes Institute for Biodiversity Conservation (ICMBio), which engages in training local communities, since IFM considers both science and society in its approaches (BERLINCK; LIMA, 2021). Currently, Project Law 1818/2022, which establishes a national policy for IFM, is in the process of approval (BRASIL, 2022).

2.2 Fire monitoring and assessment using remote sensing

Fire is the result of combustion, an exothermic chemical reaction that occurs rapidly when a given fuel composed of oxidizable material reacts with a given oxidant element, such as oxygen gas (SCHMIDT-ROHR, 2015). The necessary factors for initiating and sustaining combustion are the presence of an ignition source, fuel available at the combustion temperature, and the presence of oxidant in sufficient concentration (HOFFMAN et al., 2021). Fire releases its own energy and light.

Radiance is the main measurement of RS and corresponds to the reflection or emission of energy that a sensor is able to detect (NOVO; PONZONI, 2001). Based on the interaction of electromagnetic radiation coming from targets, and received by a sensor, RS is able to describe the spectral characteristics of targets in the Earth system in specific regions of the electromagnetic spectrum according to the spectral resolution of the sensor and the position of the spectral bands (JENSEN, 2009).

Regarding RS analysis applied to wildfires, Penha (2018) describes two main types of fire-based products: heat-related products (active fire) and products focused on the biophysical changes observed in the burned vegetation (burned area). It is important to highlight the distinction between an active fire, which is the instantaneous product of combustion characterized as a thermal anomaly, and a burned vegetation area, which represents post-fire surface conditions. Specific regions contain information about the characteristics of these different targets in the electromagnetic spectrum.

While the energy emitted during the combustion process can be detected by RS in the thermal infrared and denotes active fire hotspots (SZPAKOWSKI; JENSEN, 2019), detecting burned areas is possible by analyzing a wider spectral range, including the visible region (NEGRI et al., 2022), and the near and shortwave infrared. Consequently, the optimal techniques for generating products related to active fires or burned areas for environmental monitoring depend on the specific characteristics of the sensor, such as imagery acquisition periodicity.

For example, Figure 2.3 provides an overview of the Operational Land Imager (OLI) and the Wide Field Imager (WFI) sensors. The OLI, onboard Landsat8/9 satellites, has a spatial resolution of 30 m for bands between the visible (0.4 μm - 0.7 μm) and the infrared (0.7 μm - 2.4 μm) regions, but its panchromatic band allows the acquisition of fused images with pixels of 15 m, while the thermal band has a spatial resolution of 100 m. The WFI sensor, onboard Brazilian satellites, has spatial resolutions of 55 m and 64 m and it provides four multispectral bands (BGR NIR).

Figure 2.3 - Comparison between OLI and WFI spectral and spatial resolutions.

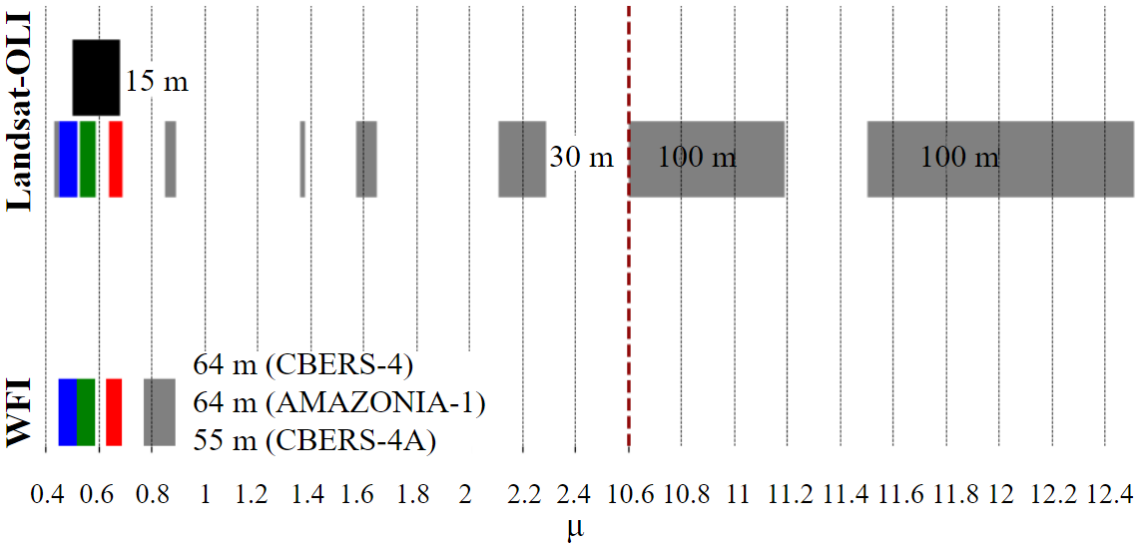

The OLI sensor operates in regions of the electromagnetic spectrum that are not covered by the WFI sensor, such as the shortwave infrared (SWIR) and thermal infrared (TIR) bands. This comparison illustrates how the sensor's specifications can affect analysis based on orbital RS. While the SWIR and TIR bands are useful for mapping burned areas and detecting active fires on the Earth's surface (CHUVIECO et al., 2002), other factors need to be considered, especially when a sensor has lower spectral resolution, as in the case of the WFI on board Brazilian satellites.

2.2.1 The WFI sensor

According to Epiphanio (2009), the CBERS are satellites of continuity, which means that one objective of this series of satellites is to ensure the continuity of images with similar characteristics over time. The first CBERS satellite was launched in 1999, and currently CBERS-4 and CBERS-4A are operational. AMAZONIA-1, the first satellite to be entirely designed, integrated, tested, and operated by Brazil, was launched in 2021. Table 2.2 shows the general chronological history of the Brazilian satellites.

Table 2.2 - Chronology of the Brazilian satellites.

CBERS-1	**CBERS-2**	**CBERS-2B**	**CBERS-3**	**CBERS-4**	**CBERS-4A**	**AMAZONIA-1**
1999	2003	2007	2013	2014	2019	2021

Source: Adapted from Oldoni (2022).

The WFI family sensors began with CBERS-1 and, although they have undergone technological improvements, there has been a continuity in the regular provision of images from these sensors over time. In fact, it was only with CBERS-3 that the WFI sensor could not operate due to problems with the launch of the satellite. In the first generation (CBERS-1, CBERS-2 and CBERS-2B), the WFI sensors had a spatial resolution of 260 m, temporal resolution between 3-5 days and two spectral bands (red and near-infrared) (EPIPHANIO, 2009).

This sensor has been improved since CBERS-3 to a spatial resolution of 64 m and four bands (blue, green, red and near-infrared), while maintaining the temporal resolution. The spatial resolution of the WFI on board CBERS-4A is 55 m due to the difference in altitude between the CBERS-4 and CBERS-4A satellites. Some national initiatives, such as the Brazil Data Cube (BDC), currently provides Analysis Ready Data (ARD) data cubes based on WFI multi-dimensional with a spatial resolution of 64 m (FERREIRA et al., 2020).

BDC is an example of a RS application based on the processing of medium resolution imagery acquired by Brazilian satellites and the provision of ARD. According to Picoli et al. (2020), these data cubes enhance environmental monitoring capabilities, such as deforestation mapping, wildfire studies and temporal LULC analysis. BDC also uses the Sentinel-2/MSI (multispectral Instrument) Landsat-8/OLI (Operational Land Images), Landsat-8/TIRS (Thermal Infrared Sensor), CBERS-4/MUX (multispectral Camera) and AQUA-TERRA/MODIS (Moderate Resolution Imaging Spectroradiometer) sensors to generate ARD data cubes.

Besides CBERS-4 and CBERS-4A, which are jointly operated and maintained by Brazil and China, AMAZONIA-1, the first satellite designed entirely in Brazil, was launched in 2021. It represents a strategic Brazilian technological asset for planning related to natural resources and environmental factors, particularly in the Amazon region (SILVA et al., 2022)). This satellite carries the WFI sensor with a spatial resolution of 64 m and a temporal coverage of 5 days, and the data combination from these three satellites allows the country to have a constellation of WFI sensors capable of providing images every 1-3 days (OLDONI, 2022).

Despite having the same technical specifications, the WFI sensors on board the three satellites exhibit variations in their response functions attributed to differences in right and left optics. Even if images of a same location are captured under identical conditions, there may still be variations in the generated images due to these optics differences. Otherwise, these satellites use different grids, and the spatial resolution

is not the same between them, as previously observed (OLDONI, 2022).

Oldoni (2022) proposed inter-satellites methods for co-registration and spectral normalization to produce robust time series based on WFI images from CBERS-4, CBERS-4A and AMAZONIA-1. The author mentions in the study "Harmonization of WFI data from CBERS-4, CBERS-4A and AMAZONIA-1 satellites for agricultural applications", that WFI images observed displacements between CBERS-4 and AMAZONIA-1 to Sentinel-2 reached 1.45 pixels (93 m), and that between CBERS-4A to Sentinel-2 reached 2.5 pixels (138 m). It indicates geometric inconsistencies between the CBERS and AMAZONIA-1 platforms.

In this sense, it is worth noting that, despite the apparent challenge of harmonizing the WFI data, available RS-based approaches can reduce noise between images from these satellites. Surface reflectance (SR) transformation functions, as suggested by Oldoni (2022), are subject to calibrations that vary according to the study area. Furthermore, it is essential to have in mind the objectives of an application to determine the appropriate level of data processing and harmonization. Certain levels of noise may be tolerated in some cases, while they may not in others (RADOUX; BOGAERT, 2017).

2.2.2 Spectral behavior of burned areas

During wildfires, fire mainly consumes organic material from vegetation fuel, affecting the intensity of fire events in natural ecosystems. Depending on the calorific value of the burning fuel, flames can reach higher temperatures, spread more easily or take longer to cool down (MCARTHUR; CHENEY, 2015). Keeley (2009), in the article "Fire intensity, fire severity and burn severity: a brief review and suggested usage", distinguishes the difference between the concepts "fire intensity" and "burn severity". Figure 2.4 illustrates these concepts that are related to the active fire and burned area RS-based products.

Basically, fire intensity describes the combustion process by which flames release energy, or in the case of fire line intensity, the rate of heat transfer per unit length of fireline. Both fire severity and burn severity refer to ways of measuring impacts by analyzing post-fire charred plant material, with burn severity the most used in RS applications. Active fires and burned area sub-products have different targets on the terrestrial surface. While thermal infrared bands assess fire hotspots and measure physical properties of fire, such as fire radiative power (FRP), burned areas can be mapped with sensors that operate in shorter waves of the electromagnetic spectrum.

Figure 2.4 - Visual examples of fire intensity and burn severity on vegetation.

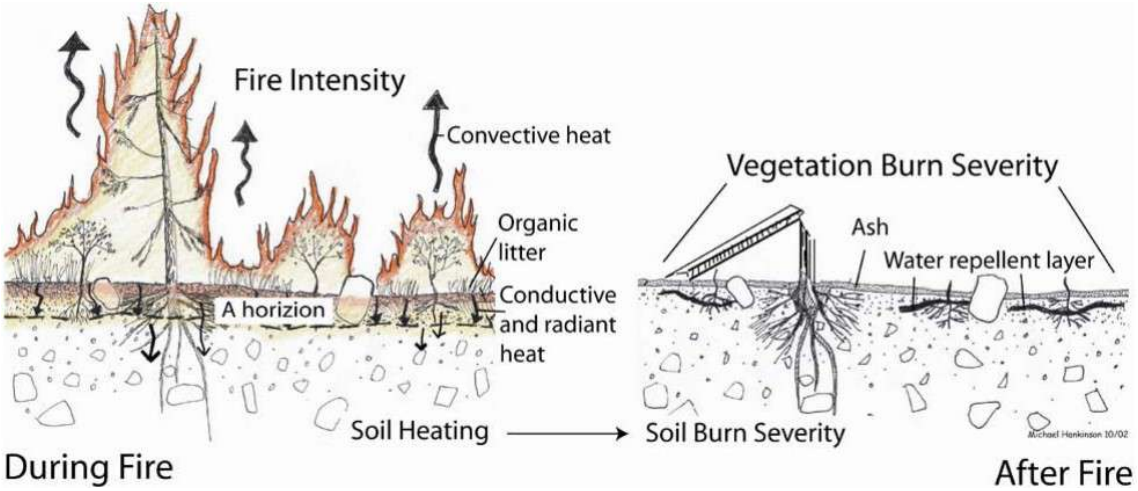

Source: Adapted from Pivello et al. (2021).

The range over which the spectral behavior of burned areas can be observed by RS depends on the number of bands a sensor has and their position along the electromagnetic spectrum. Burned areas do not have a unique spectral signature, because environmental factors, such as vegetation cover and pedology, affect its spectral response (BASTARRIKA et al., 2011; LEWIS et al., 2021). Bands positioned in the infrared region are the most common to identify and map these targets (PEREIRA et al., 2016) or to proceed spectral indices transformations to highlight burned areas.

Vegetation and pedology influence the spectral behavior of burned areas, as vegetation characterizes the available fuel (FRANKE et al., 2018) and pedology causes background effects on the signal, which varies according to the soil constituents (PEREIRA et al., 2016). Basically, there are two spectral patterns of this target on surface: areas with black and/or white ash and charcoal/charred material, detectable soon after the fire; and areas with changes in vegetation structure and abundance, detectable for a period ranging from days to months (PEREIRA et al., 1997).

In the visible region (0.4 μm - 0.7 μm), burned areas exhibit an increase in surface reflectance that gradually decreases over time. This decrease is attributed to the gradual reduction of ash cover and the increasing influence of bare soil and vegetation greening on the spectral signal detected by the sensor (PEREIRA et al., 2016). These observations differ from similar studies conducted in other natural formations, where, for example, burned areas in forests typically show an immediate decrease in reflectance in the bands located in this spectral region (LENTILE et al., 2006).

In the near-infrared (NIR) region (0.7 μm - 1.3 μm), the surface reflectance of

fire-affected areas is expected to decrease significantly, and it is attributed to the reduced amount of energy reflected by vegetation structures, which can be impacted at different levels of severity depending on their characteristics (PEREIRA et al., 1997; CHUVIECO et al., 2002). In addition to the NIR band, shortwave infrared and thermal bands are recurrent in equations of spectral indices applied to vegetation monitoring and burned areas mapping.

However, the sensor used does not always operate in these bands, as is the case with the WFI sensor. Based on the bands imaged by the reference sensor, it is possible to perform transformations in which the products highlight the spectral response of targets of interest. Spectral indices represent a fast way to obtain information from the use of two or more spectral bands, as it is a conceptually simple technique with high computational efficiency (PENHA, 2018). One of the main advantages of the WFI images is the almost daily revisit using the Brazilian satellite constellation, what justifies studies concern the viability of the WFI for mapping burned areas.

Table 2.3 lists some helpful spectral indices used for mapping burned areas using the four multispectral bands (BGR NIR) present in the WFI. The Burned Area Index (BAI) (CHUVIECO et al., 2002), Global Environment Monitoring Index (GEMI) (PINTY; VERSTRAETE, 1992), and the Normalized Difference Vegetation Index (NDVI) (ROUSE et al., 1974) use the red and NIR bands, while the EVI (HUETE et al., 2002) uses the blue, red and NIR bands. The Normalized Difference Water Index (MCFEETERS, 1996) uses both the green and NIR bands.

Table 2.3 - Spectral indices that enable the detection of burned areas based on the images derived from the WFI sensor.

Spectral index	Equation	Reference
NDVI	$\frac{\rho NIR - \rho Red}{\rho NIR + \rho Red}$	Rouse et al. (1974)
GEMI	$\gamma = \frac{2(\rho NIR^2 - \rho Red^2) + (1.5 * \rho NIR) + (0.5 * \rho Red)}{NIR + \rho Red + 0.5}$ $GEMI = \gamma * (1 - 0.25) - \frac{\rho Red - 0.125}{1 - \rho Red}$	Pinty and Verstraete (1992)
NDWI	$\frac{\rho Green - \rho NIR}{\rho Green + \rho NIR}$	McFeeters (1996)
EVI	$2.5 * \frac{\rho NIR - \rho Red}{(\rho NIR + C_1 * \rho Red - C_2 * \rho Blue + L)}$	Huete et al. (2002)
BAI	$\frac{1}{(0.1 - \rho Red)^2 + (0.06 - \rho NIR)^2}$	Chuvieco et al. (2002)

Sources: Rouse et al. (1974), Pinty and Verstraete (1992), McFeeters (1996), Huete et al. (2002), Chuvieco et al. (2002).

As mentioned, the potential to detect burned areas is reduced if a given sensor operates only in the visible and NIR regions. Many spectral indices applied to map this target use bands located along the infrared region. Despite these challenges, Pastor and Shimabukuro (2009) explored, in the article "Estimación de superficie quemada mediante la aplicación sinérgica de OBIA y SMA a imágenes WFI CBERS", the usage of the red and NIR bands of the WFI sensor for mapping burned areas based on Spectral Mixture Analysis (SMA) and Object-Based Image Analysis (OBIA).

2.2.3 Land cover change detection applied to map burned areas

Land can be understood as the place where all human activities occur (PARVEEN et al., 2018). Two other terms complement this concept in RS studies, "land use" and "land cover", and there is no global consensus on their definitions. Basically, on the surface land, humans can develop activities based on use, for example, food production, recreation and extraction of raw materials or natural resources, and this type of human-environment relationship is commonly referred to as land use, which is under human driving forces.

According to Meyer and Turner (1996, 238), land cover "is the biophysical condition of the land", such as "the kind and condition of the vegetation and other biota, the water, the soil, the artificial structures that cover its surface" (MEYER; TURNER, 1996, 238). The authors emphasize that land use alters land cover by converting or changing land cover to a qualitatively different state, by changing land cover conditions without full conversion, or by maintaining changed conditions over time. Parveen et al. (2018) highlight that non-anthropogenic forces also alter land cover.

Although there is not a unique globally used legend for land cover classes, there are proposals in the literature to standardize these classes according to different spatial scales. The Land Cover Classification System (LCCS), developed by the Food and Agriculture Organization (FAO), can be cited as a land cover legend system that can be modified by users according to their context. Examples of the eight major classes adopted by the LCCS include: cultivated and managed terrestrial areas; natural and semi-natural terrestrial vegetation; artificial surfaces and associated areas; bare area; artificial water bodies, snow and ice (GREGORIO, 2005).

Natural and artificial components on land are in a constant process of change. Changes on the Earth's surface can be gradual, such as the growth of biomass, or abrupt, such as the effects of fire on vegetation. Natural vegetation is a land cover class in different classification systems, and changes in it can be understood, by RS,

as qualitative changes in vegetation cover or as spectral and spatial movements over time (MILNE, 1988). In this sense, burned areas in natural vegetation represent abrupt and non-permanent changes in vegetation cover (SHIMABUKURO et al., 2020) and can be highlighted using vegetation or fire indices (LIU et al., 2020).

RS has provided land cover change detection (LCCD) applications since the 1990s using specific techniques and algorithms (WOODCOCK et al., 2020). However, Jin et al. (2013) argue that there is no single method universally adopted by the scientific community for detecting changes, especially when these applications aim to map changes at regional scales. Li et al. (2022) emphasize that more semantic information needs to be considered in regional mapping due to the scale and context. Some changes and burned area detection approaches use time series (ZHU, 2017; XU et al., 2022; LIU et al., 2023) and data mining (RAMO et al., 2018; WOOD, 2021).

The use of time series to map land cover changes with RS is an approach that requires attention due to seasonal differences, sun angle, phenological conditions of vegetation, clouds, and shadows, as these factors are some of the main sources of noise in time series based on satellite imagery (ZHU, 2017). In the article "Standardized Time Series and Interannual Phenological Deviation: New Techniques for Burned-Area Detection Using Long-Term MODIS-NBR Dataset", Carvalho-Júnior et al. (2015) applied time series to map burned areas in the Chapada dos Veadeiros National Park (CVNP), Goiás State, Brazil.

The CVNP is a conservation unit with phytophisiognomies of the Cerrado. Carvalho-Júnior et al. (2015) aimed to assess the effectiveness of the standardized time series and the interannual phenological deviation methods, utilizing the NDVI and NBR (Normalized Burn Ratio) spectral indices derived from MODIS imagery to identify and determine the timing of cover changes caused by fire analyzing the pixels temporal curves from 2001 to 2012. Carvalho-Júnior et al. (2015) highlight the challenges of mapping burned areas within the CNVP due to its diverse environments and non-forest cover.

Fires emit more carbon in savannas, with grasslands exhibiting faster fire spread. The negative correlation between Cerrado cover and fire, influenced by livestock and fuel loads, suggests the potential of the WFI, as there is a decrease in the reflectance surface in RGB bands during May and September for open vegetation (CHAVES et al., 2021). The high temporal resolution of the WFI allows time series construction that enables cover change detection, and this RS-based processing and analysis, aligned with the use of Machine Learning (ML) methods, has demonstrated good

results for land use and cover classifications (FERREIRA et al., 2020).

2.3 Artificial Intelligence in remote sensing applications

The recent advances, or popularization, of AI has promoted profound changes in social structures (MAKRIDAKIS, 2017). Although not necessarily a new concept, AI is currently attracting attention from society because, as it breaks new boundaries related to data management and pattern recognition (SEREY et al., 2023), for example, providing applications to optimize processes in several areas, AI also becomes a subject of debate related to the ways in which humans, and governments, incorporate its approaches to daily tasks (ZAJKO, 2022).

The ability to work with a great quantity of data and recognizing patterns are major benefits of using AI. This is important in RS because artificial satellites are constantly generating new data for Earth observation. Based on RS data, many environmental and social applications are possible, such as the study of natural phenomena and monitoring of agricultural crops, water quality, natural disasters and urban planning (ALDANA-MARTÍN et al., 2022). In the last few years, the AI technique of ML has become widely used in the environmental sciences (STROPPIANA et al., 2021), with applications in mapping burned areas (WOOD, 2021).

According to Tiwari et al. (2018, 1), ML is "a technology that allows computers to learn directly from examples and experience in the form of data". ML helps with the recognition of big data patterns, and uses them in predictions (LIU et al., 2018). There are two major categories in ML approaches, corresponding to "unsupervised learning" and "supervised learning". The first approach is more unpredictable, while supervised learning allows better expectations regarding the outputs once a model was trained based on human experiences (LIU et al., 2018). There are also hybrid approaches (MEHMOOD et al., 2022).

ML is efficient in studies related to LULC analysis and to disaster management, for example, as it provides models related to regression and classification problems in RS applications. In this sense, RS image classification based on ML can be performed by the unsupervised and supervised approaches. Unsupervised image classifiers, such as K-Means and Self-Organizing Map (SOM) algorithms, learn directly from the data without human sampling (unlabeled data), while humans participate by providing samples for training supervised classification models (labeled data). Random Forest (RF) is an example of a supervised classifier (MEHMOOD et al., 2022; MISHRA; DASGUPTA, 2022).

2.3.1 Random Forest

Random Forest (RF) is a nonparametric supervised classification algorithm based on decision trees. In this algorithm, two main parameters are defined *a priori*: the number of trees and the percentage of classification and validation samples. The process of choosing these samples, from the dataset informed by the user, is randomized and, therefore, the algorithm may employ different subtraining sets at each round (BREIMAN, 2001; KULKARNI; LOWE, 2016; BELGIU; DRĂGUŢ, 2016), *i.e.* for the construction of each tree.

RS-based data rarely satisfy the assumption of normal data distribution. In such cases, nonparametric classifiers, including RF, are widely used (BELGIU; DRĂGUŢ, 2016). Initially, for constructing an RS image classification based on an RF model, the first node of a decision tree starts with the entire set of samples, which is then divided into training and validation samples. The nodes split according to the decision rules and the input samples can be determined by parameters such as "nodesize" and "maxnode" that control the trees and the forest expansion (TYRALIS et al., 2019).

"Nodes", which are decision points in a decision tree, create "branches" that lead to the final points known as "terminal nodes" or "leaves". Terminal nodes represent predictable class labels and do not experience further splitting or division. With each new tree generated, the samples are randomized to ensure that different subsets are used in each round, understood as each tree construction. In the end, the ensemble of randomized decision trees forms a "random forest". The model is finally based on the vote of all trees, as exemplified by Figure 2.5 (KULKARNI; LOWE, 2016; TYRALIS et al., 2019; XI, 2022).

Using a ML approach, the nodes are split based on the available attributes used as input to classify the image. The algorithm mines the data and determines the most informative attributes for splitting the nodes. Evaluation of the splits can be performed using impurity indices, such as the Gini Index. It ranges from 0 to 1 and measures the impurity, or degree of class mixture, for each node (BREIMAN, 2001). For time series classifications, a dataset could be understood as a data cube, where each attribute could be interpreted as an observed day or as temporal metrics extracted from several days, depending on the data cube generation method (VIEIRA et al., 2022; KORTING et al., 2013).

Figure 2.5 - Example of a RF classification flow.

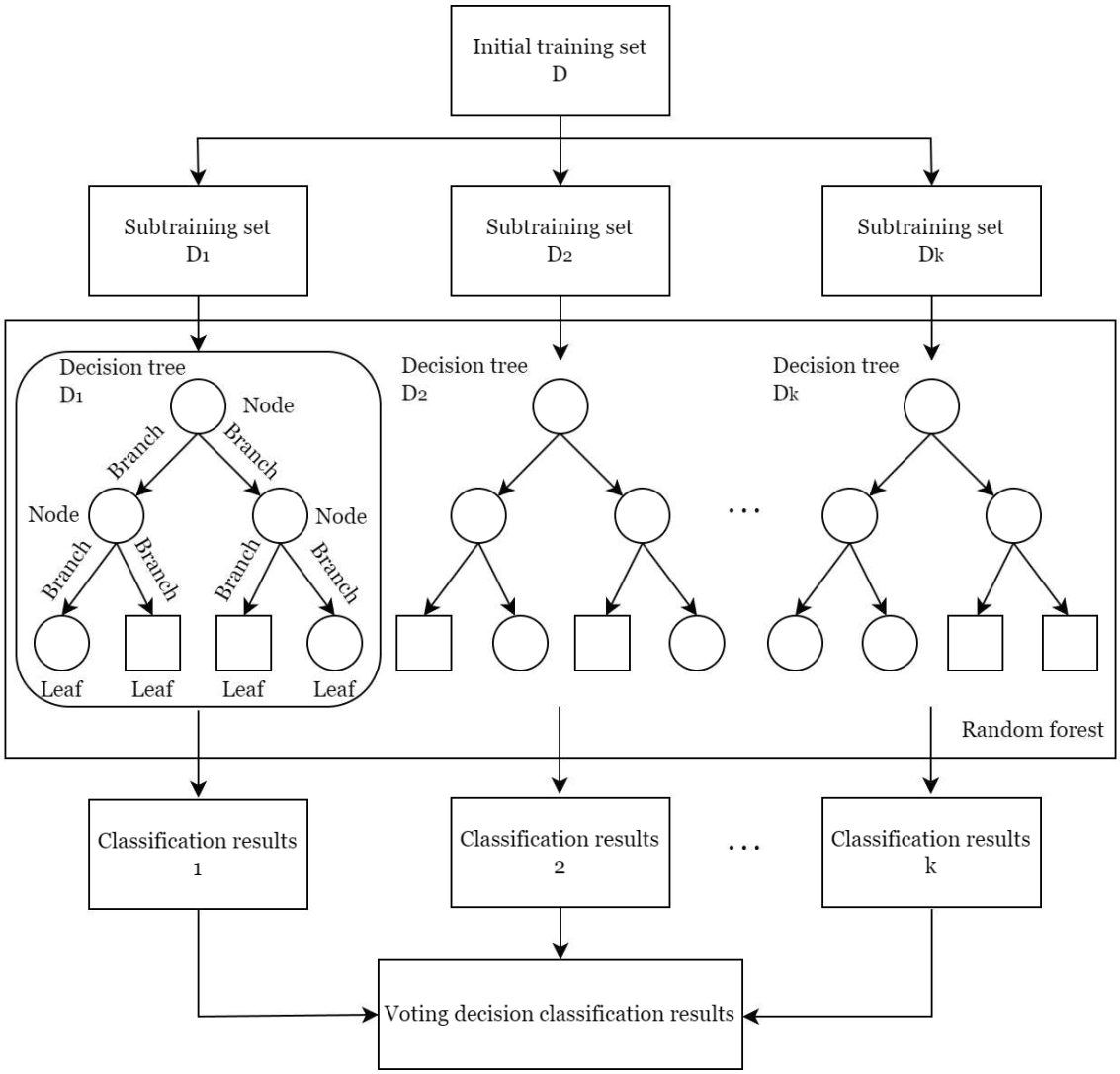

Source: Adapted from Xi (2022).

Ramo and Chuvieco (2017) discuss in the paper "Developing a Random Forest Algorithm for MODIS Global Burned Area Classification" some important points related to classifications of time series using RF for mapping burned areas. The authors highlight concerns about temporal generalization, specifically addressing the potential problems associated with training models using samples of burned areas from a single year and then applying them to other years. This paper cites the flexibility of RF regarding data integration from different sensors and scales and the low computational cost of this algorithm compared to other ML algorithms, such as Support Vector Machine (SVM).

2.3.2 Geographic Object-Based Image Analysis

According to Lang (2008), the objective of OBIA (Object-Based Image Analysis) is to represent the content of complex scenes in order to describe the reality present in images. The authors emphasize that human cognition and perception are involved in OBIA methods, which can use images from different contexts than RS applications. The term GEOBIA (Geographic Object-Based Image Analysis) emphasizes the contribution of GIScience (Geographic Information Science) components. Several studies, however, consider both terms as synonyms (BLASCHKE, 2010).

According to Hay and Castilla (2008), GEOBIA is a subdiscipline of GIScience that studies methods for partitioning images into semantic objects based on spectral, spatial and temporal features. Blaschke (2010) clarifies that GEOBIA became a widespread topic in scientific research around the 2000s, but that its principles, such as edge detection, segmentation, attribute extraction and classification, were already used before in other scientific fields. In this approach, image-objects, such as regular geographical cells, represent the central methodological element.

Segmentation produces image objects based on properties of the ground components (BLASCHKE, 2010; LANG, 2008), but there is also the possibility of using regular cells, or "superpixels", as image-objects. Pixels within RS images contain specific radiometric values and spatial objects are formed when there are relatively homogeneous aggregates of pixels (BLASCHKE et al., 2014). Segmentation techniques have historically focused on high spatial resolution images, but there is the possibility of working with time series (GÓMEZ et al., 2011), and the use of regular grids is a way of standardizing processes and analysis in the face of a large volume of data.

The idea behind cells or superpixels is to reduce data dimensionality, especially for high spatial resolution images or time series, due to spatial correlation between nearby pixels and the amount of images. Superpixels could be understood between the pixel level and the object level (CSILLIK, 2016). Gómez et al. (2011) highlight that the object-oriented approach in change detection minimizes co-registration errors and allows including context relations, which is especially useful when only BGR NIR bands are available (JOHANSEN et al., 2010).

Each class is comprehended as a semantic entity in object-oriented image classification. Until image-objects are labeled into hierarchical classes, in a process that requires human perception and knowledge, they have no real-world representational meaning (BLASCHKE; STROBL, 2001). Although GEOBIA is not a new disci-

pline, it has been dealing with AI techniques and approaches since its conception, and object-based classifications have the potential to achieve better performance and higher accuracies than pixel-based classifications (WHITESIDE et al., 2011).

2.4 Burned area products

One of the ways to understand the behavior and impacts of fire in landscapes is using burned area products provided by RS techniques (GAVEAU et al., 2021). Burned area products have the potential to be used in estimating carbon emissions and in identifying drivers of wildfires, allowing interventions to mitigate impacts, prevent and control wildfires, rehabilitate burned areas, and monitor the international goals of climate conferences.

According to Mouillot et al. (2014), the 1980s were the moment when scientific approaches based on RS emerged for mapping burned areas on Earth's surface with satellite images. Currently, burned area products with global coverage are available, such as the case of the MCD64A1, based on MODIS, or burned areas products targeted to specific geographic regions, such as the AQM1km from INPE that has coverage to Brazil. Table 2.4 contains some products of burned areas available for download or online queries.

Table 2.4 - Examples of burned areas products.

Product	**Sensor**	**Spatial**	**Temporal range**	**Developer/ Provider**	**Reference**
MCD64A1	MODIS	500 m	2000-present	NASA	Giglio et al. (2018)
AQM1km*	MODIS	1,000 m	2002-present	INPE/ LASA-UFRJ	Libonati et al. (2015)
Copernicus Burnt Area v3	Sentinel3-OLCI/ SLSTR	300 m	2020-present	C3S	Roy et al. (2019) Tansey et al. (2008)
MapBiomas Fire c2 v1	Landsat series	30 m	1985-2022	MapBiomas Project	MAPBIOMAS FOGO (2023)
AQM30m	Landsat series	30 m	2001-2021	INPE	Melchiori et al. (2015)
FireCCI51	MODIS	250 m	2001-2020	ESA	Chuvieco et al. (2018)
GABAM	Landsat series	30 m	1990-2020	GEE	Long et al. (2019)

NASA: National Aeronautics and Space Administration; LASA: Laboratory for Environmental Satellite Applications; UFRJ: Federal University of Rio de Janeiro; OLCI: Ocean and Land Colour Instrument; SLSTR: Sea and Land Surface Temperature Radiometer; C3S: Copernicus Climate Change; ESA: European Space Agency; GEE: Google Earth Engine.

Giglio et al. (2018) contextualize the monthly and global coverage product MCD64A1, from MODIS sensor collection 6 (C6), as a refinement of the methodology applied in MCD45A1 C5 and C5.1 products. MCD64A1 is based on a hybrid algorithm that uses time series with daily surface reflectance and active fire data. Rodrigues et al. (2019), when analyzing the MCD64 collections for the whole Cerrado, identified uncertainties in the southern portions, due to vegetation properties. Despite detecting small burned areas better than other collections, they tend to increase inclusion errors.

It is important to highlight the products provided by Brazilian initiatives. The Algorithm Theoretical Basis Document (ATBD) contains the step-by-step methodology developed to detect burned areas by the MapBiomas project. Based on images acquired by the satellites of the Landsat series during the period from 1985 to 2022, and utilizing deep learning, MapBiomas maps monthly and annual burned areas in the Brazilian biomes (ALENCAR et al., 2022). The ATBD guideline is constantly adapted due to changes that improve its methodology

The AQM1km product, provided by INPE and available in the Queimadas database (INPE, 2023b), is based on images from the MODIS sensors and covers the entire country. The AQM1km products aim to provide an overview of fire events in the Brazilian biomes, using cells of 1 km x 1 km, accessible through online queries. On the other hand, the monthly AQM30m product allows data download for priority areas in the Cerrado but does not encompass other biomes or the entire Cerrado.

Different results are expected when comparing these products due to methodological differences, as each product is the result of specific algorithms and techniques and may be suitable for analysis at different scales, or even have different mapping periodicities (PESSÔA et al., 2020; SHIMABUKURO et al., 2020). Consequently, according to Humber et al. (2019), the validation of these products with independent references with minimal error is necessary to comprehend their quality. Reference maps, in most cases, are generated through image interpretation by human analysts.

A validation with independent data can be conducted by estimating the true positives, true negatives, false positives and false negatives between the reference and the predicted in order to get metrics such as precision, recall, F1-score and F2-score (CORCORAN et al., 2015; RADOUX; BOGAERT, 2017). Intersection over Union (IoU) is used to compare two sets of finite data, and it is described by the equation: $J(A,B) = \frac{A \cap B}{A \cup B}$, varying from 0 to 1, with 1 representing the maximum similarity between both sets (LABATUT; CHERIFI, 2012; FLETCHER; ISLAM, 2018).

3 STUDY AREA

3.1 Chapada dos Veadeiros National Park (CVNP)

The Chapada dos Veadeiros National Park (Figure 3.1), established in 1961 by the Federal Decree No. 48.875, is located in the Brazilian state of Goiás and covers the municipalities of Alto Paraíso de Goiás, Cavalcante, Nova Roma, Teresina de Goiás, São João da Aliança and Colinas do Sul. An important characteristic of the CVNP is its function of supplying several aquifers and tributaries located in the highest portion of the Central Plateau in the Tocantins Araguaia Hydrographic Region, that integrates the Upper Tocantins basin (ICMBIO, 2021).

Figure 3.1 - Location of the CVNP and its surroundings within a buffer zone of 10 km.

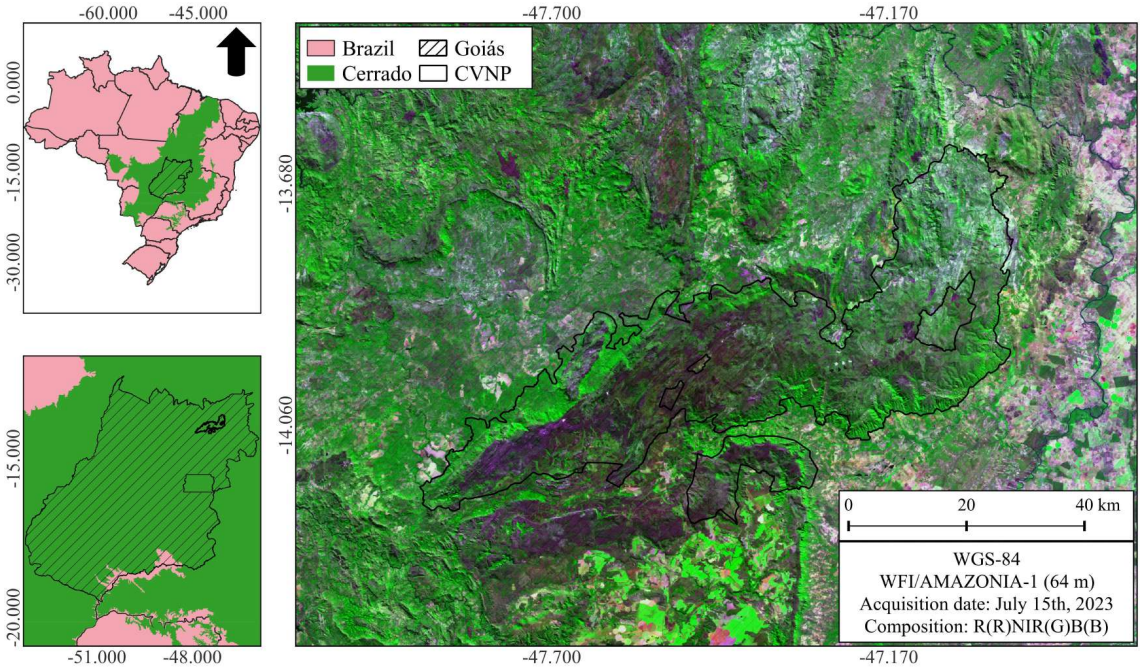

The CVNP has been target of expansions and reductions, and its current configuration, with 240,611 ha, was defined in 2017 by the Decree of June 5. The organization responsible for its management is the Chico Mendes Institute for Biodiversity Conservation, linked to the Ministry of Environment and Climate Change (MMA). The main phytophysiognomies of the study area are related to savanna formations (LOEBMANN, 2008), but the Management Plan (ICMBIO, 2021) clarifies that there is a diverse mosaic of vegetation present in the area. Figure 3.2 shows the phytophysiognomies of the study area according to the IBGE's mapping (IBGE, 2012).

Figure 3.2 - Vegetation cover of the study area.

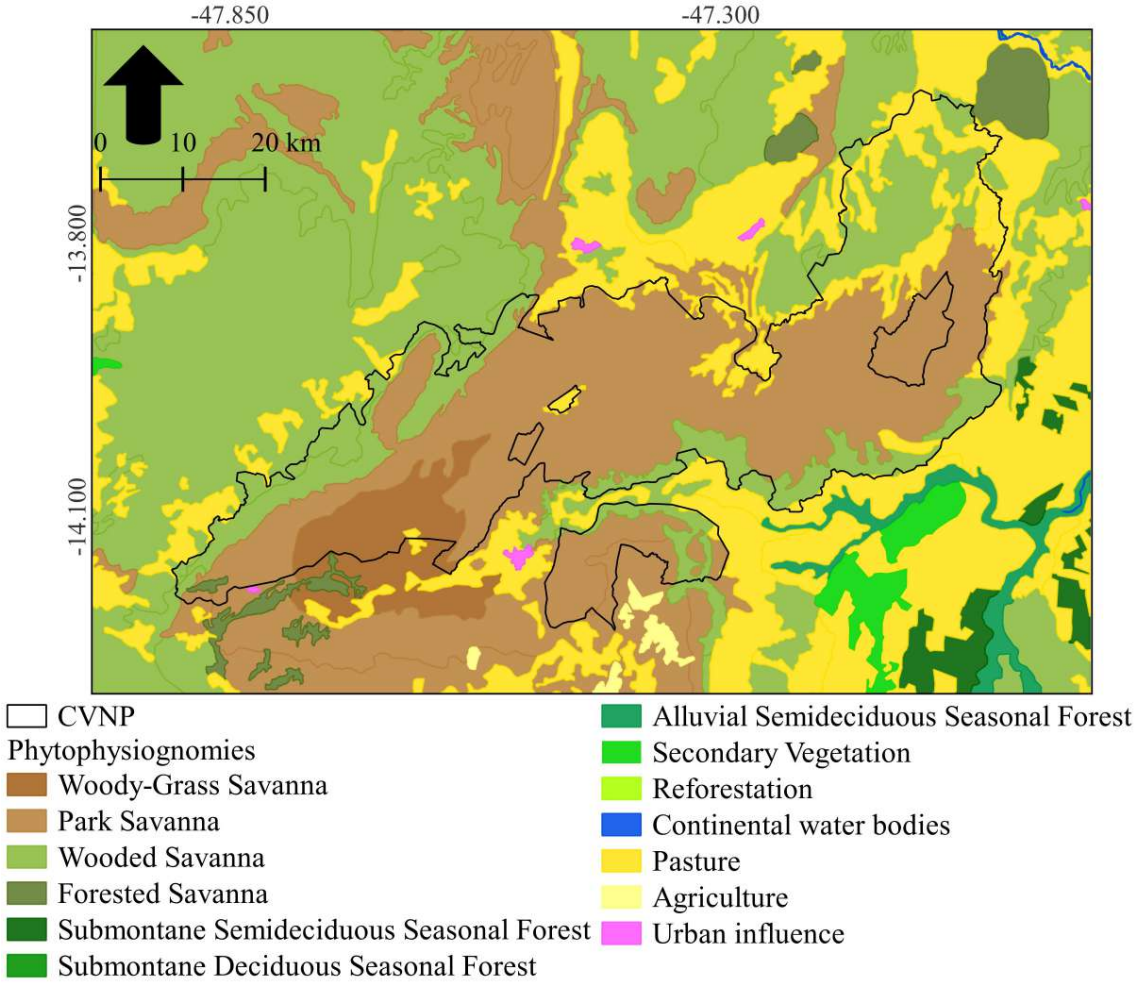

Source: IBGE (2012).

The CVNP is a World Natural Heritage Site recognized by the United Nations Educational, Scientific and Cultural Organization (UNESCO) (RIBEIRO, 2020), but around 78% of the CVNP burned in 2017 Fidelis et al. (2018), year in which the CVNP area was expanded to its current configuration. Table 3.1 illustrates the percentage of the Conservation Unit's area affected by fires between 2007 and 2021.

Table 3.1 - Recent historical burning events inside the CVNP.

Year	**Percentage of areas in CVNP affected by fire**
2007	68%
2010	78%
2015	22%
2017	27.44% (80% of the old area)
2018	6%
2019	15%
2020	15%
2021	15%

Source: ICMBIO (2022).

Currently, this conservation unit has a IFM planning implemented. Since 2017, prescribed burns have been employed within the UC to reduce the risk of destructive fires. These burns, in accordance with the Integrated Fire Management Plan, are strategically conducted during the rainy season to reduce fuel availability. Figure 3.3 shows the deforestation from 2020 to 2022 detected by the INPE's Project for Monitoring Deforestation in the Legal Amazon (PRODES) (INPE, 2023c), and the fire foci provided by the BDQueimadas' reference satellite (AQUA M-T/MODIS) (INPE, 2023b).

Figure 3.3 - Accumulated deforestation and fire foci detected in the study area.

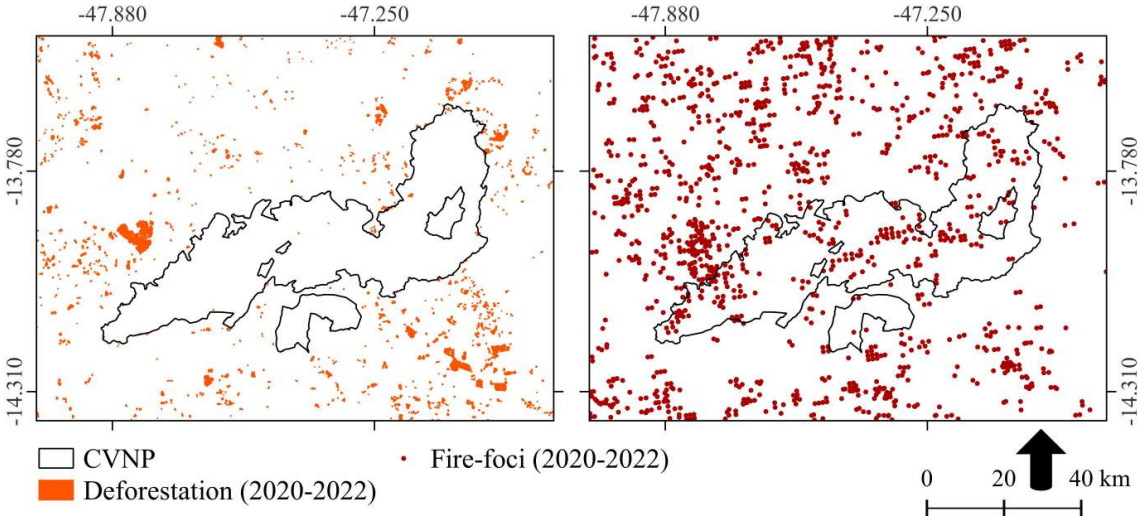

Source: INPE (2023b), INPE (2023c).

Table 3.2 shows the annual fire foci detected in and around the CVNP (with a buffer zone of 10 km) by INPE using the MODIS sensor on board the AQUA satellite. The years 2020, 2021, and 2022 designate the analysis period of this study. We observe that 2022 had the highest number of detected fire foci (332), followed by 2020 (319) and 2021 (283). RS-based data indicate that the region has been annually affected by fires that eventually reach and spread to the Cerrado within the CVNP, justifying the choice of this study area, since it also contains a diversity of phytophysiognomies (LOEBMANN, 2008).

Table 3.2 - Annual fire foci detected by the INPE's satellite reference.

Year	Number of fire foci
2020	319
2021	283
2022	332

Source: INPE (2023b).

4 METHODOLOGY

4.1 Pre-processing

We used the Python programming language to construct a time series from 2020 to 2022 based on images from the WFI sensor on board the CBERS-4A, CBERS-4 and AMAZONIA-1 satellites, available at the INPE image catalog (INPE, 2023d), considering the bounding box of our study area. Our general pre-processing steps are described in Figure 4.1.

Figure 4.1 - Pre-processing steps.

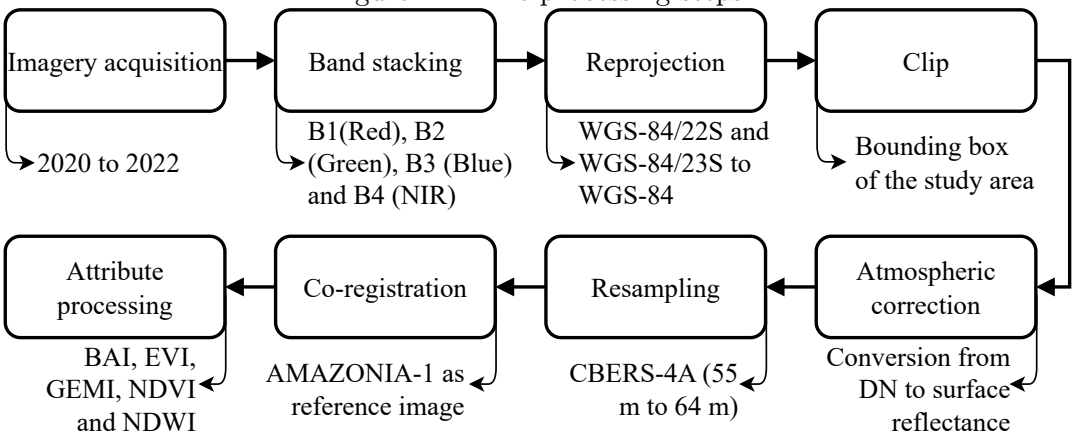

4.1.1 Imagery acquisition

We downloaded images from INPE's catalog using the Cbers4asat Python plugin (RUSSO, 2023), enabling serial image downloads via API query parameters. We acquired images from January 1st, 2020, to December 31st, 2022, from the WFI sensor on CBERS-4, CBERS-4A, and AMAZONIA-1 satellites, in Level-4 (L4), which includes corrected images with digital elevation model and control points. We set the cloud coverage to 100% because it reflects the global cloud coverage, which is not necessarily the same as the coverage in our study area.

The CVNP has eight paths directly observed by the CBERS-4A swath at row 132, and eight paths observed by CBERS-4 at row 117. For AMAZONIA-1, only one path covers the area at row 17. Based on all these criteria, we downloaded a total of 382 images. Figure 4.2 shows the satellites paths and rows that cover our study area. The amount of images per year is different. In 2020, only CBERS-4A images were included, in 2021 both CBERS-4A and AMAZONIA-1 and in 2022 the INPE catalog used as reference began to include CBERS-4 images.

Figure 4.2 - Paths and rows by satellite.

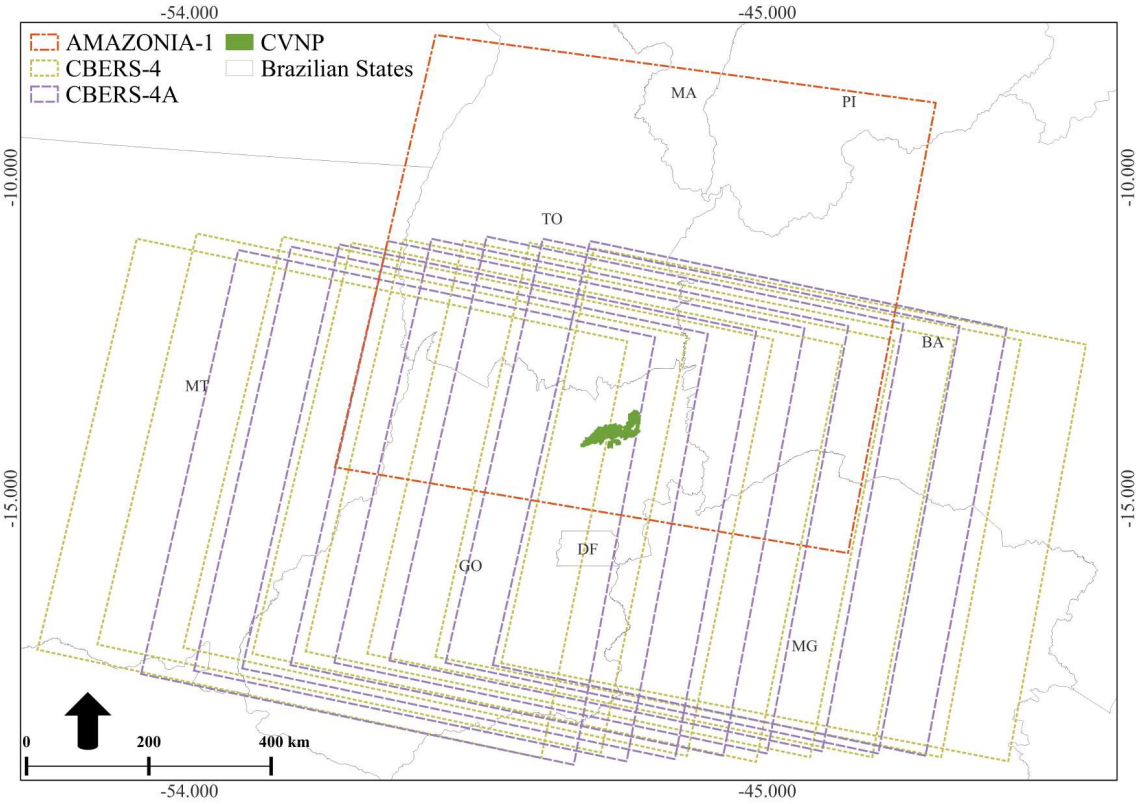

4.1.2 Band stacking

INPE provides the Blue (band 1), Green (band 2), Red (band 3) and NIR (band 4) bands for download, and the analyst has to merge them, if necessary, into a raster with the desired bands. We merge the four bands of all images using the Os module and the Rasterio library in order to standardize the band sequence as Red (1), Green (2), Blue (3) and NIR (4), according to the RGB NIR composition, directly from the computer's local using Jupyter Notebook. We performed *a posteriori* image-by-image visual analysis and excluded those with high cloud coverage in our study area.

4.1.3 Reprojection

Using the same Python libraries as before, we reprojected the bands from WGS84-22s (EPSG: 32722) and WGS84-23s (EPSG: 32723) to WGS84 (EPSG: 4326) using the nearest neighbor resampling method, which ensures the preservation of the original digital number (DN) values. All images from the WFI sensor were acquired in metric coordinate systems, and we standardize them to the WGS84 geographic coordinate system in order to avoid processing inconsistencies.

4.1.4 Clipping

The coordinates of the bounding box were defined based on a buffer zone of 10 km from the boundaries of the CVNP. After data reprojection, we clipped the images to the bounding box (xmin: '-46.8888', ymin: '-13.54311', xmax: '-47.9897', ymax : '-14.2958') to optimize further processing, since our spatial focus was the CVNP region. In this step, we used the Os, Rasterio and Shapely libraries.

4.1.5 Atmospheric correction

We used Python to implement an atmospheric correction method based on DOS (Dark Object Subtraction), as described by Chavez-Jr (1988) and Nunes et al. (2019). Table 4.1 lists the technical specifications by band of the WFI sensors used in a first radiometric calibration step, which aims to convert the data from digital numbers to radiance. We estimated the gain and offset factors for the isolated spectral bands for each image of our time series applying Equations 4.1 and 4.2

Table 4.1 - Technical specifications of the WFI sensor.

Band	**Wavelength (μ)**	**Maximum radiance (lMax) (W m-2 sr-1)**	**Minimum radiance (lMin) (W m-2 sr-1)**	**Maximum reflectance (pMax) (ρ)**
Blue	0.45 - 0.52	343.4	35.3	0.6
Green	0.52 - 0.59	361.2	25.7	0.7
Red	0.63 - 0.69	306.9	12.9	0.7
NIR	0.77 - 0.89	243.4	8.9	0.8

Source: Epiphanio (2009).

$$g = \frac{lMax - lMin}{DNMax - DNMin} \tag{4.1}$$

$$o = lMin - g \cdot DNMin \tag{4.2}$$

g: band gain factor; o: band offset factor; $lMax$: maximum radiance; $lMin$: minimum radiance; $DNMax$: maximum digital number; $DNmin$: minimum digital number.

We applied the linear function described by Equation 4.3 to convert the original band data from DN to Top-of-Atmosphere (TOA) radiance.

$$lb = g \cdot DN + o \tag{4.3}$$

lb: pixel radiance value output; DN: pixel digital number input.

We used the Ephem (RHODES, 2011) library for Python to estimate the Earth-Sun distance for each image, according to the strings from the image title that correspond to the date information. At this point, we set the observer's latitude and longitude to the centroid of our study area (x: -47.368721, y: -13.959796) and standardized the image acquisition time to 13:55:00 UTC, based on analysis of the image metadata available in the INPE catalog. We implemented Equation 4.4 for estimating the solar irradiance.

$$ESUN = \pi \cdot d^2 \cdot \frac{lMax}{pMax} \tag{4.4}$$

$ESUN$: extraterrestrial solar irradiance; d^2: Earth-Sun distance; $lMax$: maximum radiance; $pMax$: maximum reflectance.

Equation 4.5 was applied to estimate the dark object radiance required by the DOS method:

$$L1\% = \frac{0.01 \cdot ESUN \cdot \cos(\theta)}{\pi \cdot d^2} \tag{4.5}$$

$L1\%$: dark object radiance; θ: solar zenith angle.

We performed the subtraction between the generated rasters containing the dark object radiance and the images containing the TOA radiance to attenuate atmospheric noises. We applied Equation 4.6.

$$lp = lb - L1\% \tag{4.6}$$

lp: subtraction radiance.

Finally, we converted the results of the radiation subtraction to surface reflectance using Equation 4.7.

$$\rho = \frac{\pi \cdot (lb - lp) \cdot d^2}{ESUN \cdot \cos(\theta)} \tag{4.7}$$

ρ: surface reflectance.

We also used the Numpy (HARRIS et al., 2020) library and the Math module to

process matrices and perform the necessary mathematical operations.

4.1.6 Resampling

We chose to resample the CBERS-4A images from 55 m to 64 m to equalize the spatial resolution of the three satellites because it allows us to retain the CBERS-4 and AMAZONIA-1 data without resampling. We used the nearest neighbor as the resampling method. For each resampled image, we set the grid from the WFI on board AMAZONIA-1 as reference to fit the generated data with 64 m from the CBERS-4A satellite. We performed the grid alignment between CBERS-4 and AMAZONIA-1 data keeping the WFI on AMAZONIA-1 as the grid reference.

4.1.7 Co-registration

Our study area is fully covered by seven paths from CBERS-4 and CBERS-4A satellites, and it is partially covered by one additional path for each one of these satellites, resulting in a total of eight paths per satellite. On the other hand, AMAZONIA-1 covers the entire area with a single path and row. We perform automatic co-registrations to compose a time series using images from Brazilian satellites, aiming to minimize shifts in observation angles within paths of a same satellite and between different satellites.

We employed the Python library Arosics (Automated and Robust Open-Source Image Co-Registration Software) (SCHEFFLER, 2017) to this processing. We set the "grid resolution" parameter to 30 and the "window size" parameter to 400 x 400. The grid resolution refers to the number of pixels used to search for control points (CP), and the window size defines the size of the kernel. Using these parameters a total of 2772 CPs were plotted, but not necessarily all of them were used due the Arosics algorithm disregards possible outliers or points of non-correspondence.

Table 4.2 lists all the target WFI images from the CBERS-4A and CBERS- 4 satellites used to estimate the shifts based on images from AMAZONIA-1. We defined the reference image from July 30, 2021 to co-register the CBERS 4A images, and we prioritized close acquisition date and low cloud coverage. Our time series does not have WFI images from CBERS-4 in 2021, so we defined the AMAZONIA-1 image of June 30, 2022 as reference. The Arosics library allows using the obtained models to register other images. Based on the generated models for each image in Table 4.2, we applied them to the rest of our time series.

Table 4.2 - Target images used for co-registration.

Satellite	Path /Row	Target image
CBERS-4A	132 - 203	05 july 21
	132 - 204	30 june 21
	132 - 205	25 may 21
	132 - 206	21 july 21
	132 - 207	16 july 21
	132 - 208	10 june 21
	132 - 209	06 july 21
	132 - 210	01 july 21
CBERS-4	117 - 154	01 aug 22
	117 - 155	03 june 22
	117 - 156	30 june 20
	117 - 157	01 june 21
	117 - 158	24 june 22
	117 - 159	21 june 22
	117 - 160	18 june 22
	117 - 161	06 aug 22

4.1.8 Attributes processing

In this study, we adopted the BAI, EVI, GEMI, NDVI and NDWI spectral indices to highlight burned areas and to construct the datasets for training and testing the Random Forest algorithm. We used the Os, Rasterio and Numpy libraries and all the implemented equations can be found in Table 2.3.

4.2 Processing

Figure 4.3 shows the flowchart that describes the methodological steps that were followed in the processing of the data.

Figure 4.3 - Processing steps.

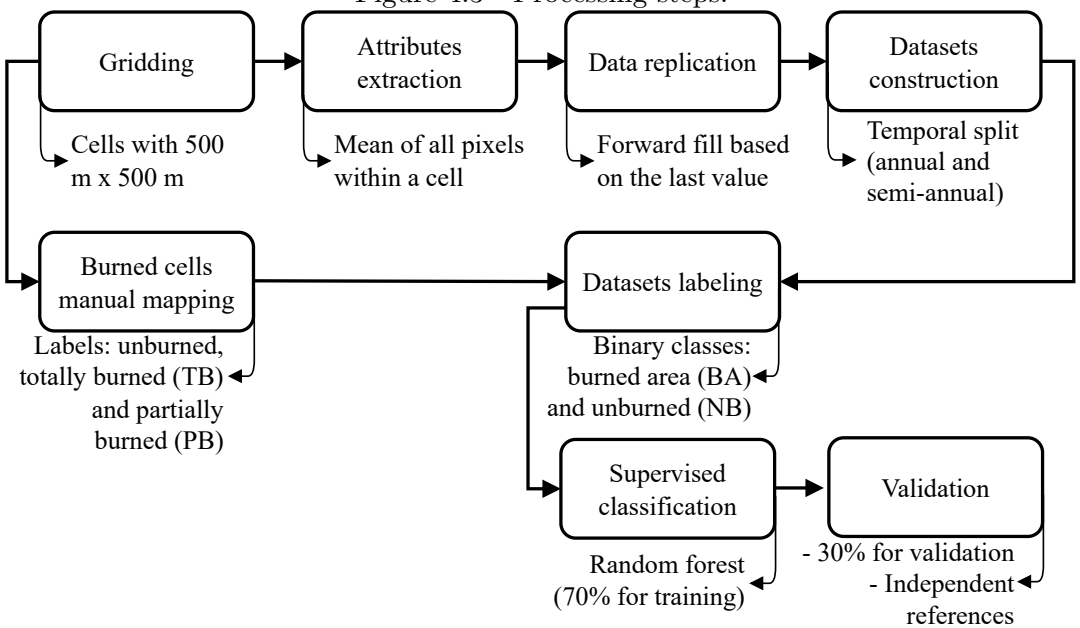

4.2.1 Gridding

We adopted the MODIS spatial resolution as the minimum mapping unit (MMU) to generate a vector grid with 500 m x 500 m cells size. The generated regular grid has 239 columns x 163 rows, which gives a total of 38,957 cells. Although this process degrades the spatial resolution of the data, it reduces the dimensionality of the datasets and allows validation with the MCD64A1 product.

4.2.2 Burned cells manual mapping

Figure 4.4 illustrates the general anatomy of burning vegetated areas. Considering that the MMU in this study refers to the size of the cells in the regular grid, we can see that, given the anatomy of burned areas, not all cells may be totally affected by fire, since cells located on the edges of the main affected area, such as on the fingers and flanks, may be partially affected, as well as unburned islands. Consequently, considering the spatial regularity of the grid, we chose to include partially affected cells as this can affect the supervised classification process and analysis, due to the potential higher heterogeneity of this target.

Figure 4.4 - Anatomy of a forest fire.

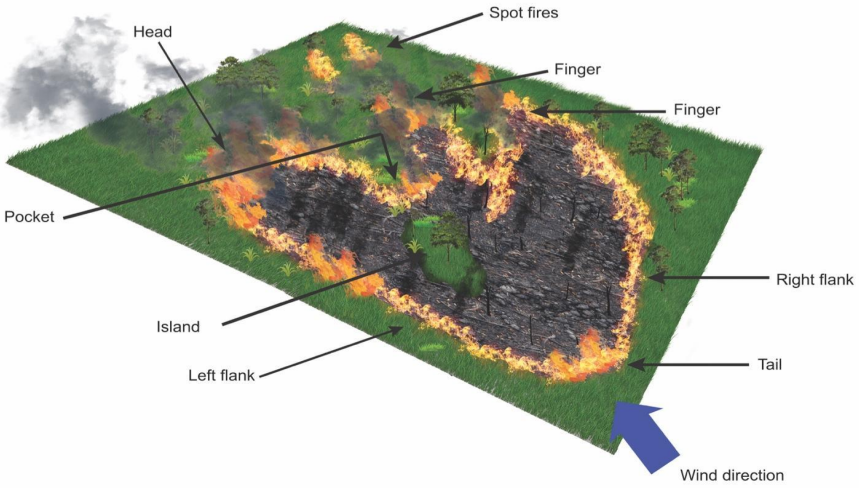

Source: NFCC (2023).

We manually collected burned areas within the cells identified by image interpretation for the years 2020, 2021 and 2022 using QGIS 3.22.12. Based on these cells we labeled them as “unburned” (NB), “totally burned” (TB) and “partially burned” (PB). The visual image analysis process was conducted using the R(R)NIR(G)B(B) color composition to enhance burned areas, which are highlighted as dark areas. Figure 4.5 shows an example of a burned area imaged by CBERS-4A on October 5, 2020, and it also has visual examples of NB, TB and PB cells.

Figure 4.5 - Examples of totally and partially burned cells, and unburned cells.

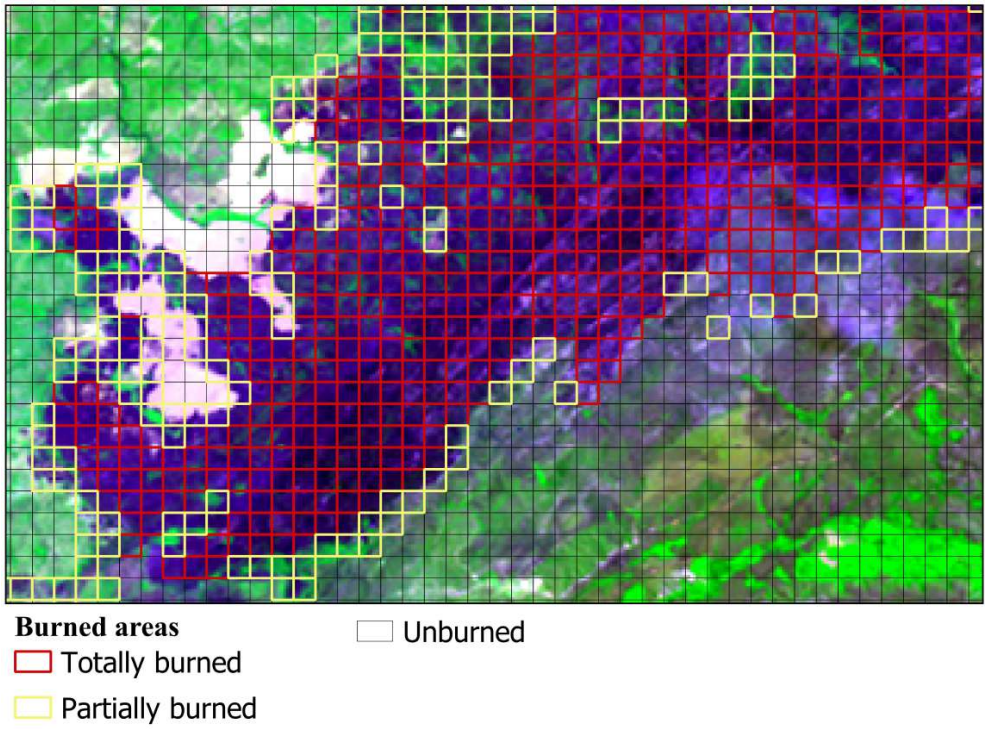

For each cell labeled as TB or PB, the corresponding image date was recorded in the attribute table. Although there are two labels for fire-affected cells, both refer to a single class called “burned area” (BA), while NB cells designate the other class, called “unburned” (NB). All subsequent supervised classifications were performed based on these binary classes (ba and nb): using only TB cells as samples of the BA class and TB plus PB cells concatenated into a single set of samples of the BA class.

4.2.3 Attributes extraction

We used the Os and the Geopandas (JORDAHL et al., 2020) and Rasterstats libraries in Python to extract the mean zonal statistics from the pixels within the cells, taking into account 235 valid observations from 2020 to 2022. We adopted the mean of the NIR band, BAI, EVI, GEMI, NDVI and NDWI spectral indices as reference to extract the pixel values within the cells.

4.2.4 Data replication

All the 235 valid observations were integrated over the period from January 1st, 2020 to December 31, 2022. As mentioned earlier, the number of images available in the INPE catalog is different for each year, and therefore, after extracting the attributes, we obtained datasets that can be understood as irregular time series, because the observations are not equally spaced in time. Burned areas are under-

stood as abrupt and not permanent changes on the Earth's surface, and among the available interpolation techniques, we choose forward fill replication because these targets do not necessarily occur between two observations. So, every gap between two valid observations was filled with the value of the first observation.

4.2.5 Datasets construction

At this stage, after replicating the data for each information layer (NIR, BAI, EVI, GEMI, NDVI, and NDWI), annual ARD datasets comprising 1,096 columns were generated, with each column representing one day. We then divided them into three annual and six semi-annual ARD datasets for each of the six information layers, totaling 18 annual ARD and 36 semi-annual ARD datasets. The purpose of testing the accuracy of the annual and semi-annual models is to analyze whether there is a possible difference in the models created with more or fewer attributes available to the classifier.

To standardize the observations per ARD dataset, we decided to omit December 31 from the annual dataset for 2020 because it is a leap year. In this context, we also excluded July 1 from the dataset for the first half of 2020. For the second semester datasets, we removed December 31. Consequently, the annual datasets have 365 observations and the semi-annual datasets have 182 observations. Table 4.3 shows the time intervals covered by the resulting ARD datasets. Finally, the files were saved in CSV (Comma-Separated Values) format to optimize subsequent processing.

Table 4.3 - Days by dataset considering the annual and semi-annual ARD time series created with WFI images.

	2020*	2021	2022
Start date	jan. 01	jan. 01	jan. 01
End date	dec. 30	dec. 31	dec. 31
Days	365	365	365
	2020-1	2021-1	2022-1
Start date	jan. 01	jan. 01	jan. 01
End date	jun. 30	jul. 01	jul. 01
Days	182	182	182
	2020-2	2021-2	2022-2
Start date	jul. 02	jul. 02	jul. 02
End date	dec. 30	dec. 30	dec. 30
Days	182	182	182

* Leap year.

4.2.6 Datasets labeling

Given the previously manually mapped mask of burned cells with the categorical labels TB, PB or NB assigned to the cells of the grid with the respective day when the burned cell was mapped, we used the Pandas (MCKINNEY, 2010) library to split all TB and PB cells according to the time range shown in Table 4.3 and merged the columns with all TB cells and with all TB plus PB cells into the ARD datasets. All other cells refer to the NB label. We chose to only explore generalizations based on multitemporal datasets, but the models generated with semi-annual ARD datasets were analyzed according to classifier accuracy metrics.

We generated two multitemporal datasets for each information plan with samples from BA and NB classes. These datasets comprise 70% randomly selected TB cells and 33.33% randomly selected NB cells for each year. Our goal was to include 1/3 of all NB cells from each year in a new dataset to reflect the quantitative characteristics of the annual datasets. At the same time, by selecting 70% of all BA cells, we aimed to obtain substantial samples from all years in order to evaluate the efficiency of generalizations without exhausting all BA cells. We repeated the same process using the concatenation of TB and PB cells as samples for BA to construct the second dataset. Figure 4.6 illustrates these steps.

Figure 4.6 - Construction of annual generic datasets.

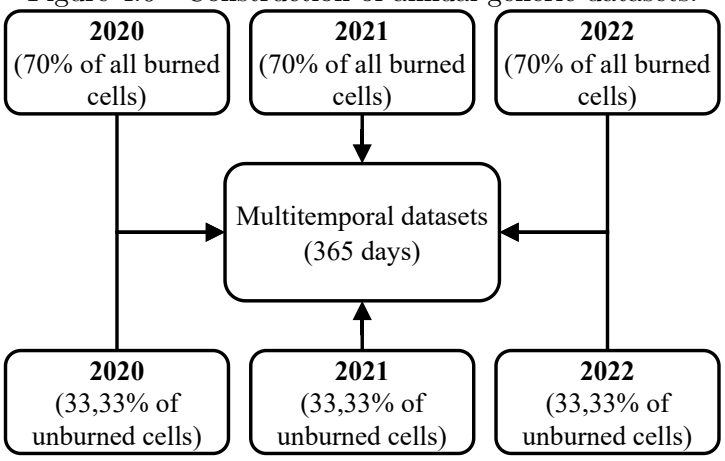

4.2.7 Supervised classification

We adopted the Random Forest algorithm to explore possibilities of binary classifications with ARD and multitemporal datasets. ARD time series refer to classifications performed on the datasets after labeling, according to Table 4.3. Multitemporal datasets refer to datasets created by concatenating random observations from more

than one annual ARD dataset, as explained earlier. No information from different plans (NIR, BAI, EVI, GEMI, NDVI and NDWI)nwas combined.

The routine for classification was implemented using the Scikit-learn library (PEDREGOSA et al., 2011) for Python. Regardless of the dataset, we chose to run five classifications instead of a single one, then we estimated the average of the metrics. In each simulation, the sample set of burned areas remained the same (full sample universe), but based on the size of this set, we randomly sampled a set with the same size for NB cells. Additionally, once both sets were defined, we selected 70% for training and 30% for validation. For each simulation, the best hyperparameters were adopted according to Table 4.4, structured with empirical values.

Table 4.4 - Hyperparameters grid used as input to search for the best values using GridSearchCV.

Parameter			
n_estimator	100	200	300
max_depth	3	5	7

The "n_estimator" parameter determines the number of trees and "max_depth" defines the maximum depth of the trees. An important point to emphasize is that all training rounds used a set of equal-sized samples from BA and NB classes, i.e. the input data was exactly balanced and it was defined based on the size of the set of samples with burned cells (TB or TB plus PB), according to the datasets. For each classification, we saved the best hyperparameters chosen from the tuning grid, the confusion matrix, and the results for accuracy, precision, recall, and F1-score. Additionally, an example of a generated decision tree was saved for each classification.

4.2.8 Validation

We performed two types of validation analysis: validation of the generated models based on the training (70%) and test (30%) samples, and validation of the classifications by comparing them to the manually created reference maps. These reference maps designate the mapping with all homogeneous cells totally affected by fire and the mapping created by the concatenation of all totally cells affected by fire and all partially burned cells, identified by image interpretation. Figure 4.7 describes the metrics used for validation and the analysis approaches based on temporal (semi-annual and annual) datasets and multitemporal models generated with TB and TB plus PB as samples of the burned area class.

Figure 4.7 - Validation and analyses approaches.

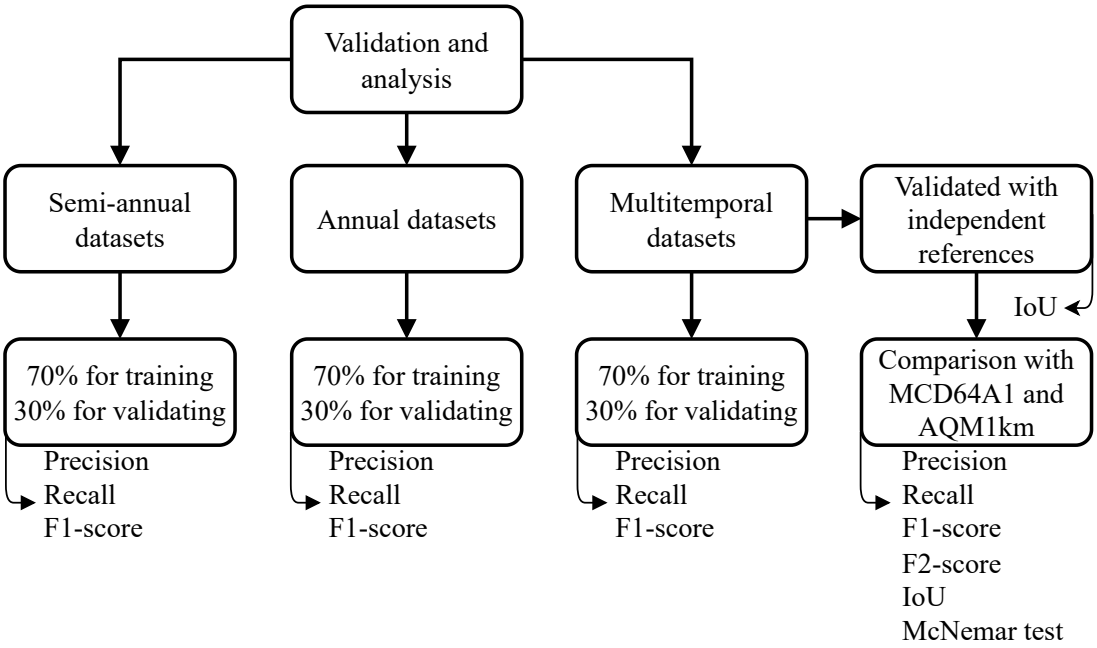

Based on the quantification of true positives (TP) and false positives (FP), we estimated the precision metric (Equation 4.8), and based on TP and false negatives (FN), we estimated the recall (Equation 4.9). We chose to explore the results of the F1-score (Equation 4.10), which is a harmonic accuracy metric between classes, and the F2-score (Equation 4.11), which gives more weight to the recall and can better describe how well the classifier can correctly detect burned cells. We used the IoU comparison to comprehend the overall correspondence (Equation 4.12).

$$\text{Precision} = \frac{TP}{TP + FP} \tag{4.8}$$

$$\text{Recall} = \frac{TP}{TP + FN} \tag{4.9}$$

$$\text{F1-score} = \frac{2 \cdot \text{Precision} \cdot \text{Recall}}{\text{Precision} + \text{Recall}} \tag{4.10}$$

$$\text{F2-score} = \frac{(1 + \beta^2) \cdot \text{Precision} \cdot \text{Recall}}{(\beta^2 \cdot \text{Precision}) + \text{Recall}} \tag{4.11}$$

β: adjusts the balance between precision and recall, with β set to 2, emphasizing recall and favoring scenarios where recall is more critical than precision.

$$\text{IoU} = \frac{Intersection}{Union} = \frac{TP}{TP + FP + FN} \tag{4.12}$$

Finally, we used the Scikit-learn library to perform the McNemar test between pairs of classifications. The null hypothesis (H0) is that neither classification performs better than the other when compared to the same reference mapping.

5 RESULTS AND DISCUSSION

5.1 Time series description

After removing images with high cloud coverage, images acquired by swaths that do not cover half our study area and images that are repeated on the same day, the number of images was reduced from 382 to 235 valid observations. Figure 5.1 shows a density chart constructed based on this time series. It can be seen that the number of valid observations increases over time. The year 2020 consists entirely of CBERS-4A images, 2021 contains images from CBERS-4A and AMAZONIA-1 and the most recent CBERS-4 images were included in the INPE catalog in 2022.

Figure 5.1 - Density of the time series from 2020 to 2022 constructed based on WFI images on board the CBERS-4, CBERS-4A and AMAZONIA-1 satellites available in the INPE catalog.

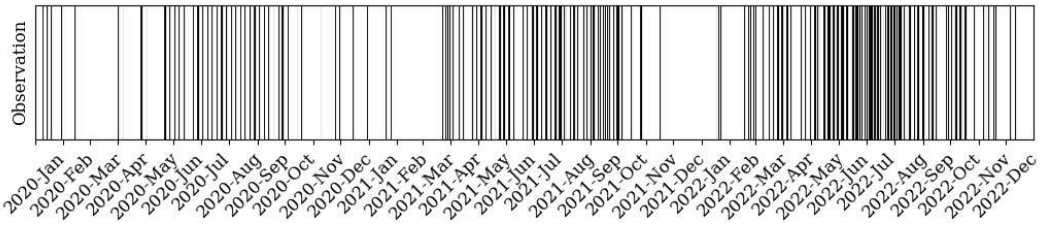

Figure 5.2a shows the total of valid observations per satellite and Figure 5.2b describes the operational temporal range of each satellite. Images from the CBERS-4A satellite are exclusively available through the INPE catalog adopted as reference in this study, and 122 images were acquired by this satellite. Our study area has been covered by AMAZONIA-1 since March 27, 2021, and a total of 75 images compose our time series. Although the CBERS-4 satellite has been in operation since 2014, it was not until May 9, 2022, that its most recent images from our study area were added to the catalog, and our time series includes 38 images acquired by this satellite

Figure 5.2 - Quantitative and temporal description per satellite.

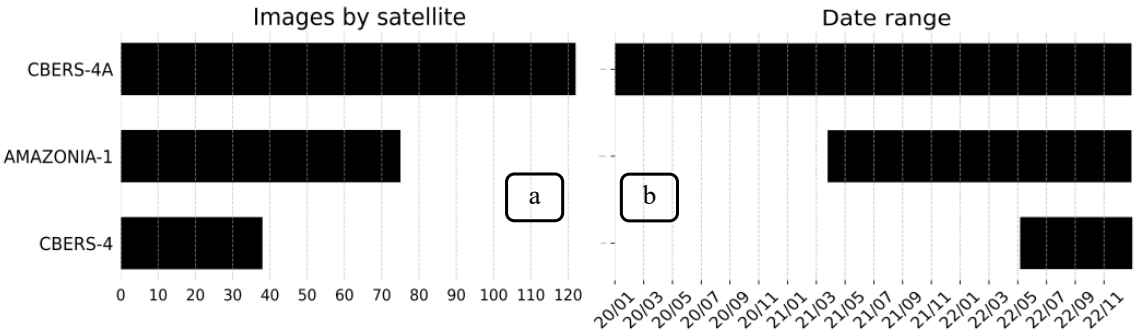

a: quantity of images per satellite; b: temporal availability of images in the catalog.

Figure 5.3 shows the imagery distribution per month along the entire time series. A total of 50 images were considered in 2020, 72 in 2021, and 113 in 2022. The months with the lowest number of observations are between November and March, and this is due to the presence of clouds in the rainy season. The peak of valid observations occurs in July, and the period from April to October concentrates the largest number of useful images. This is the period when most fires occur in the Brazilian Cerrado and is therefore the main window for observing burned areas.

Figure 5.3 - Number of valid observations per month.

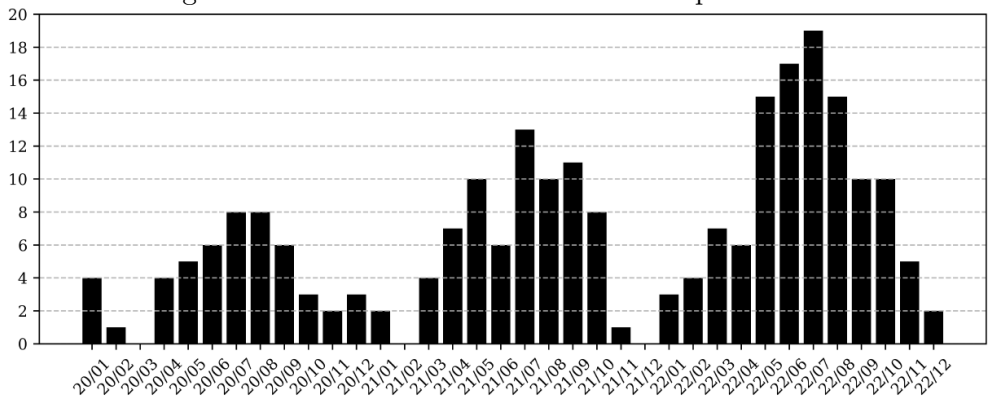

5.1.1 Misalignment between WFI inter-satellites

Table 5.1 presents basic statistics (minimum, maximum, standard deviation and mean) after performing co-registration of CBERS-4A and CBERS-4 as target images and AMAZONIA-1 as reference. Figure 5.4 shows a bar plot that contains, for each path/row, a comparison between the minimum, maximum, standard deviation and mean values of the pixels displacements.

Table 5.1 - Basic statistics for pixel displacements after co-registration.

Path / Row	Minimum	Maximum	Standard deviation	Mean
132 - 203	0.45	2.02	0.33	0.97
132 - 204	0.58	2.06	0.28	0.95
132 - 205	0.41	1.84	0.37	0.95
132 - 206	0.51	2.67	0.49	1.19
132 - 207	0.34	2.08	0.44	1.09
132 - 208	0.95	2.6	0.22	1.64
132 - 209	0.62	1.88	0.21	1.01
132 - 210	0.25	2.36	0.39	1.29
117 - 154	0.56	1.43	0.07	0.78
117 - 155	0.71	1.38	0.07	0.85
117 - 156	0.53	0.91	0.06	0.69
117 - 157	0.79	1.35	0.17	1.06
117 - 158	0.69	1.17	0.04	0.81
117 - 159	0.74	1.49	0.08	1.36
117 - 160	0.44	1.46	0.26	0.94
117 - 161	1.42	2.36	0.16	1.77

Figure 5.4 - Bar plot of the basic statistics of the spatial shifts after co-registration.

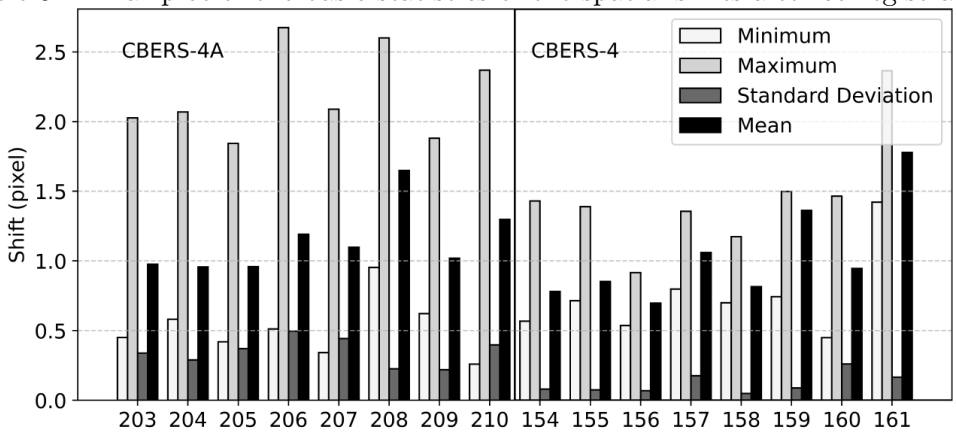

Both Table 5.1 and Figure 5.4 illustrate a noticeable spatial disagreement between images from CBERS-4A and AMAZONIA-1 when compared to the CBERS-4 and AMAZONIA-1. The higher disparity reached a maximum shift of 2.67 pixels. It's worth noting that, with the exception of CBERS-4A rows 203, 204, and 205, all other rows exhibited an average shift exceeding one pixel. As for the co-registration of CBERS-4 images, only rows 157, 159, and 161 displayed average shifts greater than one pixel.

5.2 Fire in the Chapada dos Veadeiros National Park from 2020 to 2022

Figure 5.5 shows the mapping for the three years generated by image interpretation.

Figure 5.5 - Annual burned areas mapped by visual image analysis.

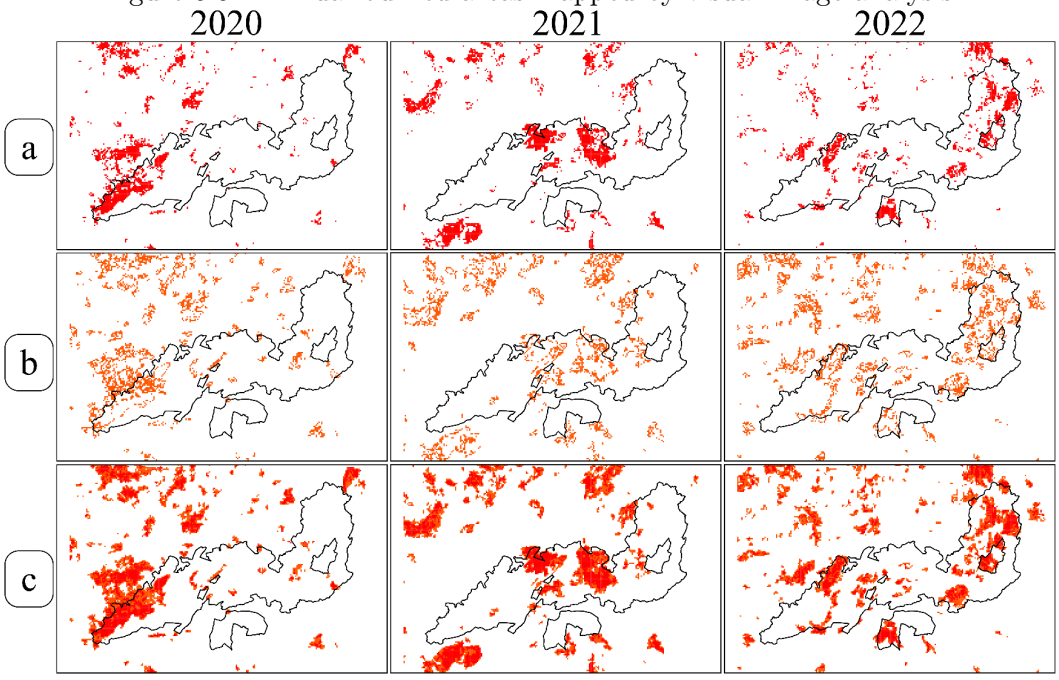

a: only TB cells; b: only PB cells; c: TB plus PB cells.

Despite the existence of TB cells and PB cells to denote areas affected by fire, it is important to emphasize that these two labels represent the BA class, while the label NB designates the unburned class, as mentioned before. Figure 5.6a shows the monthly distribution of burned areas considering the number of cells mapped as TB, Figure 5.6b contains the same analysis considering only the number of PB cells and Figure 5.6c shows the sum of TB cells and PB cells.

Figure 5.6 - Monthly distribution of cells with burned areas throughout the time series.

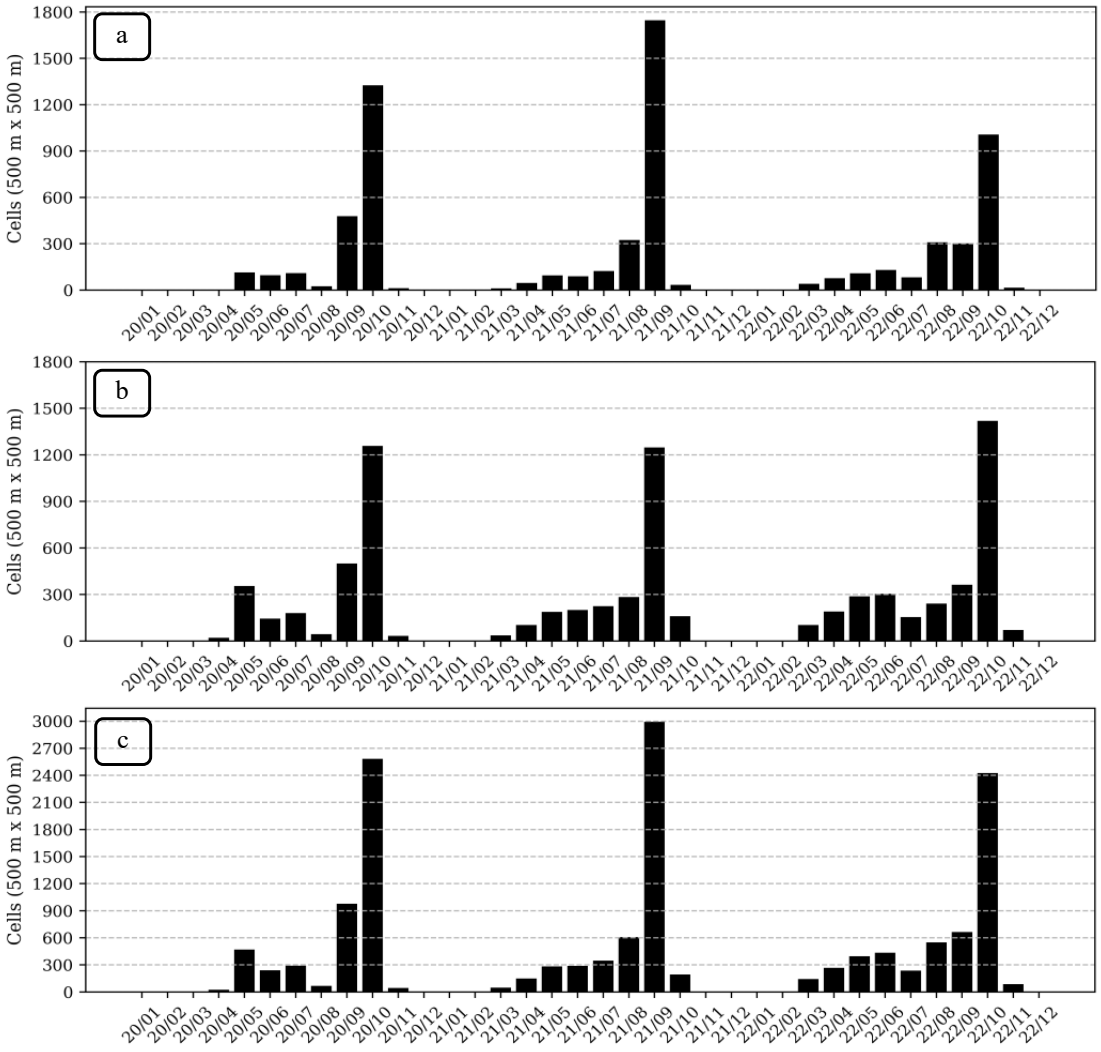

a: monthly TB cells; b: monthly PB cells; c: monthly TB and PB cells

.

Figure 5.6c illustrates that the monthly fire peak in 2020 occurred in October, when more than 2,500 cells (625 km²) were totally or partially affected by fire. In 2021, the month with the highest number of these cells was September, and it was also the month with the highest number of burned cells among the three years, with nearly 3,000 burned cells (750 km²). Similarly to 2020, in 2022 the fire peak was

recorded in October, with around 2,400 burned (650 km^2). Overall, it can be seen that the other burning events are mainly distributed between the months of April and August, and that the period between November and March is the period with the lowest number of burned cells, as shown by Figure 5.7.

Figure 5.7 - Analyzing the burned areas time series with monthly temporal decomposition.

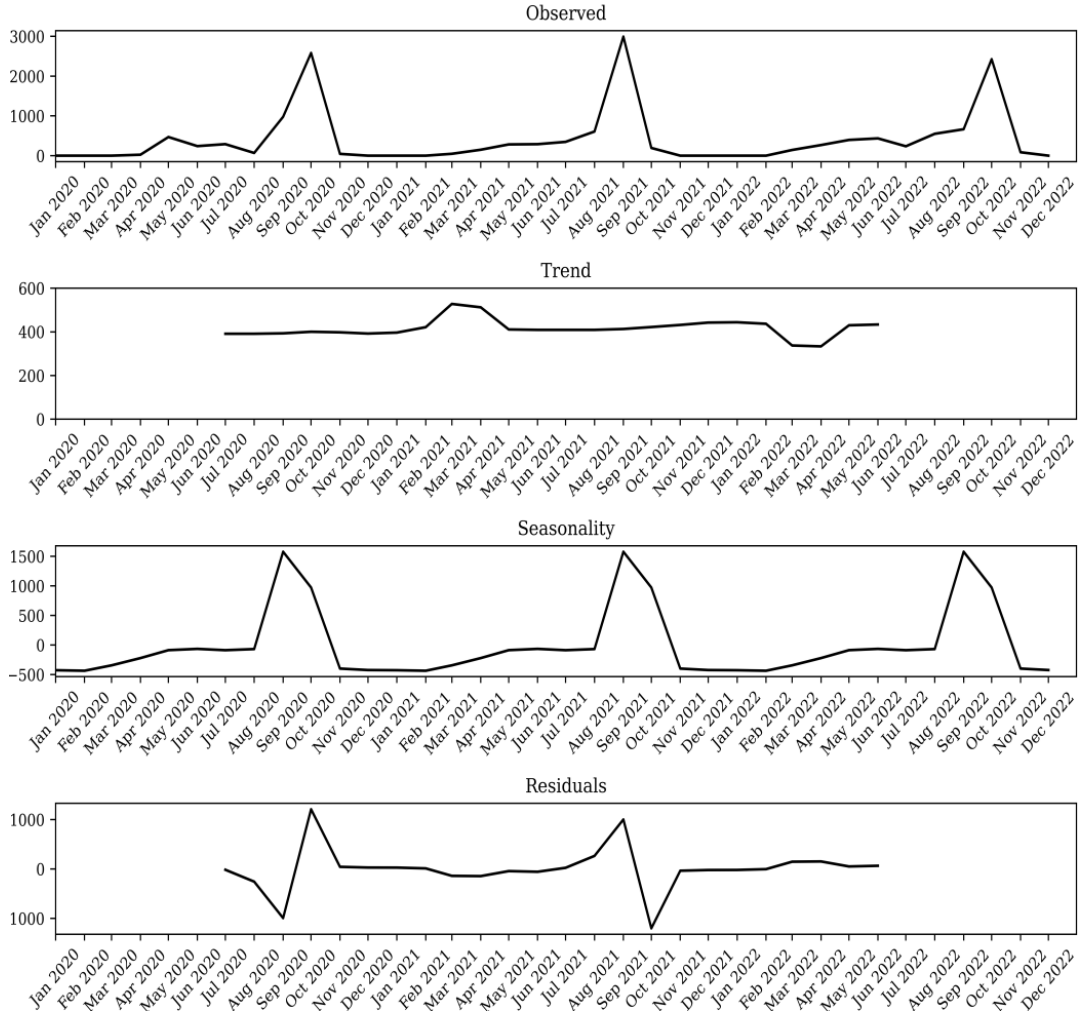

The decomposition of this monthly time series allows us to observe the typical behavior of the fire regime in the Brazilian Cerrado, characterized by high occurrence and spread during dry months (May to September), mainly during winter season (June to September) and its transition to spring, which in the Cerrado occurs in October, according to Mataveli et al. (2018). The trend plot shows disturbances in the trend of the series between January and April for the years 2021 and 2022, due to the higher incidence of fires during this period in 2021 compared to 2020, and a lower incidence in 2022 compared to 2021.

From February to April there is a constant increase in the number of burned cells,

followed by a stabilization between April and July. The seasonality plot shows that the fire regime in the three years starts around July, so the critical period is concentrated between July and October. An analysis of the residuals plot suggests that, even during this critical fire period, the inter-annual behavior does not exhibit complete similarity, as there are annual prediction errors attributed to variations in the observed number of burned cells in those months. Despite being the period with the highest number of burned cells, these months do not exhibit identical patterns.

5.3 Classifications

We trained and evaluated the models using both the TB cells and the concatenation of TB and PB cells for different models generation. The objective was to determine whether classifications using only TB cells would produce better results than using TB plus PB cells, despite the fact that concatenating these labels makes it possible to increase the number of samples. The intention was to verify if partially burned cells are less predictable, due to the greater spectral mixing of targets within them. We initially explored annual and semi-annual approaches with annual ARD datasets.

5.3.1 ARD datasets

5.3.1.1 Annual datasets

Figure 5.8 shows the F1-score obtained from the 30% of the validation samples considering the annual datasets labeled with the binary classes of burned area (TB cells) and unburned area (not even partially burned cells). We note by analyzing the three years that 2021 was the year that returned the highest scores, followed by 2020 and 2022. Although the years 2020 and 2022 have almost the same sample size of burned cells, the datasets showed slightly different responses. For all years the training returned F1-scores equal or superior to 0.9. These results are the average of the five classifications carried out per dataset, as explained before.

Figure 5.8 - F1-score for annual classifications using TB cells as the BA class.

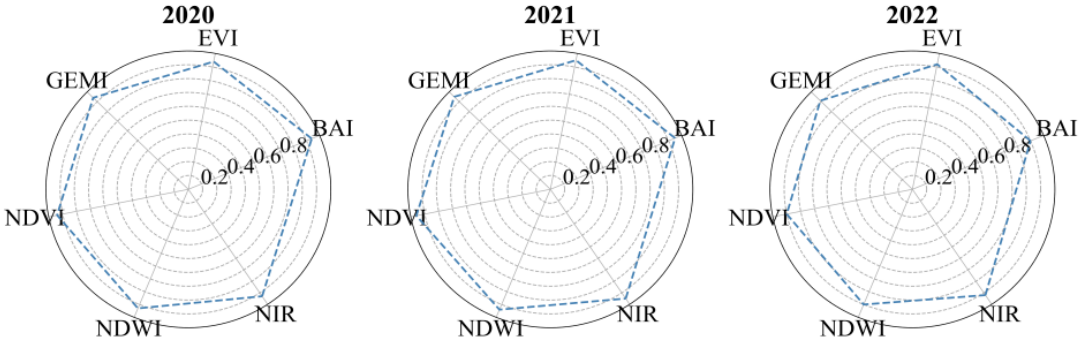

Samples per class: 2020 (1,291); 2021 (1,481); 2022 (1,250).

In 2020, the most accurate training datasets, GEMI, EVI, BAI, and NIR, achieved an F1-score of 0.94. Additionally, NDWI and NDVI produced similar results, both scoring 0.93, indicating minimal differences between them. This year had the fewest valid observations (55 images). Although data replication resulted in extended intervals of repeated values, the training successfully distinguished burned areas from different moments of the year. This result suggests the potential for detecting fire-affected areas based on annual time series, even in years with fewer available images.

In 2021, with 72 valid observations including AMAZONIA-1 WFI images since March 2021, we observed the most similar responses compared to 2020. This indicates that the indices perform similarly and proportionally to those in 2020. All datasets achieved higher F1 values in 2021 in comparison with other years, mainly in relation to 2022. The GEMI dataset recorded the highest F1-score at 0.96, while NDVI had the lowest at 0.94. Nevertheless, the analyses do not yet allow us to conclude which datasets perform better than others, and this will be explored further.

The most important difference was observed in 2022. Despite having 113 images, making it the most regular time series, due to the inclusion of CBERS-4 images in the INPE catalog since May 2022, it was observed that the BAI and NDWI datasets achieved the highest F1-score at 0.92, while the NIR, GEMI, and NDVI datasets obtained the lowest scores, which were lower than those in previous years. However, all the results achieved F1 values equal to 90% or higher, which also does not allow us to highlight significant differences between years.

Figure 5.9 shows the results obtained using TB and PB cells as samples of BA class. Comparing the plots with those in Figure 5.8, we note lower F1-scores in all years. Despite this, the year 2021 still produced the highest scores, followed by 2020 and 2022. Table 5.2 analysis indicates that reduced precision in classifying NB areas is responsible for the inferior performance when we use TB and PB cells concatenated.

Figure 5.9 - F1-score for annual classifications using TB plus PB cells as the BA class.

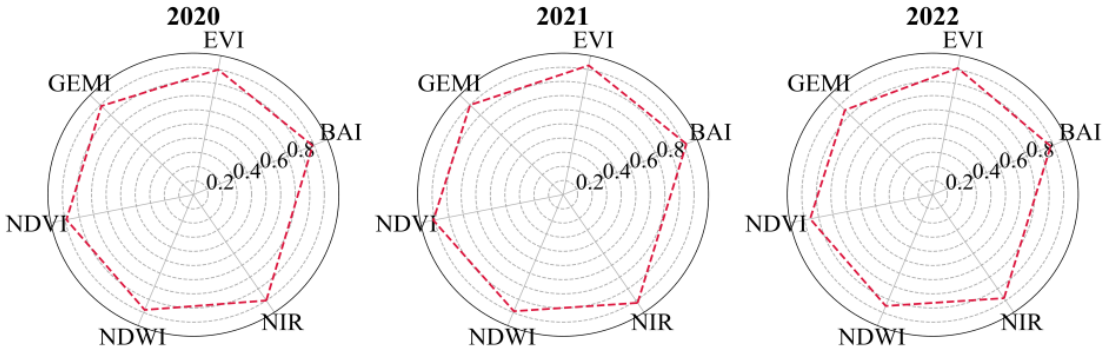

Samples per class: 2020 (2,790); 2021 (2,943); 2022 (3,137).

When PB are used with TB cells we can see that, in general, and regardless of the year (Table 5.2), the BAI, NDWI, and NIR, tend to yield the highest F1-scores. Among GEMI, EVI and NDVI, GEMI is the index with the best performance to classify burned areas and NDVI is the least efficient. These three vegetation indices seem to be influenced by other spectral components within the cells. Figure 5.10 shows the comparison between the models generated with datasets labeled with TB and with TB plus PB cells and Table 5.2 summarizes all the results of F1-score, precision, and recall for both classes.

Figure 5.10 - Comparison of F1-score from annual classifications using only TB cells and using TB plus PB cells as the BA class.

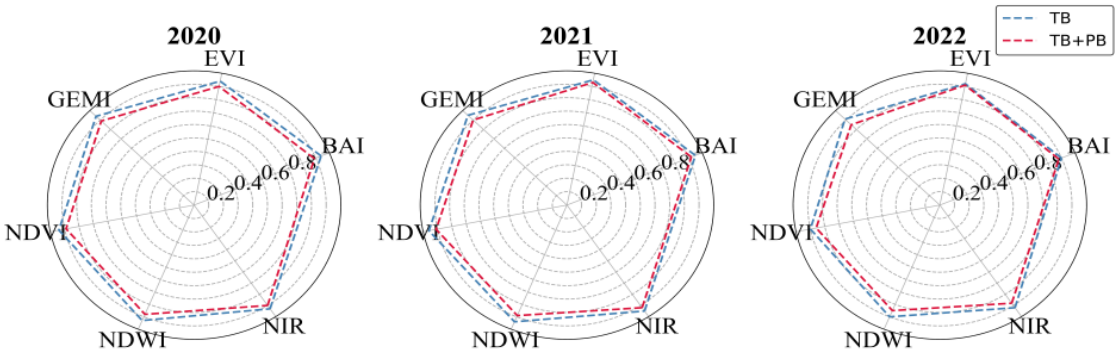

Table 5.2 - Summary of validation results (precision, recall and F1-score) per year considering TB cells and TB plus PB cells as input samples of the BA class.

	Precision		Recall		F1-	Precision		Recall		F1-
	BA	NB	BA	NB	score	BA*	NB	BA*	NB	score
NIR (2020)	0.95	0.93	0.93	0.94	0.94	0.95	0.85	0.83	0.96	0.89
NIR (2021)	0.94	0.96	0.96	0.94	0.95	0.96	0.9	0.89	0.96	0.92
NIR (2022)	0.89	0.93	0.92	0.89	0.9	0.89	0.88	0.88	0.89	0.88
BAI (2020)	0.95	0.94	0.94	0.95	0.94	0.95	0.86	0.85	0.96	0.9
BAI (2021)	0.94	0.96	0.96	0.93	0.95	0.95	0.9	0.9	0.95	0.93
BAI (2022)	0.9	0.93	0.93	0.9	0.92	0.91	0.89	0.89	0.91	0.91
EVI (2020)	0.96	0.92	0.92	0.96	0.94	0.96	0.83	0.8	0.97	0.89
EVI (2021)	0.96	0.94	0.94	0.96	0.95	0.96	0.85	0.83	0.97	0.9
EVI (2022)	0.9	0.92	0.92	0.9	0.91	0.85	0.85	0.85	0.85	0.85
GEMI (2020)	0.96	0.93	0.92	0.96	0.94	0.96	0.84	0.82	0.97	0.89
GEMI (2021)	0.96	0.96	0.96	0.96	0.96	0.96	0.86	0.84	0.97	0.91
GEMI (2022)	0.89	0.94	0.94	0.88	0.9	0.87	0.85	0.85	0.88	0.86
NDVI (2020)	0.94	0.92	0.92	0.94	0.93	0.94	0.84	0.82	0.94	0.88
NDVI (2021)	0.95	0.93	0.93	0.95	0.94	0.93	0.86	0.85	0.94	0.89
NDVI (2022)	0.87	0.92	0.93	0.86	0.9	0.83	0.87	0.88	0.82	0.85
NDWI (2020)	0.94	0.93	0.93	0.94	0.93	0.94	0.86	0.85	0.95	0.9
NDWI (2021)	0.96	0.95	0.95	0.96	0.95	0.96	0.89	0.87	0.96	0.92
NDWI (2022)	0.9	0.93	0.94	0.89	0.92	0.89	0.87	0.87	0.89	0.88

BA: TB; NB: unburned; BA*: TB + PB.

5.3.1.2 Semi-annual datasets

Figure 5.11 presents radar plots comparing the models generated using semi-annual datasets (182 observations in each dataset). The primary aspect to note is the difference in the number of samples available per semester. During the January to June period, the southern hemisphere experiences summer and autumn seasons and this period marks the transition from a climate characterized by warm temperatures and increased precipitation to a colder climate with reduced precipitation. In the Brazilian Cerrado, fires are expected to be most widespread and persistent during the second semester due to the dry peak and favorable vegetation conditions for burning, as shown in Figure 5.11.

Figure 5.11 - F1-score for semi-annual classifications using TB cells as the BA class.

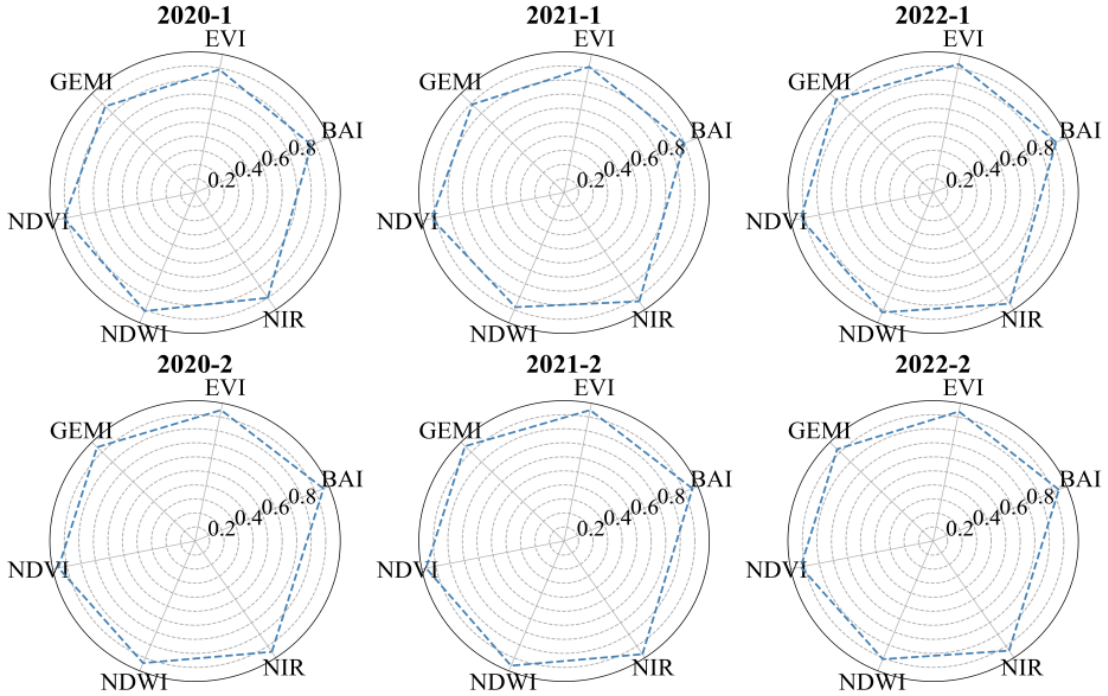

Samples per class: 2020-1 (125); 2020-2 (1,166); 2020-1 (158); 2021-2 (1,323); 2022-1 (217); 2022-2 (1,033).

The seasonal fire behavior needs to be considered in the development of semi-annual machine learning models. It poses a challenge in predicting scenarios and distinguishing between classes due to the limited number of samples available during the first semester of a year. Figure 5.11 allows us to visualize that the plots related to the first semester exhibited lower F1 values, with the exception of 2022-1, that has more samples available for this period. Upon examining the results, we can observe that GEMI had the best performance in 2020-1 (0.92) and 2021-1 (0.93). NDWI achieved

the same F1-score as GEMI in 2021-1 and showed the best result in 2022-1 (0.95).

When focusing on the second semester, we observe higher F1-scores, with all training datasets achieving scores equal or higher to 0.91. The performance of the indices, particularly in 2020-2 and 2021-2, demonstrates similarities, indicating that these indices produce comparable results. Overall, all indices returned higher F1-scores in 2021-2 compared to other semesters, and the maximum F1-score for this period was achieved by the GEMI and NDWI datasets (0.97). For the period of 2022-2, our results indicate that the highest F1-scores were achieved by the BAI, NDWI, and NIR datasets (0.94), and that the NDVI yielded the lowest F1-score (0.91).

Figure 5.12 illustrates the results when we combine TB and PB cells as samples of the BA class. Comparing it with Figure 5.13, we can see that, similarly to the annual datasets, combining both labels tends to reduce the performance of the classifier. We may observe the impact of sample size on the classifier's performance analyzing 2022-1, which has the highest number of samples among the first semester and the highest F1-scores for the period. The BAI obtained the highest accuracy (0.94) in 2022-1, considering all datasets from the first semesters.

Figure 5.12 - F1-score for semi-annual classifications using TB plus PB cells as the BA class.

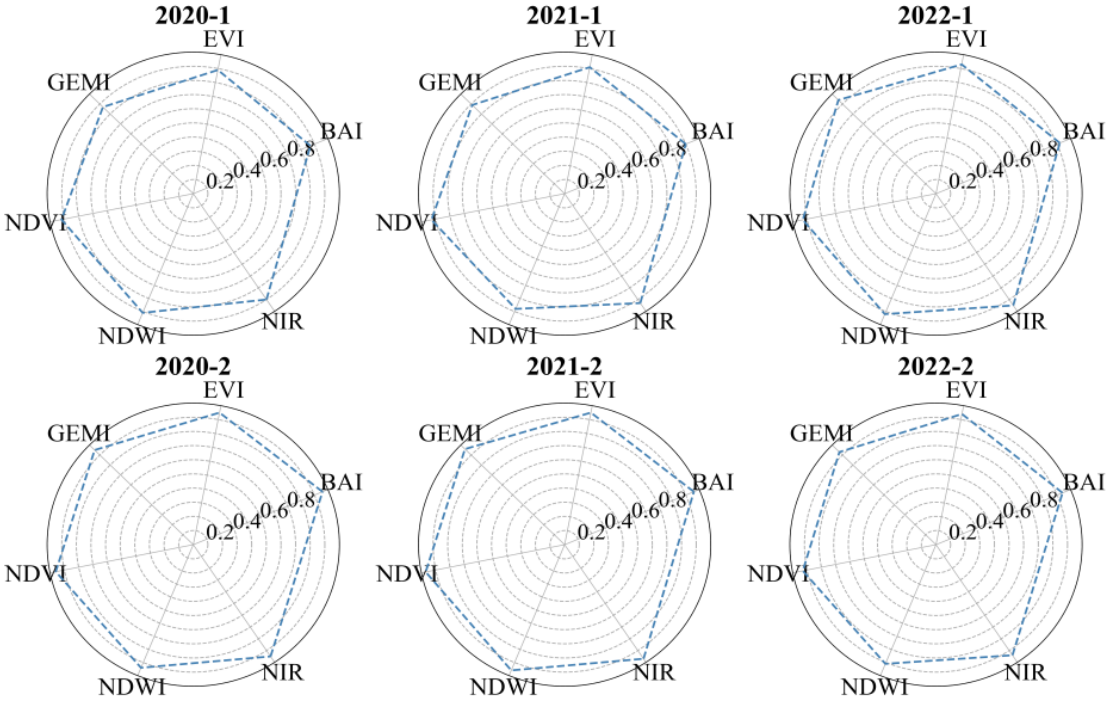

Samples per class: 2020-1 (432); 2020-2 (2,359); 2020-1 (497); 2021-2 (2,447); 2022-1 (756); 2022-2 (2,385).

Figure 5.13 shows the overlap of the plots with only TB cells and TB with PB cells as input samples for the BA class. In 2022-1, BAI performed slightly better (0.89) when using TB plus PB cells as input samples compared to using only TB cells (0.86). This may occur due to a lower sensitivity of the BAI to be mixed with different terrestrial targets within the cells, once it is based on the Euclidean distance of the red and near infrared bands, and not on normalized differences used to highlight specific targets as vegetation and water bodies, targets commonly confused to burned areas.

Figure 5.13 - Comparison of F1-score from semi-annual classifications using only TB cells and using TB plus PB cells as the BA class.

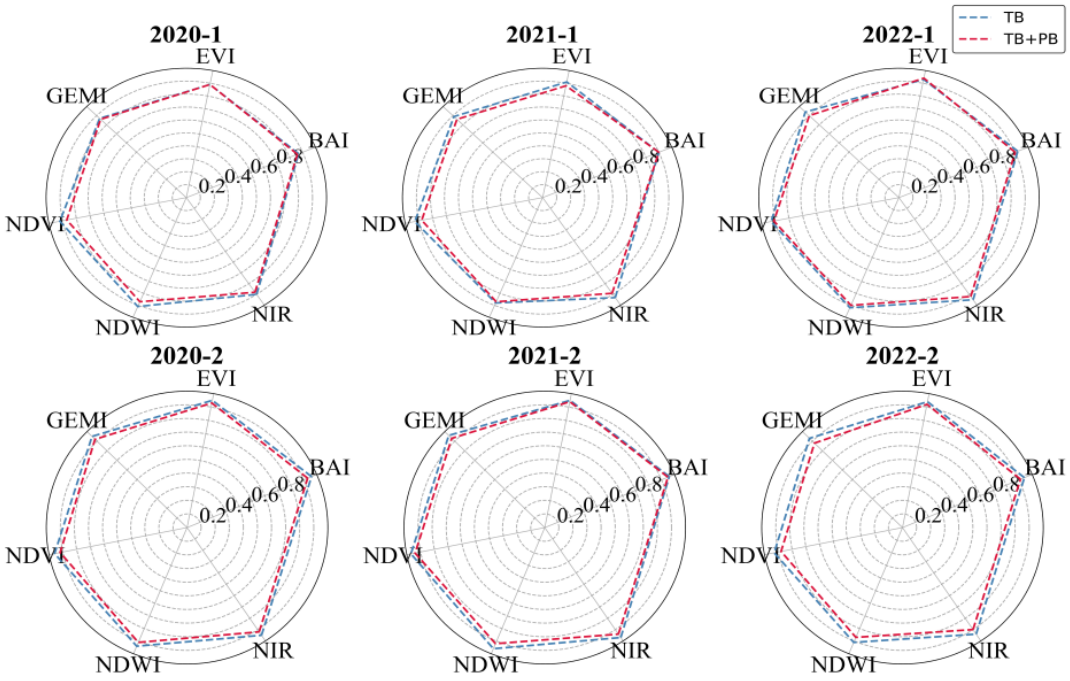

We observed that, regardless of the set of input samples and the semester, the shapes of the plots are similar, despite the reduction in F1-scores when the TB and PB cells are combined. It leads to a decrease in the performance of classifications without significant changes in the response of different spectral indices or the NIR band. Table 5.3 summarizes the results of the classification for the datasets from the first semester, and Table 5.4 contains the results of the training performed on the datasets from the second semester. We note a decrease in the recall of the NB class when combining TB and PB.

Due to the heterogeneity and spectral mixing within the regular cells, predicting partially burned cells would be a challenge because of noises in the burned area responses. Alternatively, using only TB cells may limit the classifier to detect homogeneous targets, potentially leading to underestimation of burned areas, as partially

burned cells may not be classified. Further testing and analysis will explore this.

Table 5.3 - Summary of validation results (precision, recall and F1-score) according to the first semester considering TB cells and TB plus PB cells as input samples of the BA class.

	Precision		Recall		F1-	Precision		Recall		F1-
	BA	NB	BA	NB	score	BA*	NB	BA*	NB	score
NIR (20-1)	0.84	0.9	0.91	0.83	0.87	0.83	0.89	0.89	0.83	0.86
NIR (21-1)	0.89	0.9	0.91	0.88	0.9	0.89	0.91	0.92	0.88	0.9
NIR (22-1)	0.9	0.95	0.95	0.89	0.92	0.88	0.93	0.94	0.87	0.9
BAI (20-1)	0.88	0.91	0.92	0.87	0.89	0.85	0.93	0.94	0.84	0.89
BAI (21-1)	0.88	0.94	0.95	0.86	0.91	0.86	0.91	0.92	0.85	0.88
BAI (22-1)	0.89	0.97	0.97	0.89	0.93	0.93	0.94	0.94	0.93	0.94
EVI (20-1)	0.86	0.89	0.89	0.85	0.87	0.83	0.89	0.89	0.83	0.86
EVI (21-1)	0.84	0.95	0.95	0.84	0.89	0.83	0.89	0.89	0.83	0.86
EVI (22-1)	0.92	0.95	0.95	0.92	0.94	0.9	0.9	0.9	0.9	0.9
GEMI (20-1)	0.93	0.91	0.91	0.92	0.92	0.84	0.9	0.9	0.84	0.87
GEMI (21-1)	0.92	0.94	0.95	0.91	0.93	0.87	0.89	0.89	0.87	0.88
GEMI (22-1)	0.91	0.96	0.95	0.91	0.93	0.9	0.92	0.92	0.9	0.91
NDVI (20-1)	0.88	0.93	0.94	0.88	0.91	0.83	0.92	0.92	0.82	0.87
NDVI (21-1)	0.87	0.91	0.91	0.85	0.88	0.86	0.87	0.87	0.86	0.87
NDVI (22-1)	0.9	0.94	0.94	0.89	0.92	0.89	0.91	0.91	0.89	0.9
NDWI (20-1)	0.9	0.9	0.89	0.89	0.9	0.85	0.91	0.92	0.84	0.88
NDWI (21-1)	0.93	0.94	0.95	0.93	0.93	0.88	0.9	0.89	0.88	0.89
NDWI (22-1)	0.95	0.95	0.95	0.95	0.95	0.92	0.91	0.91	0.93	0.92

BA: TB; NB: unburned; BA*: TB + PB.

Table 5.4 - Summary of validation results (precision, recall and F1-score) according to the second semester considering TB cells and TB plus PB cells as input samples of the BA class.

	Precision		Recall		F1-	Precision		Recall		F1-
	BA	NB	BA	NB	score	BA*	NB	BA*	NB	score
NIR (20-2)	0.96	0.95	0.96	0.96	0.96	0.97	0.9	0.89	0.97	0.93
NIR (21-2)	0.95	0.98	0.98	0.95	0.96	0.97	0.93	0.93	0.97	0.95
NIR (22-2)	0.94	0.95	0.95	0.94	0.94	0.94	0.88	0.88	0.94	0.91
BAI (20-2)	0.95	0.95	0.95	0.95	0.95	0.96	0.9	0.9	0.96	0.93
BAI (21-2)	0.95	0.97	0.97	0.95	0.95	0.98	0.92	0.92	0.98	0.94
BAI (22-2)	0.92	0.95	0.95	0.92	0.94	0.93	0.9	0.9	0.94	0.92
EVI (20-2)	0.95	0.96	0.95	0.95	0.95	0.97	0.88	0.86	0.98	0.92
EVI (21-2)	0.96	0.97	0.97	0.96	0.96	0.97	0.89	0.88	0.97	0.93
EVI (22-2)	0.94	0.92	0.93	0.94	0.93	0.9	0.85	0.84	0.91	0.88
GEMI (20-2)	0.96	0.97	0.97	0.96	0.96	0.96	0.89	0.88	0.97	0.92
GEMI (21-2)	0.97	0.97	0.97	0.97	0.97	0.98	0.91	0.9	0.98	0.94
GEMI (22-2)	0.92	0.94	0.94	0.92	0.93	0.9	0.86	0.85	0.91	0.88
NDVI (20-2)	0.95	0.93	0.93	0.95	0.94	0.96	0.87	0.85	0.97	0.91
NDVI (21-2)	0.95	0.96	0.96	0.96	0.96	0.96	0.89	0.88	0.96	0.92
NDVI (22-2)	0.9	0.92	0.92	0.9	0.91	0.88	0.87	0.86	0.88	0.87
NDWI (20-2)	0.95	0.94	0.95	0.95	0.95	0.95	0.89	0.88	0.96	0.92
NDWI (21-2)	0.96	0.97	0.97	0.96	0.97	0.98	0.91	0.91	0.98	0.94
NDWI (22-2)	0.92	0.95	0.95	0.92	0.94	0.91	0.9	0.9	0.91	0.9

BA: TB; NB: unburned; BA*: TB + PB.

5.3.2 Multitemporal datasets

5.3.2.1 Labeled with totally burned cells

Figure 5.14 and Table 5.5 shows the F1-score results for the models generated with the multitemporal datasets that contains samples from all yers and the precision and recall for both classes. Analyzing the F1-score metric, we can see that NDWI returned the highest result (0.92), while NIR, BAI, EVI and GEMI returned the same accuracy of the classifier (0.91). We can see by comparing the precision from both classes that NB is slightly better distinguishable from BA. While BA is more proficient at making accurate classifications, the lower recall of NB shows that more unburned cells are being identified as burned than the opposite. NDVI was the dataset with the lowest F1-score (0.89).

Figure 5.14 - Validation metrics (F1-score, precision and recall) for multitemporal classifications using TB cells as the BA class.

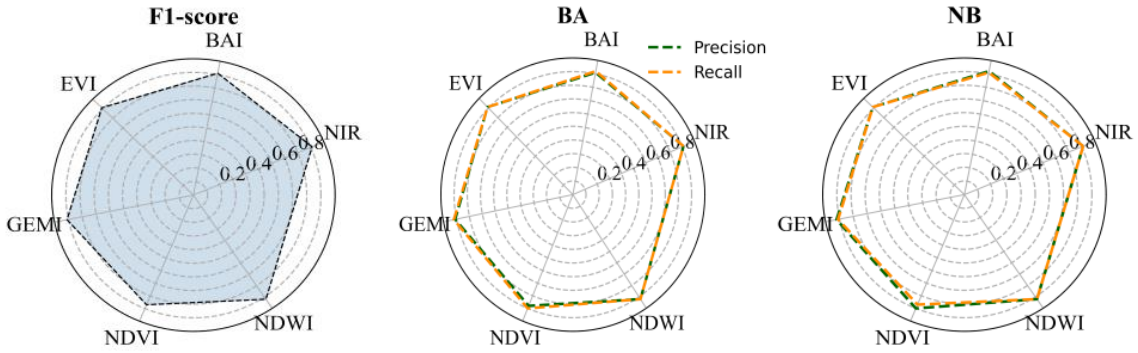

BA: burned area class; NB: unburned area class. Samples per class: 2,814.

Table 5.5 - Summary of validation results (precision, recall and F1-score) per multitemporal dataset considering TB cells as input samples of the BA class.

	Precision		Recall		F1-score
	BA	NB	BA	NB	
NIR	0.91	0.91	0.91	0.91	0.91
BAI	0.91	0.92	0.92	0.91	0.91
EVI	0.91	0.91	0.91	0.91	0.91
GEMI	0.91	0.92	0.92	0.91	0.91
NDVI	0.88	0.9	0.9	0.87	0.89
NDWI	0.92	0.92	0.92	0.92	0.92

After training the multitemporal datasets, we generalized the obtained models to the annual ARD datasets. We used the Intersection over Union (IoU) metric to evaluate these results, considering two mappings as references: the manual mapping

that contains all the TB cells and the mapping that contains the concatenation of the TB with PB cells (Figure 5.5a and Figure 5.5c). Figure 5.15 shows the results for the three years considering all datasets. An important result is that considering the reference mapping with TB and PB cells leads to better results of IoU.

Even though the models were initially trained only with TB cells, the generalizations were able to also identify cells that were partially affected by fire. We see that the lowest IoU results are associated with the NDVI annual datasets. Additionally, when considering the years, 2021, which achieved the highest F1-scores in the annual time series analysis, also yielded the best IoU values, reaching 72% (0.72) compared to the reference mapping with TB and PB cells when we consider the NIR, EVI, GEMI and NDWI datasets. Similarly, we found that 2022 produced the lowest IoU results.

Figure 5.15 - IoU obtained by the generalized annual datasets labeled with TB cells as the BA class based on the multitemporal models.

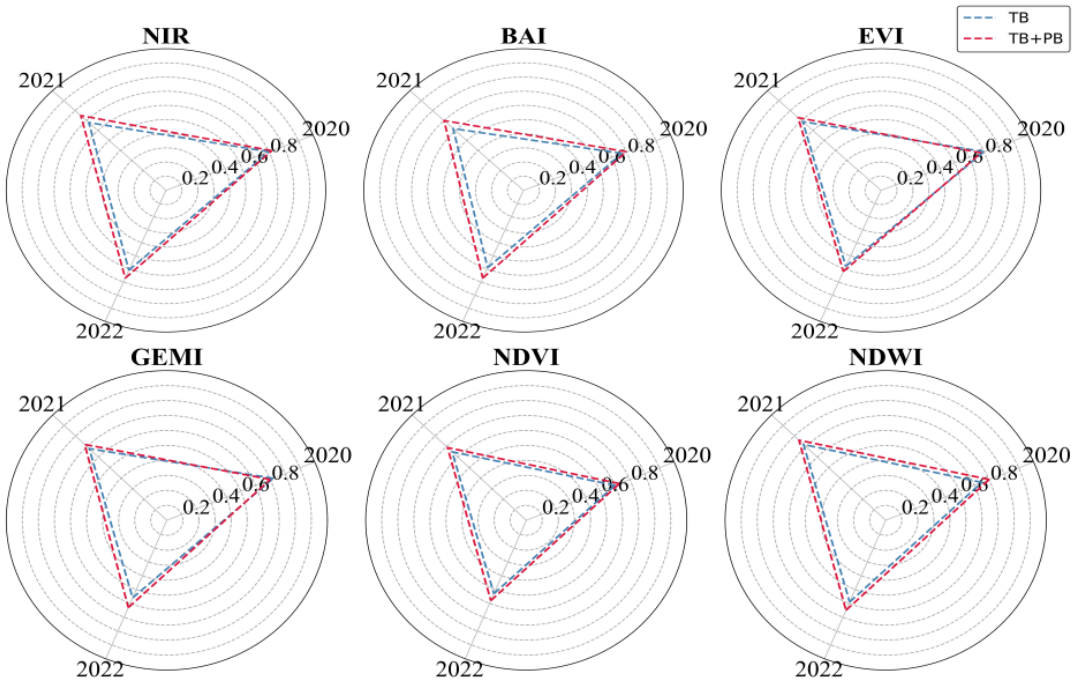

TB: reference mapping with TB cells as the BA class; TB+PB: reference mapping with TB plus PB cells as the BA class.

Previous results indicate that the annual datasets from 2022 returned the lowest IoU in both training and testing compared to other years. Aiming to understand the underlying factors related to the reduced classification and generalization performances in 2022 we highlight the necessity of a more robust time series that includes images from CBERS-4 since 2020. Although this satellite was launched in 2014, INPE has not yet included its historical images in the catalog used in this study.

Table 5.6 provides a summary of the IoU results. It is interesting to highlight the performance of EVI and GEMI in 2020, as they were the only cases where the comparison with the mapping of TB cells as BA class yielded better results than the concatenation of TB with PB.

Table 5.6 - Summary of IoU results obtained by the generalized annual datasets created with TB cells as samples of the BA class based on the multitemporal models.

	IoU	
	TB	**TB + PB**
NIR (2020)	0.7	0.72
NIR (2021)	0.68	0.75
NIR (2022)	0.61	0.67
BAI (2020)	0.67	0.7
BAI (2021)	0.62	0.7
BAI (2022)	0.59	0.67
EVI (2020)	0.7	0.68
EVI (2021)	0.69	0.73
EVI (2022)	0.58	0.62
GEMI (2020)	0.72	0.7
GEMI (2021)	0.68	0.72
GEMI (2022)	0.56	0.63
NDVI (2020)	0.6	0.63
NDVI (2021)	0.65	0.69
NDVI (2022)	0.53	0.58
NDWI (2020)	0.65	0.7
NDWI (2021)	0.72	0.76
NDWI (2022)	0.59	0.65

Adopting regular grids enables the integration of data with different characteristics and reduces the amount of data, but limits the scale and precision of the mapping to the dimensions of the spatial cells. In the case of burned areas and binary classifications, although the training of the annual models returns higher classifier accuracies when the input is made with TB cells instead TB plus PB cells, the generalization, on the other hand, returns higher IoU values when we use the reference mapping that has TB plus PB burned cells. This indicates the detection of cells partially affected by fire when the input consists only of homogeneous cells.

Figure 5.16 shows the generalization results based on the models created with multitemporal datasets labeled only with TB cells. We can note, comparing the classifications with Figure 5.5, the presence of false positives from the BA class, specially in the year 2022, potentially indicating confusion between burned areas and patches of Cerrado's phytophysiognomies, or false positives detected due to the behavior of samples from other years. Figure 5.17 elucidates one of the best generalizations by comparing it with the reference mapping containing TB plus PB cells.

Figure 5.16 - Annual burned areas classified with models from annual multitemporal datasets labeled with TB cells as samples of BA.

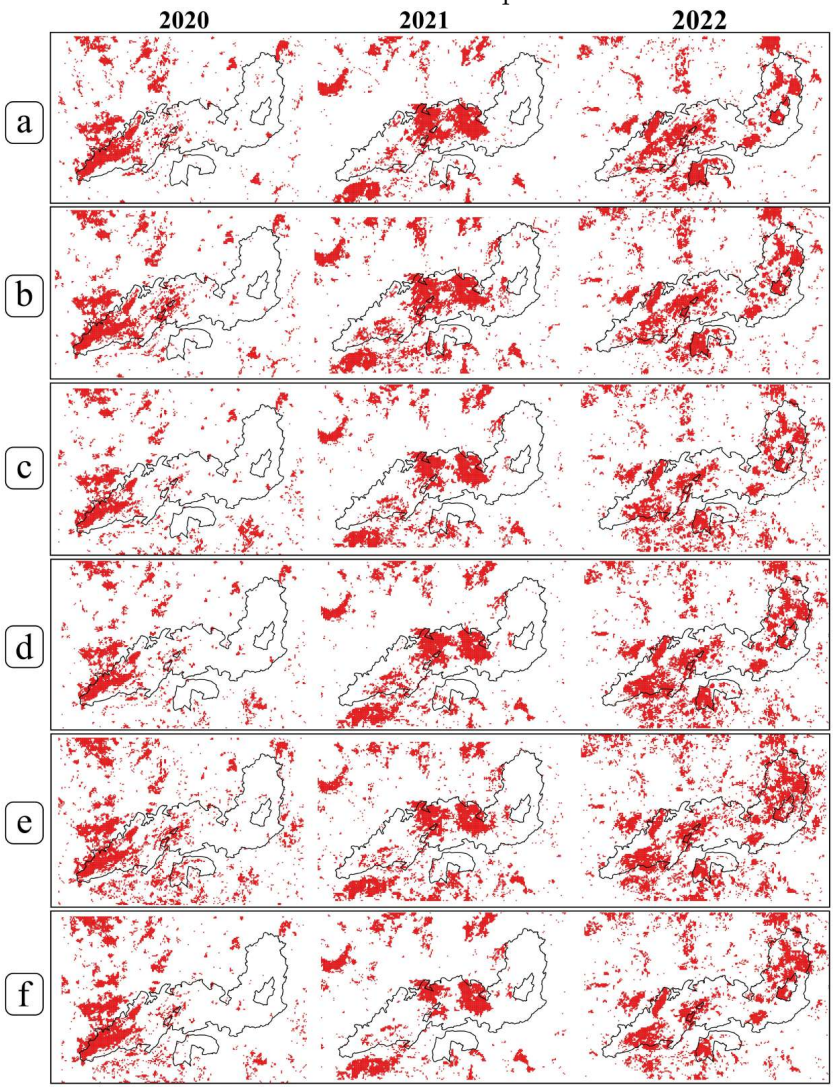

a: NIR; b: BAI; c: EVI; d: GEMI; e: NDVI; f: NDWI.

Figure 5.17 - Example of a generalization (NIR 2021, IoU = 75%).

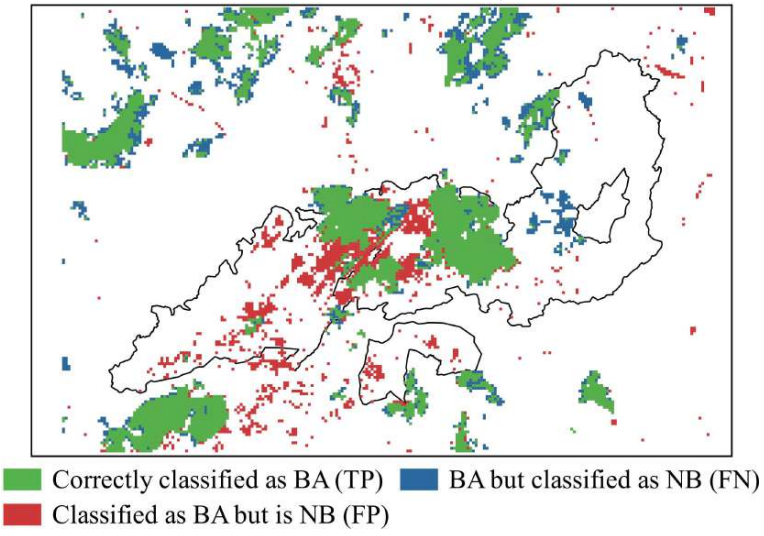

TP: true positive; FP: false positive; FN: false negative.

5.3.2.2 Labeled with totally and partially burned cells

Figure 5.18 and Table 5.7 contain the results for the F1-score, precision, and recall metrics obtained after classifying these datasets. In terms of number of samples, we see that the datasets labeled with PB cells have more than twice (6,209 samples per binary class) as many samples available as the datasets labeled only with cells totally affected by fire (2,814 samples per binary class). All datasets returned lower F1-scores when compared to the models created using only TB cells, and the best results were obtained by the NDWI (0.87), NIR and BAI (0.86) multitemporal datasets.

Figure 5.18 - Summary of validation results (F1-score, precision and recall) per multitemporal dataset considering TB plus PB cells as input samples of the BA class.

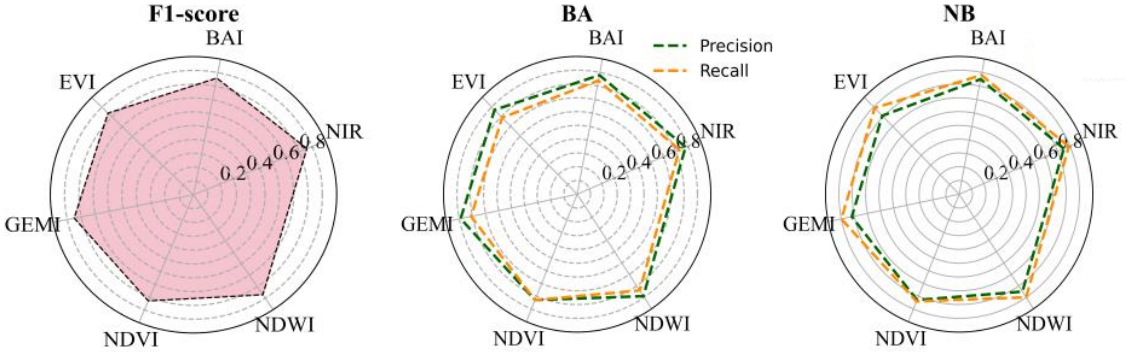

Samples per class: 6,209.

Table 5.7 - Summary of validation results (precision, recall and F1-score) per multitemporal dataset considering TB plus PB cells as input samples of the BA class.

	Precision		Recall		F1-score
	BA	NB	BA	NB	
NIR	0.88	0.85	0.83	0.89	0.86
BAI	0.88	0.85	0.84	0.88	0.86
EVI	0.87	0.81	0.79	0.89	0.84
GEMI	0.89	0.82	0.81	0.9	0.85
NDVI	0.83	0.83	0.83	0.84	0.83
NDWI	0.89	0.85	0.84	0.9	0.87

Contrary to what was observed in the analysis of the datasets labeled with TB cells, we had lower precision and recall results for both classes. Also there is an inversion between the performance of these binary classes. While the classifier exhibits higher precision in correctly classifying samples from the BA class in all multitemporal datasets, we observe that the NB class, despite lower precision, can better generalize the results to unseen data, comprising cells not included in the training of the multitemporal models. It indicates a propensity for misclassifying cells as BA (false positive) rather than as NB (false negative).

Figure 5.19 presents the IoU results after generalizing the datasets labeled with TB and PB cells. The best results were obtained in the year 2021, with NDWI (0.76), NIR (0.75), GEMI (0.72), and EVI (0.71) achieving more than 70% correspondence with the reference mapping that combines both types of burned cells into the BA class. Once again, the IoU results are higher when this mapping is used as the reference for validation. The NDVI annual datasets yielded the lowest results. In line with previous analyses, 2022 stands out as the year with the weakest generalization performances.

Figure 5.19 - IoU obtained by the generalized annual datasets labeled with TB plus PB cells as the BA class based on the multitemporal models.

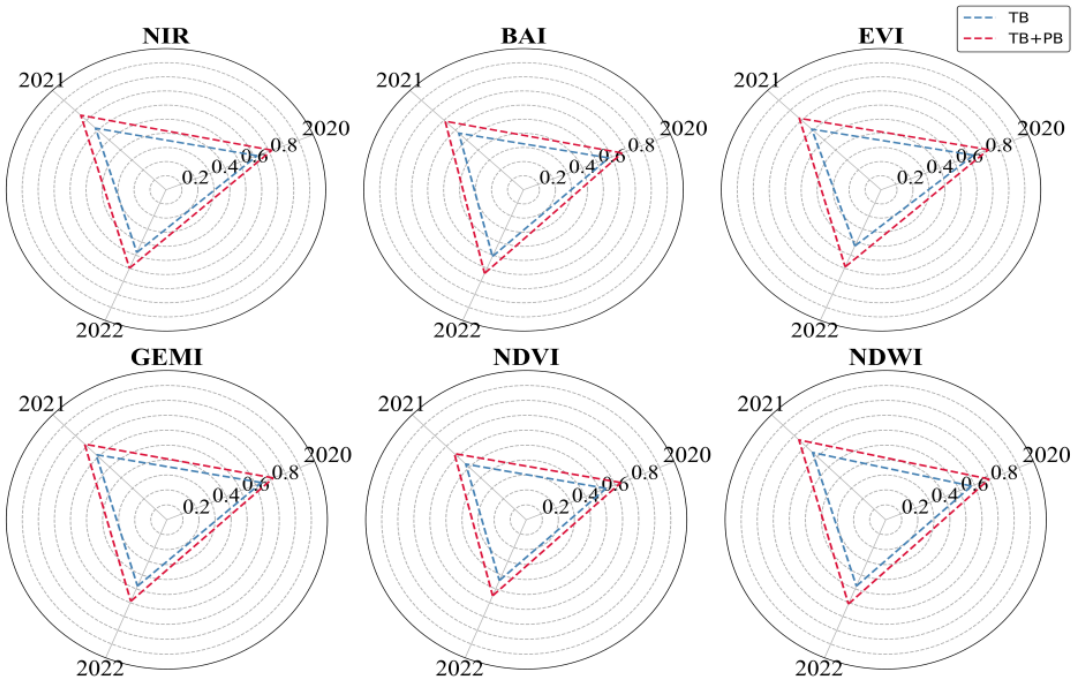

Figure 5.19 allows us to note higher amplitudes between the minimum and maximum values observed in these datasets compared to those labeled with TB cells. If we consider the interannual patterns of all the spectral indices and the NIR band, we do not see major differences between them, with the exception of the NDVI that seems to have the worst performance in all training and testing. An open hypothesis is that in our study area the red band does not act synergically with the NIR band to distinguish vegetation and changes in it caused by fire.

Table 5.8 presents the summary of the IoU results. Contrasting Table 5.8 with Table 5.6 it is possible to note similar results when the reference mapping includes both types of burned cells, despite there is more difference if we consider the reference

mapping labeled with only TB cells. This suggests that models created with only TB cells are well-generalized even when they have a smaller number of available samples. This result has important implications for ML models generation because it is an indicator that in approaches with regular cells, the better samples of the BA class concern homogeneous cells totally affected by fire.

Table 5.8 - Summary of IoU results obtained by the generalized annual datasets created with TB plus PB cells as samples of the BA class based on the multitemporal models.

	IoU	
	TB	**TB + PB**
NIR (2020)	0.62	0.72
NIR (2021)	0.62	0.75
NIR (2022)	0.48	0.6
BAI (2020)	0.58	0.67
BAI (2021)	0.57	0.69
BAI (2022)	0.51	0.64
EVI (2020)	0.63	0.73
EVI (2021)	0.61	0.72
EVI (2022)	0.43	0.59
GEMI (2020)	0.64	0.72
GEMI (2021)	0.62	0.72
GEMI (2022)	0.48	0.59
NDVI (2020)	0.54	0.64
NDVI (2021)	0.53	0.63
NDVI (2022)	0.44	0.55
NDWI (2020)	0.58	0.7
NDWI (2021)	0.64	0.76
NDWI (2022)	0.48	0.61

When comparing the results with the reference mapping with TB and PB cells representing the BA class, we observed that NDWI and NIR yielded very similar IoU results. GEMI and EVI showed IoU values close to those datasets, but the performance of their datasets was weaker in 2022. Notably, the BAI dataset outperformed the others in 2022, although its performance is comparable to the NIR results in 2020 and 2021, as their results are inferior to 70% in both years, but we emphasize that NDVI is less effective for generalization than BAI.

Figure 5.20 structures the results based on the models created with multitemporal datasets labeled only with TB cells. We observe when comparing the classifications with Figure 5.5 the presence of false positives in the BA class, specially in the datasets from 2022. Using both TB and PB cells to generate the models and generalize the results means that a greater number of cells are identified as burned areas when in fact they are not. As we mentioned before regarding the vegetation of our

study area, there appears to be confusion between the BA and NB classes within the CVNP, and using partially burned cells in training increases this confusion.

Figure 5.20 - Annual burned areas classified with models from annual multitemporal datasets labeled with TB plus PB cells as samples of BA.

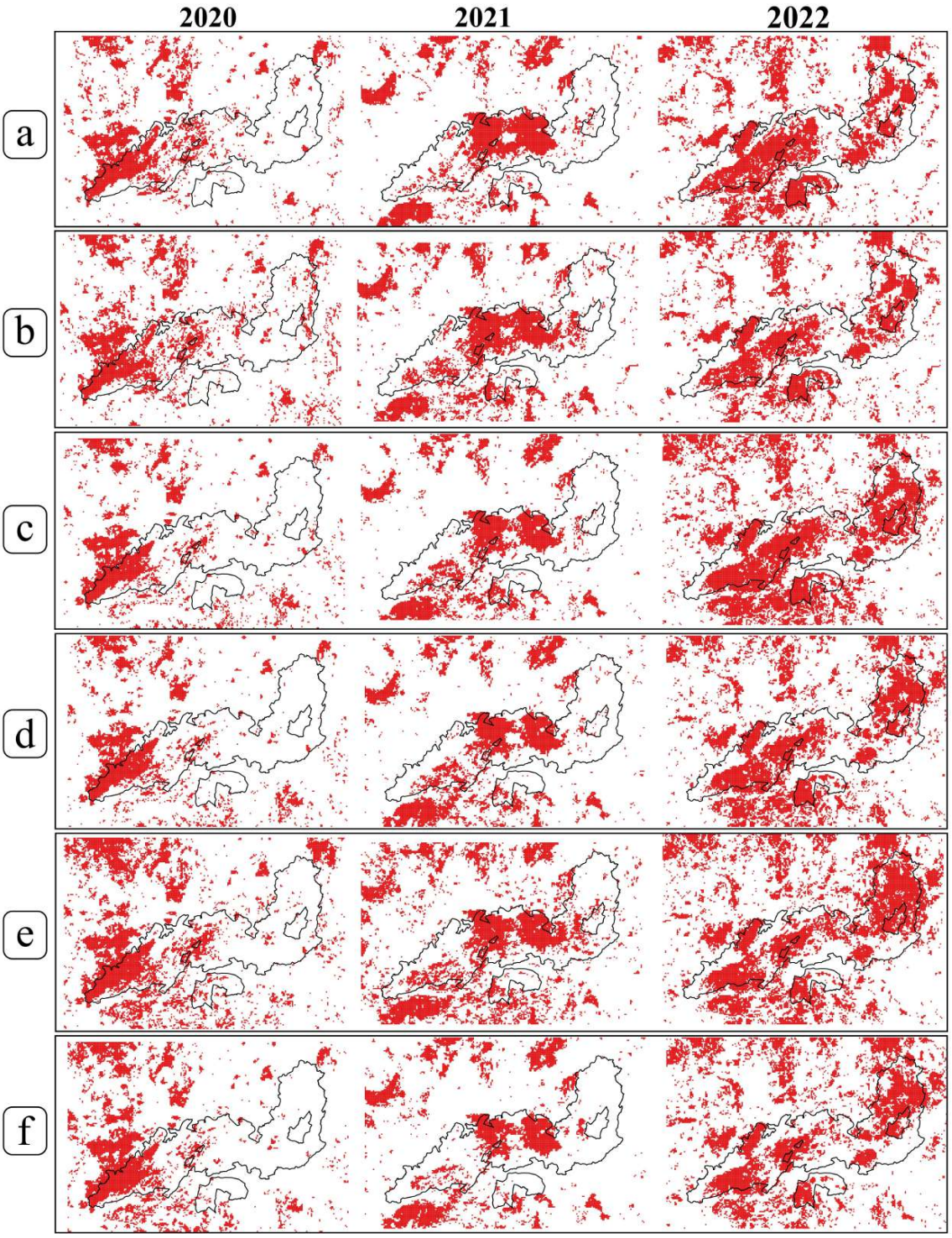

a: NIR; b: BAI; c: EVI; d: GEMI; e: NDVI; f: NDWI.

5.3.2.3 Comparison with MCD64A1 and AQM1km products

Aiming to compare our previous results with the MCD64A1 and AQM1km burned area products, we organized and plotted their annual mappings (Figure 5.21a and Figure 5.21b). We notice comparing them to those in Figure 5.5a and Figure 5.5c that both products demonstrate similar abilities to detect the main annual burn scar patterns. Table 5.9 further reinforces this finding, indicating that, with the exception of the mappings from 2022, the reference mapping that includes TB and PB cells produce higher IoU comparison results.

Figure 5.21 - MCD64A1 and AQM1km annual mappings.

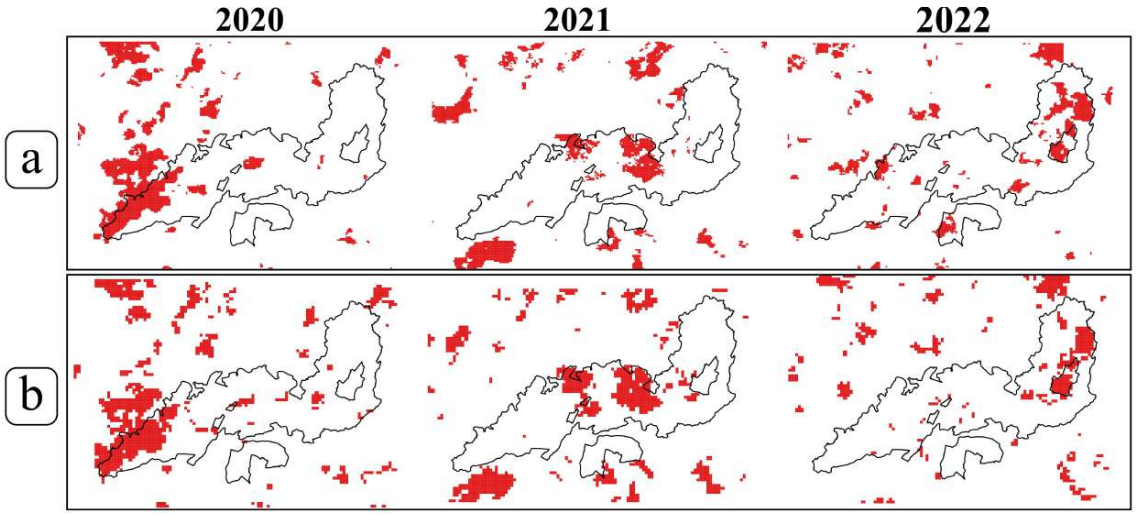

a: MCD64A1; b: AQM1km.

Table 5.9 - Summary of IoU results obtained comparing the manual mappings used as references with the MCD64A1 and AQM1km burned area products.

	IoU	
	TB	**TB + PB**
MCD64A1 (2020)	0.71	0.75
MCD64A1 (2021)	0.72	0.73
MCD64A1 (2022)	0.65	0.64
AQM1km (2020)	0.66	0.72
AQM1km (2021)	0.66	0.71
AQM1km (2022)	0.56	0.56

When we contrast these mappings with those shown in Figure 5.15 and Figure 5.19, we notice that the MCD64A1 and AQM1km are more refined in locating compact burned areas and in avoiding false positives of this class. This indicates that our classifications, while mapping the most burned cells, also generate commission er-

rors, especially in 2022 and when the models are trained using TB and PB cells as input samples. The analysis of Table 5.9 does not show whether one product is more efficient at specifically detecting burned areas, as these IoU results provide an overview of the intersection between the two sets covering all classes.

Figure 5.22 compares the annual datasets classified with TB cells to MCD64A1 and AQM1km products, while Figure 5.21b presents the results obtained using TB and PB cells. Despite the misclassification of unburned cells as burned, we found that the overall IoU results from our datasets labeled only with TB cells are similar to those of MCD64A1 and AQM1km. In the following results, only the validations based on our reference mapping with totally and partially burned cells will be studied in detail, since the overall IoU results tend to be higher, indicating a better correspondence between the reference mapping and the compared mappings.

Figure 5.22 - IoU of the comparisons of the generalized annual datasets and the MCD64A1 and AQM1km products with the reference mappings.

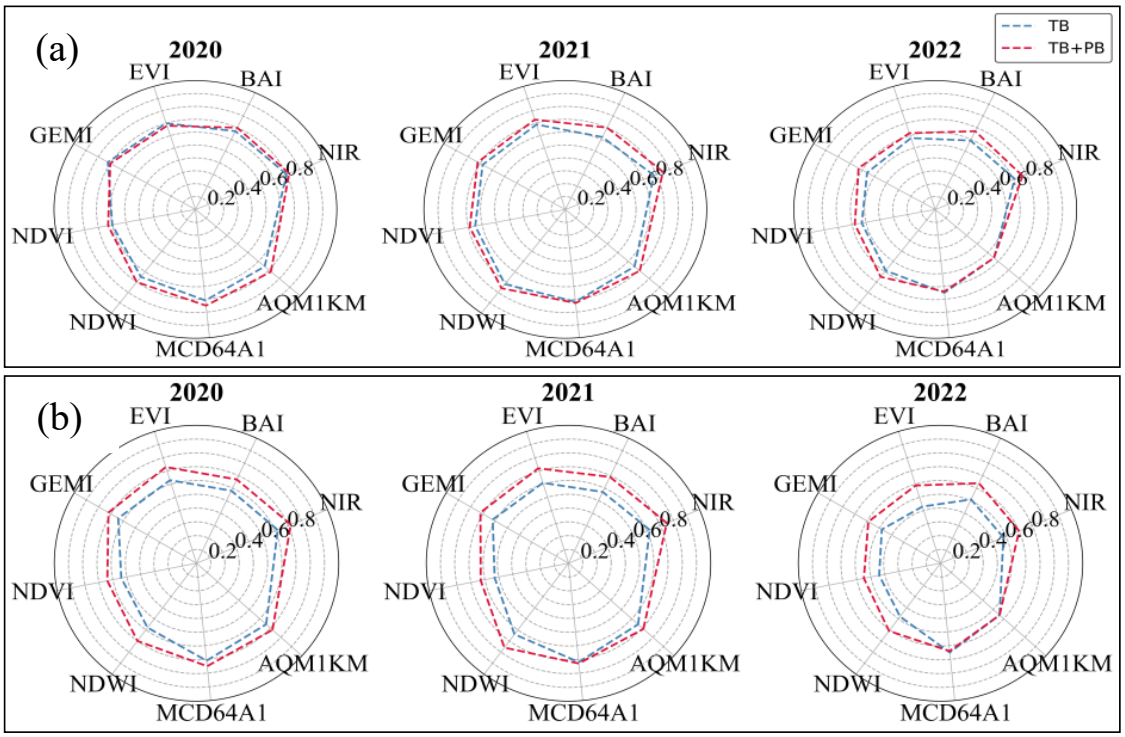

a: classified datasets labeled with TB; b: classified datasets labeled with TB plus PB cells.

Up to this point, we have presented overall results for both classes in the generated classifications as well as for the burned area products. Table 5.10 supplies detailed findings concerning the analysis of the BA class for each comparison mapping, which

have been validated against the reference annual datasets containing TB plus PB cells manually mapped.

Table 5.10 - Summary of validations (precision, recall, F1-score, F2-score, commission and omission errors) for classifications and the MCD64A1 and AQM1km products, based on the reference mapping containing TB and PB cells.

	Precision	**Recall**	**F1-score**	**F2-score**	**Commission errors**	**Omission errors**
2020						
NIR	0.74	0.64	0.69	0.66	0.26	0.36
BAI	0.66	0.65	0.66	0.65	0.34	0.35
EVI	0.67	0.58	0.62	0.6	0.33	0.42
GEMI	0.73	0.58	0.65	0.61	0.27	0.41
NDVI	0.50	0.65	0.57	0.61	0.49	0.35
NDWI	0.63	0.68	0.66	0.67	0.36	0.32
MCD64A1	0.77	0.73	0.75	0.73	0.22	0.27
AQM1km	0.73	0.63	0.68	0.65	0.26	0.37
2021						
NIR	0.72	0.73	0.73	0.73	0.28	0.27
BAI	0.60	0.78	0.68	0.73	0.4	0.22
EVI	0.69	0.71	0.7	0.7	0.31	0.29
GEMI	0.68	0.72	0.67	0.71	0.32	0.28
NDVI	0.6	0.71	0.65	0.69	0.4	0.29
NDWI	0.78	0.72	0.75	0.73	0.22	0.27
MCD64A1	0.84	0.73	0.78	0.75	0.16	0.29
AQM1km	0.75	0.61	0.67	0.63	0.25	0.39
2022						
NIR	0.6	0.65	0.62	0.64	0.39	0.35
BAI	0.58	0.7	0.63	0.67	0.42	0.3
EVI	0.51	0.62	0.56	0.6	0.49	0.38
GEMI	0.5	0.69	0.58	0.64	0.5	0.31
NDVI	0.42	0.66	0.52	0.6	0.58	0.33
NDWI	0.55	0.67	0.61	0.64	0.44	0.33
MCD64A1	0.79	0.52	0.63	0.56	0.22	0.48
AQM1km	0.62	0.28	0.38	0.31	0.38	0.72

The analysis of the classifications from 2020 reveals that, with the exception of NDVI and NDWI, all other mappings yielded higher precisions than recall, indicating that they were more accurate at classifying areas that had actually burned than at detecting them. NDWI, NDVI and BAI were the most efficient datasets at detecting burned areas (higher recall), but the F1-score and F2-score results show that NDWI was more efficient due to its lower omission errors. The MCD64A1 product proved to be the best mapping for classifying and detecting burned areas, returning the lowest commission and omission errors and the higher F1-score and F2-score.

The datasets from 2021 returned higher recalls than precisions. This trend, with exceptions seen in the NDWI dataset, MCD64A1, and AQM1km products, resulted

in 2021 yielding the highest F1-score and F2-score values, alongside the lowest omission errors (excluding AQM1km). Consequently, the datasets from 2021 proved to be the most efficient in accurately detecting burned areas (true positives). However, the commission errors remained similar to those of 2020, indicating the presence of false positives. The AQM1km showed a tendency to underestimate burned areas, but this is to be expected due to its larger minimum mapping unit of 1 km.

The year 2022 had the lowest performance in classifying burned areas, and the MCD64A1 product returned the highest precision, followed by AQM1km and NIR. However, the MCD64A1 and AQM1km recalls were lower, and this led both products to return the lowest F2-score values. Analyzing the errors reveals that although these products exhibit the fewest commission errors, meaning the fewest false positives, they also produce the highest omission errors. In other words, they underestimate the burned area class and generate the greatest number of false negatives between all datasets, meaning that they classify burned areas as being unburned areas. Figure 5.23 shows the results of all commission and omission errors by year and dataset.

Figure 5.23 - Errors of commission and omission for each annual mapping compared to the reference mapping with TB and PB cells.

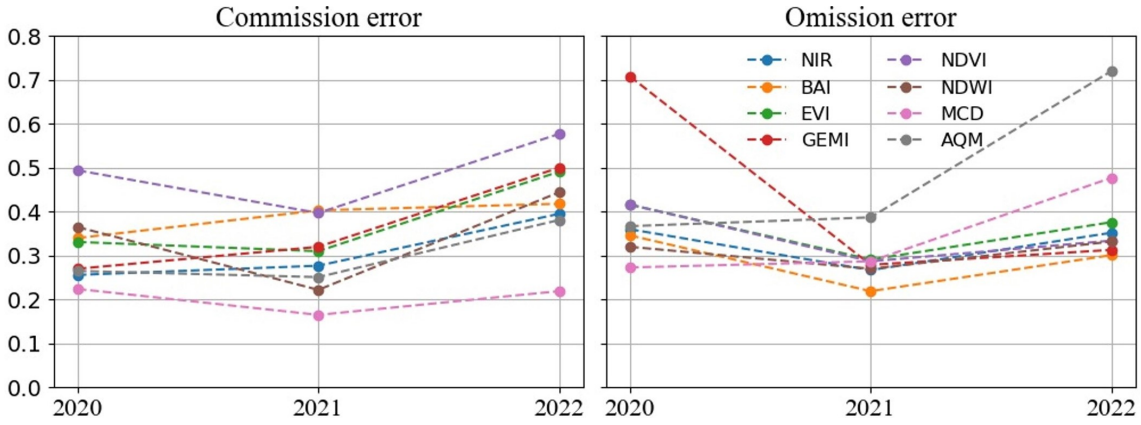

We found that, for all generated classifications based on the multitemporal datasets, 2021 returned the lowest errors of omission. However, the errors of commission were higher in 2021 than in 2020 for the NIR, BAI and GEMI datasets. Despite the tendency to identify more false positives and yield higher commission errors, the 2022 datasets exhibited lower omission errors than those of 2020, with exceptions including the NDWI dataset and the MCD64A1 and AQM1km products. This difference explains why the F2-score metric for 2022 is higher for some datasets than in 2020, while the F1-score is lower. Figure 5.24 shows the accumulated errors and Table 5.11 displays the confusion matrices for all classifications.

Figure 5.24 - Accumulated errors compared to the reference containing TB and PB cells.

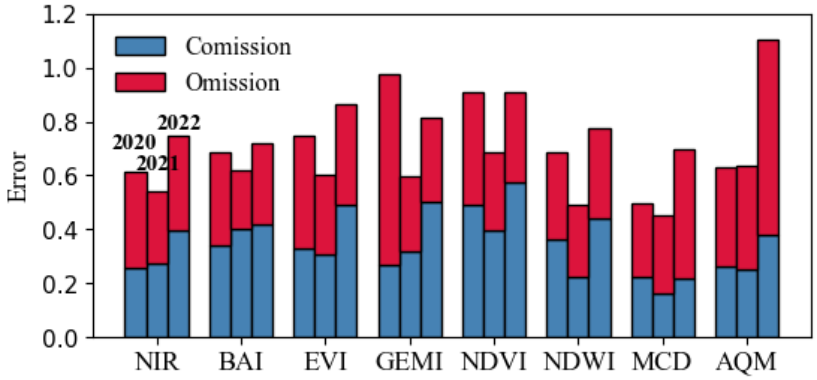

Table 5.11 - Confusion matrices obtained by validations with the annual references containing TB and PB cells.

NIR	**Reference (2020)**	
	BA	NB
BA	**2,975**	1,027
NB	1,674	**33,281**
BAI	BA	NB
BA	**3,039**	1,567
NB	1,610	**32,741**
EVI	BA	NB
BA	**2,713**	1,344
NB	1,936	**32,964**
GEMI	BA	NB
BA	**2,716**	1,007
NB	1,933	**33,301**

NDVI	**Reference (2020)**	
	BA	NB
BA	**3,010**	2,945
NB	1,639	**31,363**
NDWI	BA	NB
BA	**3,157**	1,815
NB	1,492	**32,493**
MCD64A1	BA	NB
BA	**3,377**	976
NB	1,272	**33,332**
AQM1km	BA	NB
BA	**2,942**	1,066
NB	1,707	**33,242**

NIR	**2021**	
	BA	NB
BA	**3,591**	1,376
NB	1,313	**32,677**
BAI	BA	NB
BA	**3,830**	2,596
NB	1,074	**31,457**
EVI	BA	NB
BA	**3,474**	1,563
NB	1,430	**32,490**
GEMI	BA	NB
BA	**3,532**	1,668
NB	1,372	**32,385**

NDVI	**2021**	
	BA	NB
BA	**3,493**	2,307
NB	1,411	**31,746**
NDWI	BA	NB
BA	**3,532**	1,010
NB	1,372	**33,043**
MCD64A1	BA	NB
BA	**3,586**	709
NB	1,448	**33,214**
AQM1km	BA	NB
BA	**3,003**	1,008
NB	1,901	**33,045**

NIR	**2022**	
	BA	NB
BA	**3,384**	2,218
NB	1,844	**31,511**
BAI	BA	NB
BA	**3,650**	2,622
NB	1,578	**31,107**
EVI	BA	NB
BA	**3,259**	3,145
NB	1,969	**30,584**
GEMI	BA	NB
BA	**3,590**	3,597
NB	1,638	**30,132**

NDVI	**2022**	
	BA	NB
BA	**3,477**	4,744
NB	1,751	**28,985**
NDWI	BA	NB
BA	**3,488**	2,786
NB	1,740	**30,943**
MCD64A1	BA	NB
BA	**2,755**	777
NB	2,516	**32,909**
AQM1km	BA	NB
BA	**1,463**	903
NB	3,765	**32,826**

Figure 5.25 shows radar plots for the three years. The year 2021 was the one with the best prediction among the annual classifications models using multitemporal datasets, because its F2-values tended to be higher, indicating higher recalls for the BA class. This year, as explained earlier, contains images from both CBERS-4 and AMAZONIA-1, which makes it more regular than 2020, in which there are only images from CBERS-4, but less dense than 2022. Incorporating images from CBERS-4A, AMAZONIA-1, and CBERS-4 in our datasets would enable the detection of burned areas every 1-3 days under ideal conditions.

Figure 5.25 - Validation metrics (precision, recall, F1-score and F2-score) for all analyzed annual mappings compared to the reference with TB and PB cells as the BA class.

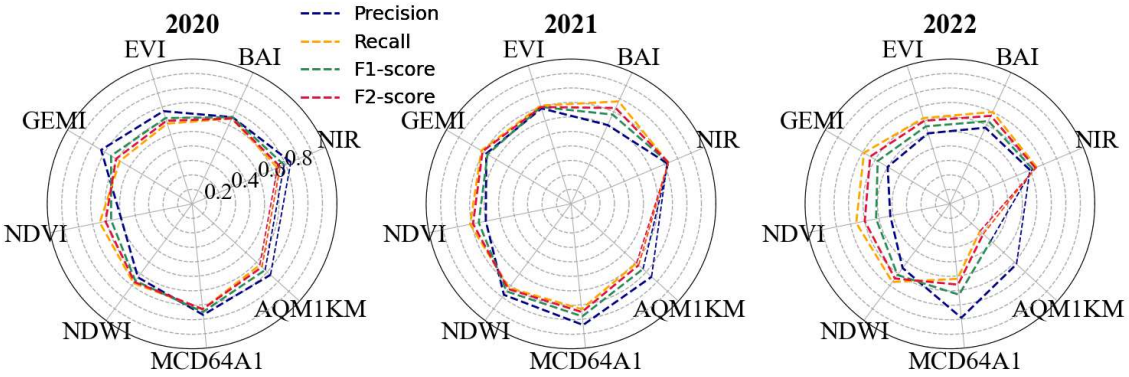

We emphasize that all multitemporal datasets were composed with samples from the three years. One hypothetical reason for the worst performances in 2022 is the increased data variability over shorter time intervals. Unburned cells could be incorrectly mapped as burned because their values may fall below or above the thresholds set by the RF algorithm, influenced by the fire behaviors of 2020 and 2021. It is possible that the variability in 2022 is higher due to radiometric differences between the three satellites, as studied by Oldoni (2022), but our study is limited in understanding it due to the absence of CBERS-4 images before May 2022.

With more regular inter-annual time series, we would be able to explore whether using the three satellites leads to increased variability and whether this variability reflects more unpredictable classifications or not. Aiming to understand if the classifications and the products could be considered similar, we performed paired McNemar tests using the manual mapping with TB and PB cells as reference (Table 5.12). The NIR classification for the year 2021 is not statistically significantly different from the EVI, GEMI, and AQM1km classifications, and the AQM1km does

not exhibit statistical differences when compared to BAI and NDWI. In 2020, the only statistically indistinguishable classifications are BAI and NDWI.

Table 5.12 - Results of paired McNemar binary test performed using as references the mapping with TB and PB cells, the MCD64A1 and the AQM1km products.

Reference	**Year**	**Classification 1**	**Classification 2**	***p-value***
TB+PB	2020	BAI	NDWI	0.301
TB+PB	2021	NIR	EVI	0.893
TB+PB	2021	NIR	GEMI	0.289
TB+PB	2021	NIR	AQM1km	0.182
TB+PB	2021	BAI	AQM1km	0.576
TB+PB	2021	NDWI	AQM1km	0.081

H0: None of the two classifications performs better than the other.

6 CONCLUSIONS

Our main conclusions are:

1. It is possible to map burned areas using WFI imagery, but there are factors to be considered. The limited number of bands and the absence of the SWIR mean that mapping methods need to exploit different RS approaches, based mainly on the red and NIR bands due to the relationship between burned areas and vegetation cover. We focused on exploring the potential of using spectral indices and the NIR band to generate semi-annual and annual mappings for the Cerrado in the CVNP, and annual models performed better than semi-annual models. Despite the irregularity of the time series due to presence of clouds and absence of WFI images from CBERS-4 in 2020 and 2021, our tests showed better results of generalization when we used multitemporal datasets with samples from all years.

2. Using regular cells with an MMU larger than the original WFI pixel size enables integrating data from various Brazilian satellites. Its implication is the possibility to generate annual mappings since the year 1999 based on the visible and NIR bands, which are present in the CBERS family since its inception. Burned areas, although they follow an annual seasonality due to environmental conditions, do not behave equally in all years. In classifications with RF, the use of multitemporal time series, including burned areas from different years and constructed with WFI images from different satellites, has the potential to improve the detection of this target. The tests performed on 38,957 cells demonstrated its capacity for processing large datasets. It is important in big earth data context and it is aligned with AI techniques that support RS and environmental data processing and analysis.

3. According to the results of the training and generalization tests, conducted individually for the NIR band and for the BAI, EVI, GEMI, NDVI and NDWI spectral indices, no major differences between these datasets were found, although some performed better than others in classifications using semi-annual and annual time series. Despite the lack of clarity regarding the dominance of certain datasets in accurately mapping burned areas, the McNemar test, performed on pairs of generalized mappings, revealed significant differences in the annual results, specially evident in the datasets of 2020 and 2022. In 2021, the EVI and GEMI, along with the AQM1km burned area product, returned significant similarities with the results obtained by generalizing the multi-temporal dataset based on the NIR band. It may indicates redundancy between this band and the derived spectral indices for the year 2021.

4. The frontier of knowledge in the context of this work lies in the potential to detect burned areas accurately in near real-time (NRT) by utilizing AI and big datasets, and the greatest advantage of using the WFI sensor is the possibility to obtain images every 1-3 days when the CBERS-4, CBERS-4A and AMAZONIA-1 satellites are used. Another significant potential lies in the production of annual burned area maps since 1999, as Brazil lacks a systematic methodology for producing burned area from its satellites. Future studies could focus on evaluating the performance of techniques such as principal component analysis, IHS transformation, and the integration of all these data into a single time series and the utilization of algorithms based on deep learning architectures. Brazil's autonomy in mapping burned areas with its satellites is considered a critical national asset for environmental monitoring and sovereignty.

REFERENCES

ALDANA-MARTÍN, J. F.; GARCÍA-NIETO, J.; ROLDÁN-GARCÍA, M. del M.; ALDANA-MONTES, J. F. Semantic modelling of earth observation remote sensing. **Expert Systems with Applications**, v. 187, p. 1–13, 2022. Available from: <<https://doi.org/10.1016/j.eswa.2021.115838>>. 17

ALENCAR, A. A.; ARRUDA, V. L.; SILVA, W. V. d.; CONCIANI, D. E.; COSTA, D. P.; CRUSCO, N.; DUVERGER, S. G.; FERREIRA, N. C.; FRANCA-ROCHA, W.; HASENACK, H.; MARTENEXEN, L. F. M.; PIONTEKOWSKI, V. J.; RIBEIRO, N. V.; ROSA, E. R.; ROSA, M. R.; SANTOS, S. M. B.; SHIMBO, J. Z.; VÉLEZ-MARTIN, E. Long-term landsat-based monthly burned area dataset for the brazilian biomes using deep learning. **Remote Sensing**, v. 14, n. 11, p. 2510, 2022. Available from: <<https://doi.org/10.3390/rs14112510>>. 2, 3, 22

BARRADAS, A. C. S.; BORGES, M. A.; COSTA, M. M.; RIBEIRO, K. T. Paradigmas da gestão do fogo em áreas protegidas no mundo e o caso da Estação Ecológica Serra Geral do Tocantins. **Biodiversidade Brasileira**, v. 10, n. 2, p. 71–86, 2020. 8

BASTARRIKA, A.; CHUVIECO, E.; MARTÍN, M. P. Mapping burned areas from Landsat TM/ETM+ data with a two-phase algorithm: balancing omission and commission errors. **Remote Sensing of Environment**, v. 115, n. 4, p. 1003–1012, 2011. Available from: <<https://doi.org/10.1016/j.rse.2010.12.005>>. 13

BATALHA, M. A. O cerrado não é um bioma. **Biota Neotropica**, v. 11, p. 21–24, 2011. Available from: <<https://doi.org/10.1590/S1676-06032011000100001>>. 5

BELGIU, M.; DRĂGUŢ, L. Random forest in remote sensing: a review of applications and future directions. **ISPRS Journal of Photogrammetry and Remote Sensing**, v. 114, p. 24–31, 2016. Available from: <<https://doi.org/10.1016/j.isprsjprs.2016.01.011>>. 18

BERLINCK, C.; LIMA, L. Implementation of integrated fire management in brazilian federal protected areas: results and perspectives. **Biodiversidade Brasileira**, v. 11, p. 1–11, 2021. Available from: <<https://doi.org/10.37002/biodiversidadebrasileira.v11i2.1709>>. 8

BLASCHKE, T. Object based image analysis for remote sensing. **ISPRS Journal of Photogrammetry and Remote Sensing**, v. 65, n. 1, p. 2–16, 2010. Available from: <<https://doi.org/10.1016/j.isprsjprs.2009.06.004>>. 20

BLASCHKE, T.; HAY, G. J.; KELLY, M.; LANG, S.; HOFMANN, P.; ADDINK, E.; FEITOSA, R. Q.; MEER, F. Van der; WERFF, H. Van der; COILLIE, F. V.; TIEDE, D. Geographic object-based image analysis–towards a new paradigm. **ISPRS Journal of Photogrammetry and Remote Sensing**, v. 87, p.

180–191, 2014. Available from: <<https://doi.org/10.1016/j.isprsjprs.2013.09.014>>. 20

BLASCHKE, T.; STROBL, J. What is wrong with pixels: some recent developments interfacing remote sensing and gis. **Zeitschrift für Geoinformationssysteme**, v. 6, p. 12–17, 2001. 20

BRASIL. **Projeto de Lei n. 1.818, de 2022. Institui a Política Nacional de Manejo Integrado do Fogo; e altera as Leis n.s 7.735, de 22 de fevereiro de 1989, 12.651, de 25 de maio de 2012 (Código Florestal), e 9.605, de 12 de fevereiro de 1998**. 2022. Access in: 04 jul. 2023. Available from: <<https://www25.senado.leg.br/web/atividade/materias/-/materia/153865>>. 8

BRASIL. MINISTÉRIO DO MEIO AMBIENTE E DA MUDANÇA DO CLIMA (MMA). **Brazil's forest reference emission level for reducing emissions from deforestation in the Cerrado biome for results-based payments for REDD+ under the United Nations Framework Convention on Climate Change**. Brasília: MMA, 2017. 5

_____. **Plano de ação para Prevenção e Controle do Desmatamento e das Queimadas no Cerrado - PPC Cerrado e Plano de Ação para Prevenção e Controle do Desmatamento na Amazônia Legal (PPCDAm)**. Brasília: MMA, 2018. 3

BREIMAN, L. Random forests. **Machine Learning**, v. 45, p. 5–32, 2001. Available from: <<https://doi.org/10.1023/A:1010933404324>>. 18

BUSTAMANTE, M. M.; SILVA, J. S.; SCARIOT, A.; SAMPAIO, A. B.; MASCIA, D. L.; GARCIA, E.; SANO, E.; FERNANDES, G. W.; DURIGAN, G.; ROITMAN, I.; FIGUEIREDO, I.; RODRIGUES, R. R.; PILLAR, V. D.; OLIVEIRA, A. O.; MALHADO, A. C.; ALENCAR, A.; VENDRAMINI, A.; PADOVEZI, A.; CARRASCOSA, H.; FREITAS, J.; SIQUEIRA, J. A.; SHIMBO, J.; GENEROSO, L. G.; TABARELLI, M.; BIDERMAN, R.; SALOMÃO, R. P.; VALLE, R.; JUNIOR, B.; NOBRE, C. Ecological restoration as a strategy for mitigating and adapting to climate change: lessons and challenges from Brazil. **Mitigation and Adaptation Strategies for Global Change**, v. 24, p. 1249–1270, 2019. Available from: <<https://doi.org/10.1007/s11027-018-9837-5>>. 1

BUSTAMANTE, M. M. C.; OLIVEIRA, E. L. Impacto das atividades agrícolas, florestais e pecuárias nos recursos naturais. In: FALEIRO, F. G.; NETO, A. L. F. (Ed.). **Savanas: desafios e estratégias para o equilíbrio entre sociedade, agronegócio e recursos naturais**. Planaltina: EMBRAPA Cerrados, 2008. p. 647–649. 1

CARVALHO-JÚNIOR, O. A.; GUIMARÃES, R. F.; SILVA, C. R.; GOMES, R. A. T. Standardized time-series and interannual phenological deviation: New techniques for burned-area detection using long-term MODIS-NBR dataset. **Remote Sensing**, v. 7, n. 6, p. 6950–6985, 2015. Available from: <<https://doi.org/10.3390/rs70606950>>. 16

CHAVES, M. E.; SOARES, A. R.; SANCHES, I. D.; FRONZA, J. G. Cbers data cubes for land use and land cover mapping in the brazilian cerrado agricultural belt. **International Journal of Remote Sensing**, v. 42, n. 21, p. 8398–8432, 2021. Available from: <<https://doi.org/10.1080/01431161.2021.1978584>>. 16

CHAVEZ-JR, P. S. An improved dark-object subtraction technique for atmospheric scattering correction of multispectral data. **Remote Sensing of Environment**, v. 24, n. 3, p. 459–479, 1988. 28

CHUVIECO, E.; LIZUNDIA-LOIOLA, J.; PETTINARI, M. L.; RAMO, R.; PADILLA, M.; TANSEY, K.; MOUILLOT, F.; LAURENT, P.; STORM, T.; HEIL, A.; PLUMMER, S. Generation and analysis of a new global burned area product based on MODIS 250 m reflectance bands and thermal anomalies. **Earth System Science Data**, v. 10, n. 4, p. 2015–2031, 2018. Available from: <<https://doi.org/10.5194/essd-10-2015-2018>>. 21

CHUVIECO, E.; MARTIN, M. P.; PALACIOS, A. Assessment of different spectral indices in the red-near-infrared spectral domain for burned land discrimination. **International Journal of Remote Sensing**, v. 23, n. 23, p. 5103–5110, 2002. Available from: <<https://doi.org/10.1080/01431160210153129>>. 10, 14

COLLI, G. R.; VIEIRA, C. R.; DIANESE, J. C. Biodiversity and conservation of the Cerrado: recent advances and old challenges. **Biodiversity and Conservation**, v. 29, n. 5, p. 1465–1475, 2020. Available from: <<https://doi.org/10.1007/s10531-020-01967-x>>. 1

CORCORAN, J.; KNIGHT, J.; PELLETIER, K.; RAMPI, L.; WANG, Y. The effects of point or polygon based training data on randomforest classification accuracy of wetlands. **Remote Sensing**, v. 7, n. 4, p. 4002–4025, 2015. Available from: <<https://doi.org/10.3390/rs70404002>>. 22

COUTINHO, L. M. O conceito do cerrado. **Revista Brasileira de Botânica**, v. 1, p. 17–23, 1978. xi, 5

_____. O conceito de bioma. **Acta Botanica Brasilica**, v. 20, p. 13–23, 2006. Available from: <<https://doi.org/10.1590/S0102-33062006000100002>>. 5

CSILLIK, O. Superpixels: the end of pixels in OBIA. A comparison of state-of-the-art superpixel methods for remote sensing data. In: KERLE, N.; GERKE, M.; LEFEVRE, S. (Ed.). **Proceedings of the GEOBIA 2016: Solutions and Synergies**. Enschede, The Netherlands, 2016. Available from: <<https://doi.org/10.3990/2.439>>. 20

DURIGAN, G.; PILON, N. A. L.; ABREU, R. C. R.; HOFFMANN, W. A.; MARTINS, M.; FIORILLO, B. F.; ANTUNES, A. Z.; CARMIGNOTTO, A. P.; MARAVALHAS, J. B.; VIEIRA, J.; VASCONCELOS, H. L. No net loss of species diversity after prescribed fires in the Brazilian savanna. **Frontiers in Forests and Global Change**, v. 3, p. 13, 2020. Available from: <<https://doi.org/10.3389/ffgc.2020.00013>>. 1, 8

DURIGAN, G.; RATTER, J. A. The need for a consistent fire policy for Cerrado conservation. **Journal of Applied Ecology**, v. 53, n. 1, p. 11–15, 2016. Available from: <<https://doi.org/10.1111/1365-2664.12559>>. 8

DUTRA, R. M. S.; SOUZA, M. M. O. d. Cerrado, revolução verde e evolução do consumo de agrotóxicos. **Sociedade & Natureza**, v. 29, p. 473–488, 2022. Available from: <<https://doi.org/10.14393/SN-v29n3-2017-8>>. 1

EITEN, G. **Classificação da vegetação do Brasil**. Brasília, DF: Conselho Nacional de Desenvolvimento Científico e Tecnológico - CNPq, 1983. 305 p. 5

EPIPHANIO, J. C. N. CBERS: estado atual e futuro. In: SIMPÓSIO BRASILEIRO DE SENSORIAMENTO REMOTO, 14., 2009. **Anais...** São José dos Campos: INPE, 2009. p. 2001–2008. 10, 11, 28

FARIA, K. M. S.; SANTOS, R. A. Análise espacial da densidade de fragmentos remanescentes e da estrutura da paisagem na sub-bacia do Rio Caiapó–GO. **Ateliê Geográfico**, v. 10, p. 355–363, 2016. Available from: <<https://doi.org/10.5216/ag.v10i2.38627>>. 1

FERREIRA, K. R.; QUEIROZ, G. R.; VINHAS, L.; MARUJO, R. F.; SIMOES, R. E.; PICOLI, M. C.; CAMARA, G.; CARTAXO, R.; GOMES, V. C.; SANTOS, L. A.; SANCHEZ, A. H.; ARCANJO, J. S.; FRONZA, J. G.; NORONHA, C. A.; COSTA, R. W.; ZAGLIA, M. C.; ZIOTI, F.; KORTING, T. S.; SOARES, A. R.; CHAVES, M. E. D.; FONSECA, L. M. G. Earth observation data cubes for Brazil: requirements, methodology and products. **Remote Sensing**, v. 12, n. 24, p. 1–19, 2020. Available from: <<https://doi.org/10.3390/rs12244033>>. 11, 17

FIDELIS, A.; ALVARADO, S. T.; BARRADAS, A. C. S.; PIVELLO, V. R. The year 2017: Megafires and management in the Cerrado. **Fire**, v. 1, n. 3, p. 49, 2018. Available from: <<https://doi.org/10.3390/fire1030049>>. 1, 2, 8, 24

FLETCHER, S.; ISLAM, M. Z. Comparing sets of patterns with the jaccard index. **Australasian Journal of Information Systems**, v. 22, 2018. Available from: <<https://doi.org/10.3127/ajis.v22i0.1538>>. 22

FRANKE, J.; BARRADAS, A. C. S.; BORGES, M. A.; COSTA, M. M.; DIAS, P. A.; HOFFMANN, A. A.; FILHO, J. C. O.; MELCHIORI, A. E.; SIEGERT, F. Fuel load mapping in the Brazilian Cerrado in support of integrated fire management. **Remote Sensing of Environment**, v. 217, p. 221–232, 2018. Available from: <<https://doi.org/10.1016/j.rse.2018.08.018>>. 13

GAVEAU, D. L.; DESCALS, A.; SALIM, M. A.; SHEIL, D.; SLOAN, S. Refined burned-area mapping protocol using Sentinel-2 data increases estimate of 2019 indonesian burning. **Earth System Science Data**, v. 13, n. 11, p. 5353–5368, 2021. Available from: <<https://doi.org/10.5194/essd-13-5353-2021>>. 3, 21

GIGLIO, L.; BOSCHETTI, L.; ROY, D. P.; HUMBER, M. L.; JUSTICE, C. O. The collection 6 MODIS burned area mapping algorithm and product. **Remote**

Sensing of Environment, v. 217, p. 72–85, 2018. Available from: <<https://doi.org/10.1016/j.rse.2018.08.005>>. 21, 22

GÓMEZ, C.; WHITE, J. C.; WULDER, M. A. Characterizing the state and processes of change in a dynamic forest environment using hierarchical spatio-temporal segmentation. **Remote Sensing of Environment**, v. 115, n. 7, p. 1665–1679, 2011. Available from: <<https://doi.org/10.1016/j.rse.2011.02.025>>. 20

GOTTSBERGER, G.; SILBERBAUER-GOTTSBERGER, I. How are pollination and seed dispersal modes in cerrado related to stratification? trends in a cerrado sensu stricto woodland in southeastern Brazil, and a comparison with neotropical forests. **Acta Botanica Brasilica**, v. 32, p. 434–445, 2018. Available from: <<https://doi.org/10.1590/0102-33062018abb0186>>. 5

GREGORIO, A. D. **Land cover classification system: classification concepts and user manual: LCCS**. [S.l.]: Food & Agriculture Organization, 2005. 15

HARRIS, C. R.; MILLMAN, K. J.; WALT, S. J. V. D.; GOMMERS, R.; VIRTANEN, P.; COURNAPEAU, D.; WIESER, E.; TAYLOR, J.; BERG, S.; SMITH, N. J.; KERN, R.; PICUS, M.; HOYER, S.; KERKWIJK, M. H. V.; BRETT, M.; HALDANE, A.; RÍO, J. F. D.; WIEBE, M.; PETERSON, P.; GÉRARD-MARCHANT, P.; SHEPPARD, K.; REDDY, T.; WECKESSER, W.; ABBASI, H.; GOHLKE, C.; OLIPHANT, T. E. Array programming with NumPy. **Nature**, v. 585, n. 7825, p. 357–362, 2020. Available from: <<https://doi.org/10.1038/s41586-020-2649-2>>. 29

HAY, G. J.; CASTILLA, G. Geographic Object-Based Image Analysis (GEOBIA): a new name for a new discipline. In: BLASCHKE, T.; LANG, S.; HAY, G. J. (Ed.). **Object-Based Image Analysis: Spatial Concepts for Knowledge-Driven Remote Sensing Applications**. Berlin: Springer, 2008. p. 75–89. 20

HOFFMAN, C.; FERNANDES, P.; MORGAN, P.; REGO, F. C. **Fire science**: from chemistry to landscape management. Switzerland: Springer, 2021. 644 p. 9

HOFMANN, G. S.; CARDOSO, M. F.; ALVES, R. J.; WEBER, E. J.; BARBOSA, A. A.; TOLEDO, P. M. de; PONTUAL, F. B.; SALLES, L. d. O.; HASENACK, H.; CORDEIRO, J. L.; AQUINO, F. E.; OLIVEIRA, L. F. B. The Brazilian Cerrado is becoming hotter and drier. **Global Change Biology**, v. 27, n. 17, p. 4060–4073, 2021. Available from: <<https://doi.org/10.1111/gcb.15712>>. 1

HUETE, A.; DIDAN, K.; MIURA, T.; RODRIGUEZ, E. P.; GAO, X.; FERREIRA, L. G. Overview of the radiometric and biophysical performance of the MODIS vegetation indices. **Remote Sensing of Environment**, v. 83, n. 1-2, p. 195–213, 2002. Available from: <<https://doi.org/10.1016/S0034-4257(02)00096-2>>. 14

HUMBER, M. L.; BOSCHETTI, L.; GIGLIO, L.; JUSTICE, C. O. Spatial and temporal intercomparison of four global burned area products. **International Journal of Digital Earth**, v. 12, n. 4, p. 460–484, 2019. Available from: <<https://doi.org/10.1080/17538947.2018.1433727>>. 22

INSTITUTO BRASILEIRO DE GEOGRAFIA E ESTATÍSTICA (IBGE). **Manual técnico da vegetação brasileira**. Rio de Janeiro: IBGE, 2012. 6, 23, 24

INSTITUTO CHICO MENDES DE CONSERVAÇÃO DA BIODIVERSIDADE (ICMBIO). **Plano de manejo do Parque Nacional da Chapada dos Veadeiros**. Brasília: ICMBIO, 2021. 23

_____. **Plano de Manejo Integrado do Fogo: Parque Nacional da Chapada dos Veadeiros**. Brasília: ICMBIO, 2022. 24

INSTITUTO NACIONAL DE PESQUISAS ESPACIAIS (INPE). **TerraClass**. 2023a. Available from: <<https://www.terraclass.gov.br/geoportal-cerrado/>>. Access in: 01 jul. 2023. 2

_____. **Banco de Dados de Queimadas**. 2023b. Available from: <<http://www.inpe.br/queimadas/bdqueimadas>>. Access in: 01 jul. 2023. 2, 7, 22, 25

_____. **TerraBrasilis**. 2023c. Available from: <<http://terrabrasilis.dpi.inpe.br/downloads/>>. Access in: 02 sep. 2023. 25

_____. **Catálogo de Imagens**. 2023d. Available from: <<http://www2.dgi.inpe.br/catalogo/>>. Access in: 03 fev. 2023. 26

JENSEN, J. R. **Sensoriamento remoto do ambiente**: uma perspectiva em recursos terrestres. São José dos Campos: Parêntese, 2009. 598 p. 2, 9

JIN, S.; YANG, L.; DANIELSON, P.; HOMER, C.; FRY, J.; XIAN, G. A comprehensive change detection method for updating the National Land Cover Database to circa 2011. **Remote Sensing of Environment**, v. 132, p. 159–175, 2013. Available from: <<https://doi.org/10.1016/j.rse.2013.01.012>>. 16

JOHANSEN, K.; ARROYO, L. A.; PHINN, S.; WITTE, C. Comparison of geo-object based and pixel-based change detection of riparian environments using high spatial resolution multi-spectral imagery. **Photogrammetric Engineering & Remote Sensing**, v. 76, n. 2, p. 123–136, 2010. Available from: <<https://doi.org/10.14358/PERS.76.2.123>>. 20

JORDAHL, K.; BOSSCHE, J. V. D.; FLEISCHMANN, M.; WASSERMAN, J.; MCBRIDE, J.; GERARD, J.; TRATNER, J.; PERRY, M.; BADARACCO, A. G.; FARMER, C.; HJELLE, G. A.; SNOW, A. D.; COCHRAN, M.; GILLIES, S.; CULBERTSON, L.; BARTOS, M.; EUBANK, N.; MAXALBERT; BILOGUR, A.; REY, S.; REN, C.; ARRIBAS-BEL, D.; WASSER, L.; WOLF, L. J.; JOURNOIS, M.; WILSON, J.; GREENHALL, A.; HOLDGRAF, C.; FILIPE; LEBLANC, F. **geopandas/geopandas: v0.8.1**. jul. 2020. Available from: <<https://doi.org/10.5281/zenodo.3946761>>. 33

JÚNIOR, A. C. P.; OLIVEIRA, S. L.; PEREIRA, J. M.; TURKMAN, M. A. A. Modelling fire frequency in a Cerrado savanna protected area. **PloS One**, v. 9, n. 7, p. 1–11, 2014. Available from: <<https://doi.org/10.1371/journal.pone.0102380>>. 7

KEELEY, J. E. Fire intensity, fire severity and burn severity: a brief review and suggested usage. **International Journal of Wildland Fire**, v. 18, n. 1, p. 116–126, 2009. Available from: <<https://doi.org/10.1071/WF07049>>. 2, 8, 12

KORTING, T.; CÂMARA, G.; FONSECA, L. M. G. Land cover detection using temporal features based on polar representation. In: CONFERENCE ON GRAPHICS, PATTERNS, AND IMAGES (SIBGRAPI), 26. **Proceedings...** Arequipa, Peru, 2013. 18

KULKARNI, A. D.; LOWE, B. Random forest algorithm for land cover classification. **International Journal on Recent and Innovation Trends in Computing and Communication**, v. 4, p. 58–63, 2016. Available from: <<https://doi.org/10.1109/IGARSS.2003.1294837>>. 18

LABATUT, V.; CHERIFI, H. Accuracy measures for the comparison of classifiers. **arXiv preprint arXiv:1207.3790**, 2012. Available from: <<https://doi.org/10.48550/arXiv.1207.3790>>. 22

LANG, S. Object-based image analysis for remote sensing applications: modeling reality–dealing with complexity. In: BLASCHKE, T.; LANG, S.; HAY, G. J. (Ed.). **Object-Based Image Analysis: Spatial Concepts for Knowledge-Driven Remote Sensing Applications**. Berlin: Springer, 2008. p. 3–27. 20

LENTILE, L. B.; HOLDEN, Z. A.; SMITH, A. M.; FALKOWSKI, M. J.; HUDAK, A. T.; MORGAN, P.; LEWIS, S. A.; GESSLER, P. E.; BENSON, N. C. Remote sensing techniques to assess active fire characteristics and post-fire effects. **International Journal of Wildland Fire**, v. 15, n. 3, p. 319–345, 2006. Available from: <<https://doi.org/10.1071/WF05097>>. 13

LEWIS, S. A.; ROBICHAUD, P. R.; HUDAK, A. T.; STRAND, E. K.; EITEL, J. U.; BROWN, R. E. Evaluating the persistence of post-wildfire ash: a multi-platform spatiotemporal analysis. **Fire**, v. 4, n. 4, p. 68, 2021. Available from: <<https://doi.org/10.3390/fire4040068>>. 13

LI, J.; ZHU, S.; GAO, Y.; ZHANG, G.; XU, Y. Change detection for high-resolution remote sensing images based on a multi-scale attention siamese network. **Remote Sensing**, v. 14, n. 14, p. 3464, 2022. Available from: <<https://doi.org/10.3390/rs14143464>>. 16

LIBONATI, R.; DACAMARA, C. C.; SETZER, A. W.; MORELLI, F.; MELCHIORI, A. E. An algorithm for burned area detection in the Brazilian Cerrado using 4 μm MODIS imagery. **Remote Sensing**, v. 7, n. 11, p. 15782–15803, 2015. Available from: <<https://doi.org/10.3390/rs71115782>>. 21

LIU, P.; LIU, Y.; GUO, X.; ZHAO, W.; WU, H.; XU, W. Burned area detection and mapping using time series sentinel-2 multispectral images. **Remote Sensing of Environment**, v. 296, p. 113753, 2023. Available from: <<https://doi.org/10.1016/j.rse.2023.113753>>. 16

LIU, S.; ZHENG, Y.; DALPONTE, M.; TONG, X. A novel fire index-based burned area change detection approach using landsat-8 oli data. **European Journal of Remote Sensing**, v. 53, n. 1, p. 104–112, 2020. Available from: <<https://doi.org/10.1080/22797254.2020.1738900>>. 16

LIU, Z.; PENG, C.; WORK, T.; CANDAU, J.-N.; DESROCHERS, A.; KNEESHAW, D. Application of machine-learning methods in forest ecology: recent progress and future challenges. **Environmental Reviews**, v. 26, n. 4, p. 339–350, 2018. Available from: <<https://doi.org/10.1139/er-2018-0034>>. 17

LOEBMANN, D. G. S. W. **Classificação fitofisionômica do Cerrado no Parque Nacional da Chapada dos Veadeiros, GO, com a aplicação de uma análise combinatória com filtros adaptativos em imagens TM LANDSAT**. 65 p. Thesis (Master in Geography) — Universidade de Brasilia (UnB), Brasília, 2008. 23, 25

LONG, T.; ZHANG, Z.; HE, G.; JIAO, W.; TANG, C.; WU, B.; ZHANG, X.; WANG, G.; YIN, R. 30 m resolution global annual burned area mapping based on Landsat images and google earth engine. **Remote Sensing**, v. 11, n. 5, p. 489, 2019. Available from: <<https://doi.org/10.3390/rs11050489>>. 21

MAKRIDAKIS, S. The forthcoming artificial intelligence (ai) revolution: its impact on society and firms. **Futures**, v. 90, p. 46–60, 2017. Available from: <<https://doi.org/10.1016/j.futures.2017.03.006>>. 17

MAPBIOMAS. MapBiomas Brasil: o projeto. 2023. Available from: <<https://mapbiomas.org/o-projeto>>. Access in: 01 jul. 2023. 2

MAPBIOMAS FOGO. **Algorithm theoretical basis document (ATBD). Collection 2, Version 1**. 2023. Available from: <<https://mapbiomas.org/atbd---entenda-cada-etapa>>. Access in: 18 July 2023. 21

MATAVELI, G. A. V.; SILVA, M. E. S.; PEREIRA, G.; CARDOZO, F. da S.; KAWAKUBO, F. S.; BERTANI, G.; COSTA, J. C.; RAMOS, R. de C.; SILVA, V. V. da. Satellite observations for describing fire patterns and climate-related fire drivers in the brazilian savannas. **Natural Hazards and Earth System Sciences**, v. 18, n. 1, p. 125–144, 2018. Available from: <<https://doi.org/10.5194/nhess-18-125-2018>>. 43

MCARTHUR, A.; CHENEY, N. The characterization of fires in relation to ecological studies. **Fire Ecology**, v. 11, n. 1, p. 3–9, 2015. Available from: <<https://doi.org/10.1007/BF03400629>>. 12

MCFEETERS, S. K. The use of the Normalized Difference Water Index (NDWI) in the delineation of open water features. **International Journal of Remote Sensing**, v. 17, n. 7, p. 1425–1432, 1996. 14

MCKINNEY, W. Data structures for statistical computing in Python. In: PYTHON IN SCIENCE CONFERENCE, 9. **Proceedings...** Austin, 2010. p. 51–56. Available from: <<10.25080/Majora-92bf1922-00a>>. 35

MEHMOOD, M.; SHAHZAD, A.; ZAFAR, B.; SHABBIR, A.; ALI, N. Remote sensing image classification: a comprehensive review and applications. **Mathematical Problems in Engineering**, v. 2022, p. 1–24, 2022. Available from: <<https://doi.org/10.1155/2022/5880959>>. 17

MELCHIORI, A. E.; CANDIDO, P. A.; LIBONATI, R.; MORELLI, F.; SETZER, A.; JESUS, S. C. de; GARCIA-FONSECA, L.; KORTING, T. Spectral indices and multi-temporal change image detection algorithms for burned area extraction in the brazilian cerrado. In: SIMPÓSIO BRASILEIRO DE SENSORIAMENTO REMOTO, 17., 2015, João Pessoa. **Anais...** São Jose dos Campos: INPE, 2015. p. 643–650. Available from: <<http://dx.doi.org/10.13140/RG.2.1.4314.2562>>. 21

MEYER, W. B.; TURNER, B. Land-use/land-cover change: challenges for geographers. **GeoJournal**, v. 39, p. 237–240, 1996. Available from: <<https://doi.org/10.1007/BF00188373>>. 15

MILNE, A. K. Change direction analysis using Landsat imagery: a review of methodology. In: INTERNATIONAL GEOSCIENCE AND REMOTE SENSING SYMPOSIUM, 1988. **Proceedings...** IEEE, 1988. p. 541–544. Available from: <<https://doi.org/10.1109/IGARSS.1988.570193>>. 16

MISHRA, A.; DASGUPTA, A. Supervised and unsupervised machine learning algorithms for forecasting the fracture location in dissimilar friction-stir-welded joints. **Forecasting**, v. 4, n. 4, p. 787–797, 2022. Available from: <<https://doi.org/10.3390/forecast4040043>>. 17

MOUILLOT, F.; SCHULTZ, M. G.; YUE, C.; CADULE, P.; TANSEY, K.; CIAIS, P.; CHUVIECO, E. Ten years of global burned area products from spaceborne remote sensing – a review: analysis of user needs and recommendations for future developments. **International Journal of Applied Earth Observation and Geoinformation**, v. 26, p. 64–79, 2014. Available from: <<https://doi.org/10.1016/j.jag.2013.05.014>>. 21

MYERS, N.; MITTERMEIER, R. A.; MITTERMEIER, C. G.; FONSECA, G. A. D.; KENT, J. Biodiversity hotspots for conservation priorities. **Nature**, v. 403, n. 6772, p. 853–858, 2000. Available from: <<https://doi.org/10.1038/35002501>>. 1

NASCIMENTO, I. V. Cerrado: o fogo como agente ecológico. **Territorium**, n. 8, p. 25–35, 2001. Available from: <<https://doi.org/10.14195/1647-7723_8_3>>. 7

NATIONAL FIRE CHIEFS COUNCIL (NFCC). **National Fire Chiefs Council: control Measure Knowledge**. 2023. Available from: <<https://www.ukfrs.com/modal/general-cm/14303/347023/document/nojs>>. Access in: 03 oct. 2023. 32

NEGRI, R. G.; LUZ, A. E.; FRERY, A. C.; CASACA, W. Mapping burned areas with multitemporal–multispectral data and probabilistic unsupervised learning. **Remote Sensing**, v. 14, n. 21, p. 5413, 2022. Available from: <<https://doi.org/10.3390/rs14215413>>. 9

NOVO, E. M. L. de M.; PONZONI, F. J. **Introdução ao sensoriamento remoto**. São José dos Campos: Instituto Nacional de Pesquisas Espaciais, 2001. 68 p. 9

NUNES, B. Y. C.; SIMÕES, L. da S.; AQUINO, G. S. de; ROSA, R.; REZENDE, P. S. Correção atmosférica de imagens do sensor WFI do CBERS-4 através do método dark object subtraction (DOS). In: SIMPÓSIO BRASILEIRO DE SENSORIAMENTO REMOTO, 19., 2019, Santos. **Anais...** São Jose dos Campos: INPE, 2019. p. 935–938. 28

OLDONI, L. V. **Harmonization of WFI data from the CBERS-4, CBERS-4A and AMAZONIA-1 satellites for agricultural applications**. 216 p. Thesis (PhD in Remote Sensing) — Instituto Nacional de Pesquisas Espaciais (INPE), São Jose dos Campos, 2022. 3, 10, 11, 12, 64

OVERBECK, G. E.; VÉLEZ-MARTIN, E.; SCARANO, F. R.; LEWINSOHN, T. M.; FONSECA, C. R.; MEYER, S. T.; MÜLLER, S. C.; CEOTTO, P.; DADALT, L.; DURIGAN, G.; GANADE, G.; GOSSNER, M. M.; GUADAGNIN, D. L.; LORENZEN, K.; JACOBI, C. M.; WEISSER, W. W.; PILLAR, V. D. Conservation in Brazil needs to include non-forest ecosystems. **Diversity and Distributions**, v. 21, n. 12, p. 1455–1460, 2015. Available from: <<https://doi.org/10.1111/ddi.12380>>. 1

PARVEEN, S.; BASHEER, J.; PRAVEEN, B. A literature review on land use land cover changes. **International Journal of Advanced Research**, v. 6, n. 7, p. 1–6, 2018. Available from: <<http://dx.doi.org/10.21474/IJAR01/7327>>. 15

PASTOR, C. Q.; SHIMABUKURO, Y. E. Estimación de superficie quemada mediante la aplicación sinérgica de obia y sma a imágenes WFI CBERS. In: SIMPÓSIO BRASILEIRO DE SENSORIAMENTO REMOTO, 14., 2009, Natal. **Anais...** São Jose dos Campos: INPE, 2009. p. 2119–2126. 15

PEDREGOSA, F.; VAROQUAUX, G.; GRAMFORT, A.; MICHEL, V.; THIRION, B.; GRISEL, O.; BLONDEL, M.; PRETTENHOFER, P.; WEISS, R.; DUBOURG, V.; VANDERPLAS, J.; PASSOS, A.; COURNAPEAU, D.; BRUCHER, M.; PERROT, M.; DUCHESNAY, E. Scikit-learn: machine learning in Python. **Journal of Machine Learning Research**, v. 12, p. 2825–2830, 2011. Available from: <<https://doi.org/10.48550/arXiv.1201.0490>>. 36

PENHA, T. V. **Detecção de áreas queimadas na Amazônia utilizando imagens de média resolução espacial, técnicas de GEOBIA e mineração de dados**. 74 p. Thesis (Master in Remote Sensing) — Instituto Nacional de Pesquisas Espaciais (INPE), São Jose dos Campos, 2018. 2, 9, 14

PEREIRA, A. A.; TEIXEIRA, F. R.; LIBONATI, R.; MELCHIORI, E. A.; CARVALHO, L. M. T. Avaliação de índices espectrais para identificação de áreas queimadas no Cerrado utilizando dados Landsat TM. **Revista Brasileira de Cartografia**, v. 8, n. 68, p. 1665–1680, 2016. Available from: <<https://doi.org/10.14393/rbcv68n8-44386>>. 2, 13

PEREIRA, J.; CHUVIECO, E.; BEAUDOIN, A.; DESBOIS, N. Remote sensing of burned areas: a review. In: CHUVIECO, E. (Ed.). **A review of remote sensing methods for the study of large wildland fires**. Alcalá de Henares: Universidad de Alcalá, 1997. p. 127–184. 13, 14

PESSÔA, A. C. M.; ANDERSON, L. O.; CARVALHO, N. S.; CAMPANHARO, W. A.; JUNIOR, C. H. S.; ROSAN, T. M.; REIS, J. B.; PEREIRA, F. R.; ASSIS, M.; JACON, A. D.; OMETTO, J. P.; SHIMABUKURO, Y. E.; SILVA, C. V. J.; PONTES-LOPES, A.; MORELLO, T. F.; ARAGÃO, L. E. O. C. Intercomparison of burned area products and its implication for carbon emission estimations in the Amazon. **Remote Sensing**, v. 12, n. 23, p. 3864, 2020. Available from: <<https://doi.org/10.3390/rs12233864>>. 22

PICOLI, M. C.; SIMOES, R.; CHAVES, M.; SANTOS, L. A.; SANCHEZ, A.; SOARES, A.; SANCHES, I. D.; FERREIRA, K. R.; QUEIROZ, G. R. CBERS data cube: a powerful technology for mapping and monitoring brazilian biomes. **ISPRS Annals of the Photogrammetry, Remote Sensing and Spatial Information Sciences**, v. 3, p. 533–539, 2020. Available from: <<https://doi.org/10.5194/isprs-annals-V-3-2020-533-2020>>. 11

PINHEIRO, E. d. S.; DURIGAN, G. Diferenças florísticas e estruturais entre fitofisionomias do cerrado em Assis, SP, Brasil. **Revista Árvore**, v. 36, p. 181–193, 2012. Available from: <<https://doi.org/10.1590/S0100-67622012000100019>>. 6

PINTY, B.; VERSTRAETE, M. GEMI: a non-linear index to monitor global vegetation from satellites. **Vegetation**, v. 101, p. 15–20, 1992. Available from: <<https://doi.org/10.1007/BF00031911>>. 14

PIVELLO, V. R. The use of fire in the cerrado and amazonian rainforests of Brazil: past and present. **Fire Ecology**, v. 7, p. 24–39, 2011. Available from: <<DOI:10.4996/fireecology.0701024>>. 6

PIVELLO, V. R.; VIEIRA, I.; CHRISTIANINI, A. V.; RIBEIRO, D. B.; MENEZES, L. da S.; BERLINCK, C. N.; MELO, F. P.; MARENGO, J. A.; TORNQUIST, C. G.; TOMAS, W. M.; OVERBECK, G. E. Understanding Brazil's catastrophic fires: causes, consequences and policy needed to prevent future tragedies. **Perspectives in Ecology and Conservation**, v. 19, n. 3, p. 233–255, 2021. Available from: <<https://www.perspectecolconserv.com/

en-understanding-brazils-catastrophic-fires-causes-articulo-S2530064421000560>>. 1, 3, 7, 13

RADOUX, J.; BOGAERT, P. Good practices for object-based accuracy assessment. **Remote Sensing**, v. 9, n. 7, p. 646, 2017. Available from: <<https://doi.org/10.3390/rs9070646>>. 12, 22

RAMO, R.; CHUVIECO, E. Developing a random forest algorithm for modis global burned area classification. **Remote Sensing**, v. 9, n. 11, p. 1193, 2017. Available from: <<https://doi.org/10.3390/rs9111193>>. 19

RAMO, R.; GARCÍA, M.; RODRÍGUEZ, D.; CHUVIECO, E. A data mining approach for global burned area mapping. **International Journal of Applied Earth Observation and Geoinformation**, v. 73, p. 39–51, 2018. Available from: <<https://doi.org/10.1016/j.jag.2018.05.027>>. 3, 16

RAMOS-NETO, M. B.; PIVELLO, V. R. Lightning fires in a Brazilian savanna national park: rethinking management strategies. **Environmental Management**, v. 26, p. 675–684, 2000. Available from: <<https://doi.org/10.1007/s002670010124>>. 7

RHODES, B. C. Pyephem: astronomical ephemeris for python. **Astrophysics Source Code Library**, 2011. Available from: <<https://ui.adsabs.harvard.edu/abs/2011ascl.soft12014R>>. 29

RIBEIRO, J. F.; WALTER, B. M. T. Fitofisionomias do bioma Cerrado. In: SANO, S. M.; ALMEIDA, S. P. D. (Ed.). **Cerrado: ambiente e flora**. Planaltina: EMBRAPA Cerrados, 1998. p. 152–212. 5, 6

_____. As principais fitofisionomias do bioma Cerrado. **Cerrado: Ecologia e Flora**, Embrapa Informação Tecnológica Brasília, v. 1, p. 151–212, 2008. 6

RIBEIRO, L. S. **História do Parque Nacional da Chapada dos Veadeiros: da sua criação à sua [re]ampliação em 2017**. 167 p. Thesis (Master in Sustainable Development) — Universidade de Brasília (UnB), Brasilia, 2020. 24

RODRIGUES, J. A.; LIBONATI, R.; PEREIRA, A. A.; NOGUEIRA, J. M.; SANTOS, F. L.; PERES, L. F.; ROSA, A. S.; SCHROEDER, W.; PEREIRA, J. M. C.; GIGLIO, L.; TRIGO, I. F.; SETZER, A. W. How well do global burned area products represent fire patterns in the Brazilian savannas biome? an accuracy assessment of the mcd64 collections. **International Journal of Applied Earth Observation and Geoinformation**, v. 78, p. 318–331, 2019. Available from: <<https://doi.org/10.1016/j.jag.2019.02.010>>. 22

ROUSE, J. W.; HAAS, R. H.; SCHELL, J. A.; DEERING, D. W. **Monitoring vegetation systems in the great plains with ERTS**. Washington: NASA, 1974. 309 p. 14

ROY, D. P.; HUANG, H.; BOSCHETTI, L.; GIGLIO, L.; YAN, L.; ZHANG, H. H.; LI, Z. Landsat-8 and Sentinel-2 burned area mapping – a combined sensor

multi-temporal change detection approach. **Remote Sensing of Environment**, v. 231, p. 111254, 2019. Available from: <<https://doi.org/10.1016/j.rse.2019.111254>>. 3, 21

RUSSO, G. M. **Desenvolvimento de uma biblioteca Python para busca e processamento de dados do Satélite Sino-Brasileiro CBERS-04A**. 51 p. Thesis (Course in Computer Science) — Fundação Universidade Federal de Rondônia, Porto Velho, 2023. 26

SAWYER, D.; MESQUITA, B.; COUTINHO, B.; ALMEIDA, F. d.; FIGUEIREDO, I.; LAMAS, I.; PEREIRA, L.; PINTO, L.; PIRES, M.; KASECKER, T. **Ecosystem Profile: Cerrado Biodiversity Hotspot**. [S.l.]: Critical Ecosystem Parternship Fund, 2016. 1, 5

SCHEFFLER, D. **AROSICS: An Automated and Robust Open-Source Image Co-Registration Software for multi-sensor satellite data**. jul. 2017. Available from: <<https://doi.org/10.5281/zenodo.3743085>>. 30

SCHMIDT, I. B.; FONSECA, C. B.; FERREIRA, M. C.; SATO, M. N. Implementação do programa piloto de manejo integrado do fogo em três unidades de conservação do cerrado. **Biodiversidade Brasileira**, v. 6, n. 2, p. 55–70, 2016. 8

SCHMIDT-ROHR, K. Why combustions are always exothermic, yielding about 418 kj per mole of o2. **Journal of Chemical Education**, v. 92, n. 12, p. 2094–2099, 2015. Available from: <<https://doi.org/10.1021/acs.jchemed.5b00333>>. 9

SEREY, J.; ALFARO, M.; FUERTES, G.; VARGAS, M.; DURÁN, C.; TERNERO, R.; RIVERA, R.; SABATTIN, J. Pattern recognition and deep learning technologies, enablers of industry 4.0, and their role in engineering research. **Symmetry**, v. 15, n. 2, p. 535, 2023. Available from: <<https://doi.org/10.3390/sym15020535>>. 17

SHIMABUKURO, Y. E.; DUARTE, V.; ARAI, E.; FREITAS, R.; LIMA, A.; VALERIANO, D.; BROWN, I.; MALDONADO, M. Fraction images derived from Terra MODIS data for mapping burnt areas in Brazilian Amazonia. **International Journal of Remote Sensing**, v. 30, n. 6, p. 1537–1546, 2009. Available from: <<https://doi.org/10.1080/01431160802509058>>. 3

SHIMABUKURO, Y. E.; DUTRA, A. C.; ARAI, E.; DUARTE, V.; CASSOL, H. L. G.; PEREIRA, G.; CARDOZO, F. d. S. Mapping burned areas of Mato Grosso State Brazilian Amazon using multisensor datasets. **Remote Sensing**, v. 12, n. 22, p. 3827, 2020. Available from: <<https://doi.org/10.3390/rs12223827>>. 3, 16, 22

SILVA, W. K. L.; GRANDE, E. T. G.; OLIVEIRA, D. C. de. Estudo do satélite brasileiro Amazonia-1 e de sua trajetória: mapeamento sistemático e análise documental dos artefatos históricos–oficiais. **Research, Society and Development**, v. 11, n. 2, p. 1–35, 2022. Available from: <<https://doi.org/10.33448/rsd-v11i2.25894>>. 11

SIMON, M. F.; GRETHER, R.; QUEIROZ, L. P. de; SKEMA, C.; PENNINGTON, R. T.; HUGHES, C. E. Recent assembly of the Cerrado, a neotropical plant diversity hotspot, by in situ evolution of adaptations to fire. **Proceedings of the National Academy of Sciences**, v. 106, n. 48, p. 20359–20364, 2009. Available from: <<https://doi.org/10.1073/pnas.0903410106>>. 3

SOTERRONI, A. C.; RAMOS, F. M.; MOSNIER, A.; FARGIONE, J.; ANDRADE, P. R.; BAUMGARTEN, L.; PIRKER, J.; OBERSTEINER, M.; KRAXNER, F.; CÂMARA, G.; CARVALHO, A. X. Y.; POLASKY, S. Expanding the soy moratorium to Brazil's Cerrado. **Science Advances**, v. 5, n. 7, p. 1–9, 2019. Available from: <<https://www.science.org/doi/10.1126/sciadv.aav7336>>. 1

STROPPIANA, D.; BORDOGNA, G.; SALI, M.; BOSCHETTI, M.; SONA, G.; BRIVIO, P. A. A fully automatic, interpretable and adaptive machine learning approach to map burned area from remote sensing. **ISPRS International Journal of Geo-Information**, v. 10, n. 8, p. 546, 2021. Available from: <<https://doi.org/10.3390/ijgi10080546>>. 17

SZPAKOWSKI, D. M.; JENSEN, J. L. A review of the applications of remote sensing in fire ecology. **Remote Sensing**, v. 11, n. 22, p. 2638, 2019. Available from: <<https://doi.org/10.3390/rs11222638>>. 9

TANSEY, K.; GRÉGOIRE, J.-M.; DEFOURNY, P.; LEIGH, R.; PEKEL, J.-F.; BOGAERT, E. V.; BARTHOLOMÉ, E. A new, global, multi-annual (2000–2007) burnt area product at 1 km resolution. **Geophysical Research Letters**, v. 35, n. 1, 2008. Available from: <<https://doi.org/10.1029/2007GL031567>>. 21

TIWARI, T.; TIWARI, T.; TIWARI, S. How artificial intelligence, machine learning and deep learning are radically different? **International Journal of Advanced Research in Computer Science and Software Engineering**, v. 8, n. 2, p. 1, 2018. 17

TYRALIS, H.; PAPACHARALAMPOUS, G.; LANGOUSIS, A. A brief review of random forests for water scientists and practitioners and their recent history in water resources. **Water**, v. 11, n. 5, p. 910, 2019. Available from: <<https://doi.org/10.3390/w11050910>>. 18

UNIVERSIDADE FEDERAL DO RIO DE JANEIRO (UFRJ). **Alerta de área queimada com monitoramento estimado por satélite**. 2023. Available from: <<https://alarmes.lasa.ufrj.br/>>. Access in: 01 jul. 2023. 2

VALERIANO, D. M. **FREL Cerrado: Nível de referência de emissões provenientes do desmatamento do Cerrado**. 2017. <http://redd.mma.gov.br/images/conaredd/conaredd_frelcerrado_daltonvaleriano.pdf>. Access in: 2 jul. 2023. xiii, 6

VIEIRA, L. d. S.; QUEIROZ, G.; SHIGUEMORI, E. An analysis of the influence of the number of observations in a random forest time series classification to map the forest and deforestation in the Brazilian Amazon. **The International Archives of the Photogrammetry, Remote Sensing and Spatial Information Sciences**, v. 43, p. 721–728, 2022. 18

WALTER, H. **Vegetação e zonas climáticas**. São Paulo: Editora Pedagógica e Universitária, 1986. 325 p. 6

WHITESIDE, T. G.; BOGGS, G. S.; MAIER, S. W. Comparing object-based and pixel-based classifications for mapping savannas. **International Journal of Applied Earth Observation and Geoinformation**, v. 13, n. 6, p. 884–893, 2011. Available from: <<https://doi.org/10.1016/j.jag.2011.06.008>>. 21

WOOD, D. A. Prediction and data mining of burned areas of forest fires: Optimized data matching and mining algorithm provides valuable insight. **Artificial Intelligence in Agriculture**, v. 5, p. 24–42, 2021. Available from: <<https://doi.org/10.1016/j.aiia.2021.01.004>>. 16, 17

WOODCOCK, C. E.; LOVELAND, T. R.; HEROLD, M.; BAUER, M. E. Transitioning from change detection to monitoring with remote sensing: a paradigm shift. **Remote Sensing of Environment**, v. 238, p. 1–5, 2020. Available from: <<https://doi.org/10.1016/j.rse.2019.111558>>. 16

XI, E. Image classification and recognition based on deep learning and random forest algorithm. **Wireless Communications and Mobile Computing**, v. 2022, 2022. Available from: <<https://doi.org/10.1155/2022/2013181>>. 18, 19

XU, L.; HEROLD, M.; TSENDBAZAR, N.-E.; MASILIŪNAS, D.; LI, L.; LESIV, M.; FRITZ, S.; VERBESSELT, J. Time series analysis for global land cover change monitoring: a comparison across sensors. **Remote Sensing of Environment**, v. 271, p. 112905, 2022. Available from: <<https://doi.org/10.1016/j.rse.2022.112905>>. 16

ZAJKO, M. Artificial intelligence, algorithms, and social inequality: sociological contributions to contemporary debates. **Sociology Compass**, v. 16, n. 3, p. 1–16, 2022. Available from: <<https://doi.org/10.1111/soc4.12962>>. 17

ZHU, Z. Change detection using landsat time series: a review of frequencies, preprocessing, algorithms, and applications. **ISPRS Journal of Photogrammetry and Remote Sensing**, v. 130, p. 370–384, 2017. Available from: <<https://doi.org/10.1016/j.isprsjprs.2017.06.013>>. 16